学位論文

Theory of nonequilibrium steady states in multiband systems in ac-fields and its applications

(ac外場中の多バンド系における非
平衡定常状態の理論とその応用)

平成２５年１２月博士（理学）申請

東京大学大学院理学系研究科
物理学専攻
見上　敬洋

Thesis

Theory of nonequilibrium steady states in multiband systems in ac-fields and its applications

Takahiro Mikami

Department of Physics, University of Tokyo

December 2013

Abstract

In this thesis, multiband correlated electron systems driven into nonequilibrium by strong ac-electric fields are studied numerically and analytically. Our fundamental interest is to understand how multiband electron systems, which exhibit various properties originating from orbital degrees of freedom already in equilibrium, should exhibit even richer physics when driven out of equilibrium under the influence of external fields.

We have performed this in two steps. First, we have formulated the *multiband Floquet-DMFT* (dynamical mean field theory) as a basis for simulating multiband correlated systems. This is done by extending the previously developed Floquet-DMFT for single-band electron systems to multiband electron systems in ac-electric fields. We also clarify the connection between our formalism and the photo-induced Berry curvature, which is extensively studied in the context of Floquet topological insulators. This is the first study to establish a multiband extension of Floquet-DMFT formalism.

Using the multiband Floquet-DMFT, we then study two interesting multiband systems, the *dp*-model and the honeycomb-Hubbard model (the Hubbard model on honeycomb lattice) in ac-electric fields. In particular, we choose *circularly polarized lights* that are known to drive novel physics such as photo-induced topological phase transitions.

Our interest in nonequilibrium steady states of the *dp*-model in strong ac-fields is motivated from recent pump-probe measurements in high-T_c cuprates. We investigate electronic structures in the *dp*-model in strong circularly polarized ac-fields and obtain novel photon-dressed band structures and nonequilibrium distribution functions which indicate a *population inversion*. Specifically, we have calculated optical conductivities and found characteristic features (*negative optical conductivities*) in the nonequilibrium situation. We have also discussed how the Zhang-Rice singlet band behaves under the influence of external fields.

We then study nonequilibrium steady states of the honeycomb-Hubbard model in circularly polarized electric fields, as a paradigm for the interplay between photo-induced topological properties and electron correlation. We have revealed, by numerical calculation of electronic structures and optical conductivities, that the system exhibits a novel phase diagram where we have both photo-induced Mott transitions and topological-to-topological phase transitions. To give a physical insight into the numerical result, we develop an analytic perturbation theory for Floquet states, which provides a picture that the correlated electron system on honeycomb lattice in an intense circularly polarized field has an effective Hamiltonian for an anomalous quantum Hall system (Haldane model) where the topological number changes sign many times as the field strength is increased.

Acknowledgement

I would like to express my deepest gratitude to Prof. Hideo Aoki who provided helpful comments and suggestions on my thesis. I am also indebted to Dr. Naoto Tsuji and Dr. Takashi Oka for fruitful discussions. Also, I would like to thank all the members in our Laboratory, Yuta Murakami, Motoharu Kitatani and Sota Kitamura, whose comments made enormous contribution to my work. I heartily thank Prof. Takeo Kato, Prof. Naomichi Hatano, Prof. Seiji Miyashita, Prof. Ryo Shimano and Prof. Hidenori Takagi for illuminating discussion, constructive comments and careful reading of this thesis. I would also like to express my gratitude to my family for their moral support and warm encouragements.

Finally, I gratefully appreciate the support of the Aoki Labolatory, that made it possible to have great opportunity to study at ETH, Zürich in Switzerland and discuss my research with Prof. Philipp Werner. These experiences highly influenced me and made it possible to complete my thesis with enthusiasms for researches on physics.

Contents

Chapter 1

Introduction

1.1 Physics of multi-orbital many-body electron systems

Electrons in solids exhibit amazingly huge variety of physics. In fact, materials surrounding us show various properties such as electric conductivity, optical or magnetic properties, and so on. The complexity and diversity of phenomena in electronic systems may be surprising since, in a microscopic point of view, electrons in a solid are simply described in terms of the Hamiltonian,

$$\mathscr{H} = \mathscr{H}_0 + \mathscr{H}_1, \tag{1.1a}$$

$$\mathscr{H}_0 = \sum_\sigma \int d\boldsymbol{r}^3 \psi_\sigma^\dagger \left[-\frac{\hbar^2}{2m}\nabla^2 + V(\boldsymbol{r}) \right] \psi_\sigma(\boldsymbol{r}), \tag{1.1b}$$

$$\mathscr{H}_1 = \frac{1}{2}\sum_{\sigma\sigma'} \iint d\boldsymbol{r} d\boldsymbol{r}' \psi_\sigma^\dagger(\boldsymbol{r}) \psi_{\sigma'}^\dagger(\boldsymbol{r}') \frac{e^2}{|\boldsymbol{r}-\boldsymbol{r}'|} \psi_{\sigma'}(\boldsymbol{r}') \psi_\sigma(\boldsymbol{r}), \tag{1.1c}$$

with electron field operator $\psi_\sigma(\boldsymbol{r})$ for spin σ, Planck's constant $\hbar = 1.05 \times 10^{-34}\mathrm{J}\cdot\mathrm{s}$, the mass of an electron $m = 9.11 \times 10^{-31}\mathrm{kg}$, and the elementary charge $e = 1.60 \times 10^{-19}\mathrm{C}$. $\mathscr{H}_0$ and $\mathscr{H}_1$ are the kinetic energy and the potential energy from Coulomb repulsion among electrons, respectively. The scalar potential $V(\boldsymbol{r})$ represents the Coulomb attraction between an electron and nuclei that are periodically arranged, forming a lattice structure of the material. In the Hamiltonian Eq. (1.1), material dependence only appears in the periodic potential $V(\boldsymbol{r})$.

It is important to treat the noninteracting Hamiltonian $\mathscr{H}_0$, which contains the material dependence, properly so that one can capture the electronic states subject to the periodically arranged nuclei. The standard way to do that begins with reinterpreting the Hamiltonian in terms of noninteracting atomic orbitals, which is the so-called *tight-binding approximation*. In this approximation, one first picks up a nucleus in the solid. The isolated atom forms atomic orbitals as depicted in Fig. 1-1. Atoms in a unit cell are arranged periodically and thus one can make electronic states with a wave vector $\boldsymbol{k}$ as

$$\phi_{\boldsymbol{k}\alpha\sigma}(\boldsymbol{r}) = \frac{1}{\sqrt{N_c}} \sum_j e^{i\boldsymbol{k}\cdot\boldsymbol{R}_j} \phi_{\alpha\sigma}(\boldsymbol{r}-\boldsymbol{R}_j), \tag{1.2}$$

using atomic orbitals $\phi_{\alpha\sigma}(\boldsymbol{r}-\boldsymbol{R}_j)$ with an orbital index α and the position $\boldsymbol{R}_j$ of a unit cell

(N_c is the number of unit cells). Using the atomic orbitals as a basis, we expand the electron field operator as

$$\psi_\sigma(\boldsymbol{r}) = \sum_{\boldsymbol{k}\alpha} \phi_{\boldsymbol{k}\alpha\sigma}(\boldsymbol{r})^* c_{\boldsymbol{k}\alpha\sigma} = \sum_{j\alpha} \phi_{\alpha\sigma}(\boldsymbol{r}-\boldsymbol{R}_j)^* c_{j\alpha\sigma} \tag{1.3}$$

with $c_{\boldsymbol{k}\alpha\sigma}$ and $c_{j\alpha\sigma}$ the fermionic annihilation operators for the electronic states labeled by $(\boldsymbol{k},\alpha,\sigma)$ and (j,α,σ), respectively. This representation leads to the tight-binding Hamiltonian,

$$\mathscr{H} = \sum_{jl,\alpha\beta,\sigma} t_{jl}^{\alpha\beta} c_{j\alpha\sigma}^\dagger c_{l\beta\sigma} + \frac{1}{2} \sum_{i\alpha j\beta\sigma} \sum_{i'\alpha' j'\beta'\sigma'} U(i\alpha\sigma, j\beta\sigma' | i'\alpha'\sigma, j'\beta'\sigma') c_{i'\alpha'\sigma}^\dagger c_{j'\beta'\sigma'}^\dagger c_{j\beta\sigma'} c_{i\alpha\sigma} \tag{1.4}$$

with the hopping amplitude $t_{jl}^{\alpha\beta}$ of an electron between two orbitals (j,α,σ) and (l,β,σ), and the Coulomb matrix element $U(i\alpha\sigma, j\beta\sigma' | i'\alpha'\sigma, j'\beta'\sigma')$ for a two-body process of scattering of a pair of electrons (i,α,σ) and (j,β,σ') into another pair (i',α',σ) and (j',β',σ'). This two-body amplitude between different positions and orbitals are small compared to that for the same orbital and the site, and thus one can neglect the inter-orbital or inter-site Coulomb scattering amplitudes in a first approximation. This assumption leads to a more simplified Hamiltonian,

$$\mathscr{H} = \sum_{jl,\alpha\beta,\sigma} t_{jl}^{\alpha\beta} c_{j\alpha\sigma}^\dagger c_{l\beta\sigma} + \sum_{i\alpha} U_\alpha c_{i\alpha\uparrow}^\dagger c_{i\alpha\downarrow}^\dagger c_{i\alpha\downarrow} c_{i\alpha\uparrow}, \tag{1.5a}$$

$$t_{jl}^{\alpha\beta} = \int d\boldsymbol{r} \phi_{\alpha\sigma}(\boldsymbol{r}-\boldsymbol{R}_j)^* \left[-\frac{\hbar^2}{2m}\nabla^2 + V(\boldsymbol{r}) \right] \phi_{\beta\sigma}(\boldsymbol{r}-\boldsymbol{R}_l), \tag{1.5b}$$

$$U_\alpha = \iint \phi_\alpha(\boldsymbol{r})^* \phi_\alpha(\boldsymbol{r}')^* \frac{e^2}{|\boldsymbol{r}-\boldsymbol{r}'|} \phi_\alpha(\boldsymbol{r}') \phi_\alpha(\boldsymbol{r}). \tag{1.5c}$$

with the *intra-orbital Coulomb repulsion* U_α for the orbital α.

We should note that, in some cases, the inter-orbital Coulomb scattering amplitudes that we have dropped, may play crucial roles in multi-band electron systems. In fact, if there are nearly degenerate orbitals on each site, the inter-orbital Coulomb matrix elements $U'_{\alpha\beta}$ and $J_{\alpha\beta}$ ($\alpha \neq \beta$) given by

$$U'_{\alpha\beta} = \iint \phi_\alpha(\boldsymbol{r})^* \phi_\beta(\boldsymbol{r}')^* \frac{e^2}{|\boldsymbol{r}-\boldsymbol{r}'|} \phi_\beta(\boldsymbol{r}') \phi_\alpha(\boldsymbol{r}), \tag{1.6a}$$

$$J_{\alpha\beta} = \iint \phi_\alpha(\boldsymbol{r})^* \phi_\beta(\boldsymbol{r}')^* \frac{e^2}{|\boldsymbol{r}-\boldsymbol{r}'|} \phi_\alpha(\boldsymbol{r}') \phi_\beta(\boldsymbol{r}), \tag{1.6b}$$

may become comparable to the intra-orbital Coulomb repulsion U_α. $U'_{\alpha\beta}$ and $J_{\alpha\beta}$ are respectively called *inter-site Coulomb repulsion* and *Hund's coupling* between α- and β-orbitals. In fact, the ferromagnetism of itinerant d-electron systems have moderate values of Hund's coupling, and the origin of the itinerant ferromagnetism is considered to be Hund's coupling [1, 2, 3, 4]. In this study, however, we are not going to study the physics of inter-band Coulomb interactions. As we will discuss later, intra-orbital Coulomb repulsions itself give rise to rich physics and we are going to study that aspects of Coulomb interaction for the first approximation.

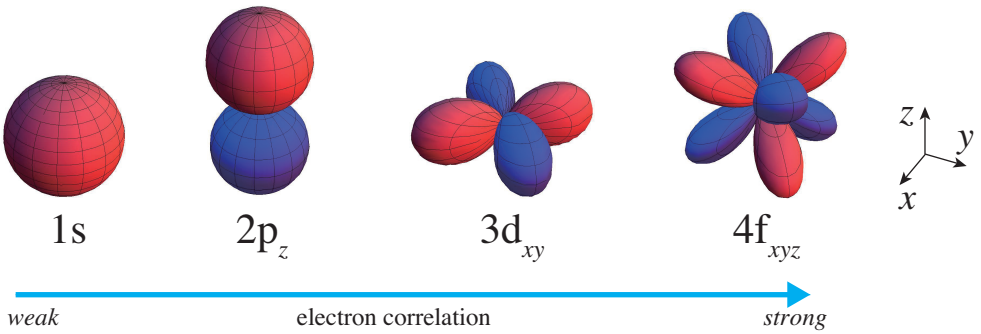

Figure 1-1: Real number representation of atomic orbitals in the three-dimensional space. Sign of the wave function is depicted as red and blue regions.

The fermionic lattice model Eq. (1.5), namely the multi-orbital Hubbard model, is the minimal model to study the interacting electrons in a multi-orbital system. There, the individuality of the solid enters in the hopping matrix $t_{jl}^{\alpha\beta}$ and the strength U_α of electron-electron repulsion for each orbital. The hopping process drives electrons delocalized so that the kinetic energy may be minimized, while the interaction prevents electrons from moving freely and renders the system insulating. Thus there exists a competition between metallic and insulating nature in the model. In general, the strength of electron-electron repulsion becomes larger with the angular momentum of the orbital as in Fig. 1-1, and therefore the electron repulsion plays an important role when the material contains heavy atoms with d or f orbitals.

The Hamiltonian Eq. (1.5), although a minimal model for interacting fermionic systems, contains rich physics due to the multi-orbital degrees of freedom and the presence of many-body interactions.

One important physics is the metal-insulator phase transition driven by the electron correlation [5]. Consider an electronic system described by the single-band Hubbard model,

$$\mathscr{H} = \sum_{ij} t_{ij} c_{i\sigma}^\dagger c_{j\sigma} + \sum_i U n_{i\uparrow} n_{i\downarrow}. \tag{1.7}$$

If one puts an electron on a site where another electron is already occupied, the electron feels the Coulomb repulsion energy U. Therefore, when every site is occupied by one electron, there exists a finite excitation energy U for an electron added to an occupied site. If the repulsion U is so large that the kinetic energy cannot compensate the penalty, electrons prefer to stay at their sites and the system shows insulating feature. Such correlation-induced insulators are called *Mott insulators*, which was first theoretically investigated by Mott [6]. Mott insulators show significant differences from conventional band insulators when additional carriers are doped in the system. In fact, doping carriers into Mott insulators gives rise to amazingly rich physics, such as antiferromagnetism and superconductivity [7].

Especially in copper-oxide based materials, there exists an unconventional superconducting phase close to the antiferromagnetic insulating phase. As we shall go into detail in Chapter 4, cuprates are composed of CuO_2 layers and its minimal lattice model are the so-called

dp-model [8], a three-band Hubbard model which contains d- and p-orbitals on copper and oxygen atoms, respectively. In undoped cuprates, $d_{x^2-y^2}$-orbitals on copper sites are half-filled, while p-orbitals on oxygen sites are fully occupied. Due to the strong electron-electron repulsion U on copper sites, undoped cuprates are Mott insulators. At sufficiently low temperatures, electron spins on copper sites exhibit antiferromagnetic order, due to the super-exchange interaction.

There are long debates on the theoretical treatments for the dp-model. Immediately after the proposal of the dp-model by Emery [8], Zhang and Rice [9] showed that the dp-model can be mapped to the so-called t-J model [10], equivalent to the large-U limit of the single-band Hubbard model Eq. (1.7). The important observation by Zhang and Rice is that a doped hole situated on an oxygen atom forms a spin-singlet with another hole on the neighboring copper site (Zhang-Rice singlet, ZRS). ZRS is energetically very stable and thus doped holes on a CuO_2 plane is effectively expressed as ZRSs moving in the antiferromagnetic background, as the t-J model describes.

However, it is also pointed out that the single-band Hubbard model lacks some important physics. For example, in magnetic fields, the ZRS is no longer robust, and thus the single-band Hubbard model and the dp-model do not give consistent results even in the large-U limit [11]. The multi-band nature of cuprates become even more important when we discuss the difference between electron and hole doping [12]. It is experimentally known [13, 14, 15] that doped holes are situated in oxygen atoms and form ZRS [9], while doped electrons go to copper sites and form doublons. This is because the difference of energy level between d- and p-orbitals are small compared to the Coulomb interaction U and cuprates are categorized as the so-called *charge-transifer insulators*, as pointed out by Zaanen, Sawatzly and Allen [16]. Therefore cuprates should be basically treated by the dp-model in order to treat the hole- and electron-doping on a equal footing. In fact, the multi-band nature of cuprates are recently investigated in the context of d-wave superconductivity [17], and are expected to be even more important for photo-carrier doping which induces electrons and holes at the same time, as we will discuss later.

Another important physics of multi-band systems appears even in the absence of the electron correlation. Suppose that the electrons are weakly correlated and set $U_\alpha = 0$ for every orbital involved. In that case the system is described by the noninteracting Hamiltonian in Eq. (1.5) and its eigenstates are obtained as $|u_{\boldsymbol{k}\alpha}\rangle$ which are labeled by the Bloch wave number $\boldsymbol{k}$ and the band index α. Regarding the eigenstates as a mapping from the momentum $\boldsymbol{k}$ in the Brillouin zone onto $|u_{\boldsymbol{k}\alpha}\rangle$ in the Hilbert space, one can construct a gauge-invariant quantity, $\mathscr{B}_{\boldsymbol{k}\alpha} = -i\nabla_{\boldsymbol{k}} \times \langle u_{\boldsymbol{k}\alpha}|\nabla_{\boldsymbol{k}}|u_{\boldsymbol{k}\alpha}\rangle$, for each band α. This represents a curvature in the $\boldsymbol{k}$-space, and its $\boldsymbol{k}$-integral over the whole Brillouin zone gives an integer that signifies a topological number of the band α, which was clearly pointed out by Thouless, *et al.* [18]. Namely, band structures with nontrivial topological numbers are first investigated in integer quantum Hall states in strong magnetic fields by Thouless *et al.* After that, Haldane constructed an artificial toy model that exhibits topological phases even in the absence of the magnetic fields [19]. Recently, Fu, Kane and Mele pointed out that Haldane's model can be realized in spin-orbit coupled systems [20, 21, 22] and found a new class of materials called *topological insulators* [23]. All the topologically nontrivial systems have orbital degrees of

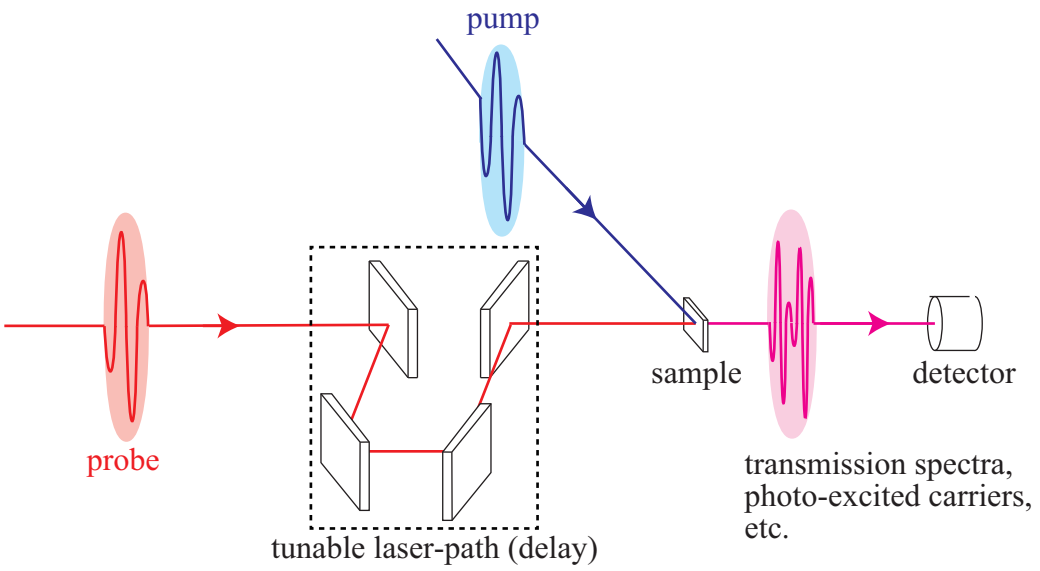

Figure 1-2: Schematic description of pump-probe experiments.

freedom (Landau levels in integer quantum Hall states, and band indices in topological insulators) and thus it is necessary to consider multi-orbital models to study topological aspects of solids. We will present the detailed explanation of the topological phases in noninteracting systems in Chapter 5.

1.2 Electrons in multi-band systems driven out of equilibrium

1.2.1 Experiments

In the previous section we have introduced the physics of multi-band electron systems where orbital degrees of freedom play crucial roles. There, the system shows rich phase diagrams containing metal-insulator phase transitions or topological phase transitions by varying some parameters such as the density of electrons, disorders, electron hopping and interaction. Recently experimental techniques have been developed for generating lasers with various photon energies and measuring systems in an ultrafast time-scale. Such developments have enabled us to realize optical manipulations of electronic states of systems and to study the possibility of phase transitions by means of external fields.

One of the most powerful experimental techniques is the pump-probe measurements. In Fig. 1-2, we depict a schematic picture of the pump-probe measurements. In these experiments, a pump-light with mid-infrared to visible light (corresponding to the photon energy 10 meV ~ 10 eV, with typical pulse width ~100 fs) is applied to the sample. After the pump light, a subsequent probe light is applied to the sample to observe the reflectance spectrum that contains information of the pumped states. The time interval between the pump-light and pulse-light are arbitrarily chosen, so that the transient spectra of the system are traced as a function of time after the pumping.

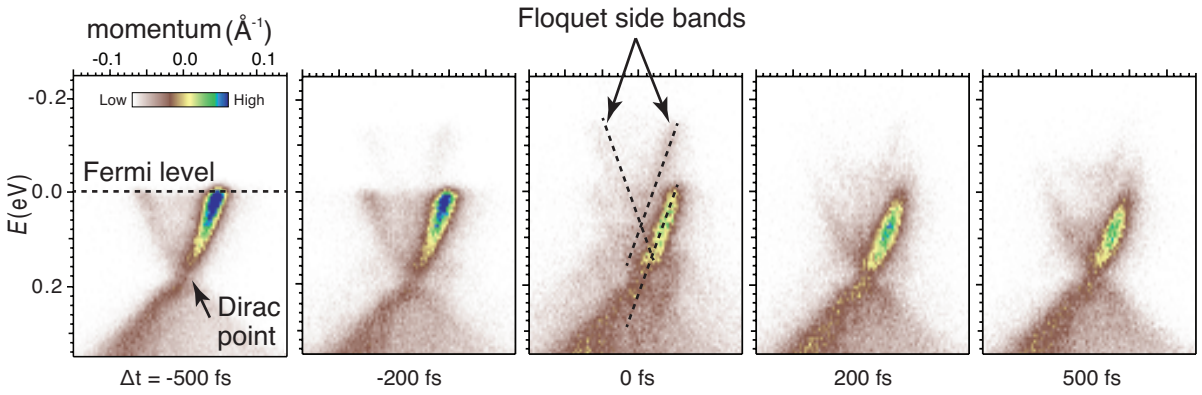

Figure 1-3: Time-resolved ARPES for surface Dirac electrons in a topological insulator Bi_2Se_3 [28], reprinted with kind permission from AAAS. A probe light with photon energy 180 meV and pulse width 250 fs is applied to the sample, together with some probe lights after the time delay Δt. $\Delta t < 0$ [$\Delta t > 0$] indicates the probe light is ahead of [behind] the pump light.

There are a number of interesting reports with the pump-probe measurements in real materials. Okamoto, *et al*. [24] studied photo-excited states of undoped cuprates and observed photo-induced carriers in Mott-insulating state. Fausti, *et al*. [25] reported a photo-induced superconductivity in stripe-ordered cuprates (A detailed explanation is presented in Chapter 4).

Another important observable in pump-probe measurements is the momentum and energy of electrons themselves in the sample. By combining the angle-resolved photoemission spectroscopy (ARPES) with pump-probe measurement techniques, one can directly detect the photo-excited electrons in a time-resolved fashion [26, 27, 28]. In Fig. 1-3 we show an example in transient momentum-resolved spectra on the surface of a topological insulator Bi_2Se_3 by Wang, *et al*. [28]. Δt is the time of the arrival of the probe light at the sample, where the arrival of the pump light is set to be $\Delta t = 0$. Bi_2Se_3 is gapped ($\sim$ 300 meV) in the bulk, while there is a surface mode that has a massless Dirac dispersion, protected by the topological aspect of the material. Wang, *et al*. applied the pump light with pulse width 250 fs (full width at the half-maximum) and photon energy Ω =180 meV, smaller than the bulk gap, so that the pump field interacts only with surface electrons. In the center panel ($\Delta t = 0$) of Fig. 1-3, one can see some copies of the original Dirac dispersions, with the energy interval Ω. The appearance of side-bands under the influence of ac-fields are theoretically predicted, and such side-band states are called *Floquet states*, the steady states of ac-driven electronic systems, oscillating periodically in time. The features of the spectral functions in Fig. 1-3 indeed coincides with the analysis with the Floquet theory [29, 30], and thus Wang, *et al*. concluded that the Floquet states do exist in their surface Dirac electron system driven by ac-fields.

1.2.2 Theoretical approach: steady states in ac-fields

These interesting experimental attempts at optical manipulation of electronic states have motivated theorists to study the dynamics of electrons in solids under the influence of external fields [31, 32]. In particular, we would like to address a question of what is happening to electrons in a solid during the application of the pump light. As we have stated, the pulse width applied to the system is typically ∼100 fs. In that time-interval, the pulse with photon energy $\hbar\Omega$ is equivalent to an ac-electric fields with frequency Ω continuously applied to the system. The 100 fs time-interval is greater than typical time scale of electron-electron scattering ∼10 fs [33]. This indicates that electrons approach to some nonequilibrium steady states during the period of the pump-fields.

As we have stated above and shall discuss in Chapter 3, it is known that periodically driven quantum systems have Floquet states, time-dependent steady state solutions of the Schrödinger equation. Although the ac-driven systems no longer have time-independent eigenstates in general, instead, one can take these Floquet states as basis states for the time-dependent Schrödinger equation and can interpret any steady states in terms of the Floquet states, as we usually describe electronic states in spatially periodic systems (solids) in terms of Bloch states. Moreover, using Floquet states as basis states, one can greatly reduce the computational costs in the study of steady states in ac-fields.

There are several works on Floquet study for periodical driven systems. Oka and Aoki [29] studied an electronic system on honeycomb lattice in circularly polarized ac-fields. They showed that the circularly polarized light induces a topological gap in the honeycomb lattice and gives rise to a photo-induced Hall effect. Subsequently, Kigatawa, *et al.* [34] showed, using perturbation theory combined with the Floquet theorem, that the photo-induced Hall state is equivalent to a topological state realized in the Haldane model [19] known as a prototypical model for topological insulators. Tsuji, *et al.* [35] developed a Green's function method combined with Floquet theory which is applicable to interacting system under the influence of ac-electric fields.

These developments in both experiments and theories in nonequilibrium states in ac-electric fields have motivated us to study ac-driven correlated electron systems with orbital degrees of freedom. As we have explained with a case of cuprates, in real materials orbital degrees of freedom cannot be neglected in general, and they become even more important under the influence of external fields, where high energy excitations are induced. Furthermore, multi-orbital systems in ac-electric fields can obtain topological properties, as proposed for noninteracting case by Oka and Aoki [36], and it is interesting to investigate whether the topological properties are affected, or even enhanced in the presence of electron correlation.

Electron correlation *and* orbital degrees of freedom in ac-electric fields have not been studied so far and our study consists of twofold steps. Firstly, we establish such numerical methods that can simulate multi-orbital correlate electron systems in ac-fields on a equal footing. Then we apply our numerical methods to some multi-orbital systems where experimental and theoretical interesting physics are expected. The results obtained in this thesis are listed as follows.

- **Extension of Floquet-DMFT method to multi-band correlated electron systems** (Chapter 3) — In order to study periodically driven many-body systems, we

should take into account the electron correlation and external fields in a non-perturbative manner. Tsuji, *et al*. [35] have proposed a novel Green's function technique that incorporates the electron correlation with the dynamical mean-field theory (DMFT) and external fields by the Floquet Green's functions. We have here extended the Floquet-DMFT technique to multi-band systems for the first time. One of the essential differences between the single-band and multi-band systems is the appearance of a photo-induced Berry phase under the influence of external fields, as Oka, *et al.* [29] have shown in the noninteracting case. To extend their argument to many-body systems, we shall clarify the connection between the photo-induced Berry phase and the dc-Hall conductivity in terms of Floquet Green's functions in the chapter.

- **Application I: the *dp*-model in circularly polarized ac-fields** (Chapter 4) — In order to investigate the properties of photo-induced cuprates [24, 25], we study the *dp*-model, a three-band Hubbard model for CuO_2 plane in cuprates [8], under the influence of ac-electric fields. Based on Floquet-DMFT, we study the steady states in the *dp*-model in circularly polarized ac-fields. Investigating the nonequilibrium electronic states and their transport properties, we shall find that a *population inversion* [35] takes place for large photon energy, which is accompanied by a negative optical conductivity.

- **Application II: the Hubbard model on honeycomb lattice in circularly polarized ac-fields** (Chapter 5) — As a paradigm of the interplay of photo-induced topology and electron correlation, we study the Hubbard model on honeycomb lattice in circularly polarized ac-fields. The honeycomb lattice in circularly polarized fields is one of the minimal model that exhibits photo-induced topological phase transitions, and studied in noninteracting and weak-field regime [29]. In this study, we investigate strongly correlated regime and intense-field regime. We shall find a novel *photo-induced metal-to-insulator phase transition* and *topological-to-topological phase transitions* for the first time in the overlooked regime. Further, we develop an analytic construction technique for obtaining an effective Hamiltonian, in order to provide insights into our findings by constructing an effective Hamiltonian.

1.3 Organization of the thesis

With the above background, we shall present the fundamentals of nonequilibrium many-body physics, developments of new theoretical tools, and its application to the multi-band systems. The organization of this thesis is the following (Fig. 1-4).

In Chapter 2, we review the basics of Green's function theory for nonequilibrium many-body systems. Especially we shall take account of dissipation, by attaching an exactly solvable heat-bath to the system. We also introduce DMFT, which is a powerful framework to investigate strongly correlated systems even out of equilibrium.

In Chapter 3, we introduce the Floquet-DMFT method in multi-band electron systems. We also formulate the nonequilibrium Kubo formula for optical conductivity and discuss the connection between the photo-induced Berry curvature and the Hall conductivity in ac-driven

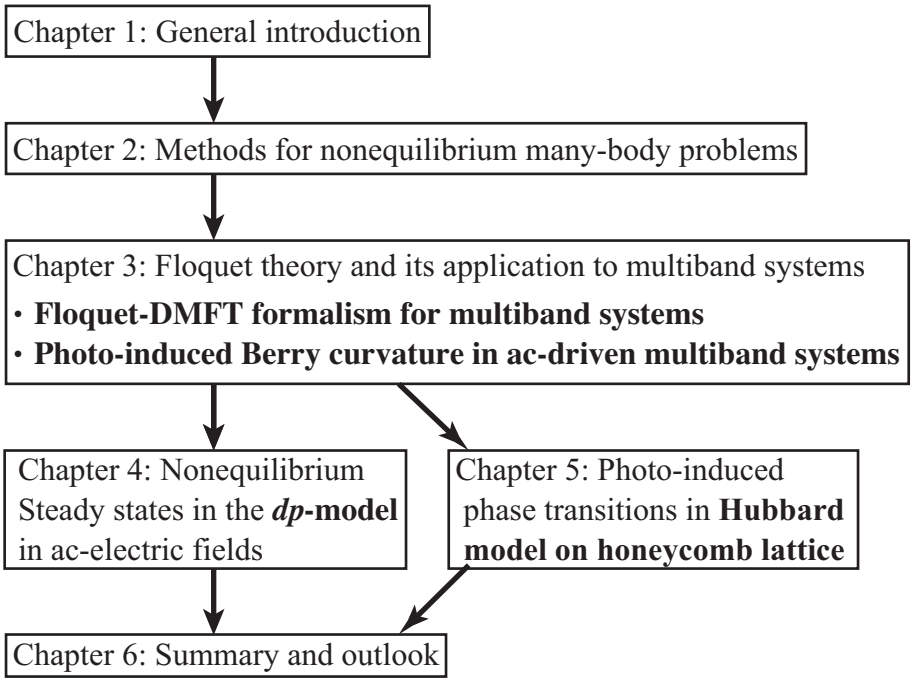

Figure 1-4: A flow diagram of the thesis.

systems.

Having fully formulated the Floquet-DMFT technique, we apply our method to the *dp*-model in Chapter 4, and the honeycomb-Hubbard model in Chapter 5. In both chapters, the motivation and the formalism specific for each system are stated in detail.

Chapter 2

Methods for non-equilibrium many-body problems

In this chapter, we review the nonequilibrium Green' function theory, and set a foundation of the theoretical method to study quantum many-body nonequilibrium steady states. For that purpose we focus on the Keldysh-Green's function formalism for the steady states of quantum systems attached to dissipative environments. We also introduce the dynamical mean-field theory (DMFT) so that the strong electron correlation can be incorporated.

2.1 Green's functions in Keldysh formalism

Methods of Green's functions have been developed as a powerful tool for treating interactions in a perturbative way. A point of these methods is that many-body interactions, which cannot be treated exactly in general, can be systematically treated as an expansion in terms of noninteracting Green's functions that is explicitly obtained from the knowledge of noninteracting Hamiltonian. The fact that any observables in interacting systems can be expanded in terms of noninteracting Green's functions is based on Wick's theorem [37]. Wick's theorem turns out to hold in ground states, at finite temperatures [38, 39], and even in nonequilibrium [40, 41]. The series expansion can be expressed as Feynman diagrams [42, 40], which enables us to treat the perturbation in a handy manner.

The methods of the Green's functions for nonequilibrium are introduced by Keldysh [43] and by Kadanoff and Baym [44]. One important difference from that for equilibrium lies in the treatment of interactions in the initial state. In equilibrium formalism, the interaction is assumed to be absent in the infinite past (Gell-Mann and Low theorem [45]), so that the statistical averages in interacting situations can be replaced by a noninteracting one in a mathematical manner. In nonequilibrium, however, the assumption of adiabatic switching explicitly breaks down and we need a Green's function formalism free from the assumption of adiabatic switching-on.

Now we start with formulating the Green's function method for general nonequilibrium situations, based on Refs. [46, 47, 48]. Throughout this section, we consider the time evolu-

tion of a quantum system with the general Hamiltonian,

$$\mathscr{H}(t) = \mathscr{H}_0(t) + \mathscr{H}_1(t), \tag{2.1}$$

where $\mathscr{H}_0(t)$ is an unperturbed one-body term and $\mathscr{H}_1(t)$ is a perturbation term. We assume that the initial state is given by a density matrix $\rho(t_0)$.

Once the Hamiltonian $\mathscr{H}(t)$ is given, the time evolution of the quantum system is given by the Schrödinger equation for the density matrix $\rho(t)$,

$$i\frac{\partial}{\partial t}\rho(t) = [\rho(t), \mathscr{H}(t)], \tag{2.2}$$

where $[A,B] = AB - BA$ is the commutator of two operators A and B. Therefore, the expectation value of any observable $\hat{O}$ at time t is, in principle, obtained by $\mathrm{tr}\,\rho(t)\hat{O}$ with the solution $\rho(t)$ of the deterministic equation Eq. (2.2). Of course the Schrödinger equation cannot be solved in general and we need a suitable technique according to each problem we face.

2.1.1 Interaction picture on L-shaped contour

In order to develop the perturbation theory with respect to $\mathscr{H}_1(t)$, we introduce the *interaction picture*. The time-evolution of the system is described by the unitary operator $\mathscr{U}(t,t_0)$ defined by $\mathscr{U}(t,t_0)|\Psi(t_0)\rangle = |\Psi(t)\rangle$. Combining it with the Schrödinger equation, we obtain the equation of motion,

$$i\frac{\partial}{\partial t}\mathscr{U}(t,t_0) = \mathscr{H}(t)\mathscr{U}(t,t_0). \tag{2.3}$$

The solution of Eq. (2.3) is formally given by

$$\mathscr{U}(t,t_0) = \begin{cases} \mathrm{T}\exp\left(-i\int_{t_0}^{t}\mathscr{H}(\bar{t})d\bar{t}\right) & t > t_0, \\ \tilde{\mathrm{T}}\exp\left(-i\int_{t_0}^{t}\mathscr{H}(\bar{t})d\bar{t}\right) & t < t_0, \end{cases} \tag{2.4}$$

where T [$\tilde{\mathrm{T}}$] is the time [anti-time] ordering operator.

Let us consider the time evolution of the expectation value of any observable $\hat{O}$. In *the Schrödinger picture*, the expectation value of $\hat{O}$ at time t is given by $\mathrm{tr}\,\rho(t)\hat{O}$ where the density matrix itself evolves as

$$\rho(t) = \mathscr{U}(t,t_0)\rho(t_0)\mathscr{U}(t_0,t).$$

In *the Heisenberg picture*, on the other hand, operator $\hat{O}$ evolves with time. The Heisenberg representation $\hat{O}_{\mathrm{H}}(t)$ is defined by

$$\hat{O}_{\mathrm{H}}(t) = \mathscr{U}(t_0,t)\hat{O}\mathscr{U}(t,t_0),$$

with the initial time t_0 as the reference point[1]. The expectation value is now written as $\mathrm{tr}\,\rho(t_0)\hat{O}_{\mathrm{H}}(t)$. In the Heisenberg picture, the state remains unchanged, while the observable $\hat{O}_{\mathrm{H}}(t)$ evolves with the full Hamiltonian $\mathscr{H}(t)$. In order to treat $\mathscr{H}_1(t)$ as a perturbation term,

[1] Heisenberg picture and interaction picture coincide with each other at $t = t_0$.

we move on to another picture, *the interaction picture*, where the time-evolution unitary operator $\mathscr{U}$ is replaced with $\mathscr{U}_0$, given by

$$\mathscr{U}_0(t,t_0) = \begin{cases} \mathrm{T}\exp\left(-i\int_{t_0}^{t}\mathscr{H}_0(\bar{t})d\bar{t}\right) & \text{for } t > t_0, \\ \tilde{\mathrm{T}}\exp\left(-i\int_{t_0}^{t}\mathscr{H}_0(\bar{t})d\bar{t}\right) & \text{for } t < t_0. \end{cases} \tag{2.5}$$

We consider the time evolution of $\hat{O}$ with the unperturbed unitary operator,

$$\hat{O}_{\mathrm{I}}(t) = \mathscr{U}_0(t_0,t)\hat{O}\mathscr{U}_0(t,t_0). \tag{2.6}$$

Then we obtain an equivalent expression for the expectation value,

$$\mathrm{tr}\,\rho(t_0)\mathscr{U}(t,t_0)\mathscr{U}_0(t,t_0)\hat{O}_{\mathrm{I}}(t)\mathscr{U}_0(t_0,t)\mathscr{U}(t,t_0) = \mathrm{tr}\,\rho(t_0)\mathscr{S}(t_0,t)\hat{O}_{\mathrm{I}}(t)\mathscr{S}(t,t_0).$$

We have defined a time evolution operator in the interaction picture, $\mathscr{S}(t,t_0)$, with the following properties:

$$\mathscr{S}(t,t_0) = \mathscr{U}_0(t_0,t)\mathscr{U}(t,t_0), \tag{2.7}$$

$$i\frac{\partial}{\partial t}\mathscr{S}(t,t_0) = \mathscr{H}_{1\mathrm{I}}(t)\mathscr{S}(t,t_0), \tag{2.8}$$

$$\mathscr{S}(t,t_0) = \begin{cases} \mathrm{T}\exp\left(-i\int_{t_0}^{t}\mathscr{H}_{1\mathrm{I}}(\bar{t})d\bar{t}\right) & \text{for } t > t_0, \\ \tilde{\mathrm{T}}\exp\left(-i\int_{t_0}^{t}\mathscr{H}_{1\mathrm{I}}(\bar{t})d\bar{t}\right) & \text{for } t < t_0, \end{cases} \tag{2.9}$$

where $\mathscr{H}_{1\mathrm{I}}(t)$ is the perturbative Hamiltonian $\mathscr{H}_1(t)$ in the interaction picture, defined in the same way as in Eq. (2.6). $\mathscr{S}(t,t_0)$ explicitly depends only on the perturbation Hamiltonian $\mathscr{H}_{1\mathrm{I}}$, and is therefore suitable for the perturbation expansion with respect to $\mathscr{H}_{1\mathrm{I}}$. The expectation value of an operator $\hat{O}$ is now expressed as

$$\langle\hat{O}_{\mathrm{H}}(t)\rangle_0 = \frac{\mathrm{tr}\,e^{-\beta\mathscr{H}(t_0)}\mathscr{S}(t_0,t)\hat{O}_{\mathrm{I}}(t)\mathscr{S}(t,t_0)}{\mathrm{tr}\,e^{-\beta\mathscr{H}(t_0)}\mathscr{S}(t_0,t)\mathscr{S}(t,t_0)}. \tag{2.10}$$

Here we examine the order of the time variables in Eq. (2.10). From the definition of $\mathscr{S}$ in Eq. (2.9), operators in $\mathscr{S}(t,t_0)$ [$\mathscr{S}(t_0,t)$] are arranged in the time [anti-time] order from right to left. Further, the initial density matrix, $e^{-\beta\mathscr{H}(t_0)}$, can be rewritten as

$$e^{-\beta\mathscr{H}(t_0)} = \exp\left(-i\int_{C_3}d\tau\mathscr{H}_{1\mathrm{I}}(\tau)\right),$$

where we have extended the domain of the time variable to the complex plane and C_3 is a straight contour directed from t_0 to $-i\beta + t_0$. We set $\mathscr{H}_{1\mathrm{I}}(\tau) \equiv \mathscr{H}_{1\mathrm{I}}(t_0)$ for $\tau \in C_3$. The time variables in Eq. (2.10) are now ordered along the contour with three-branches in Fig. 2-1(a).

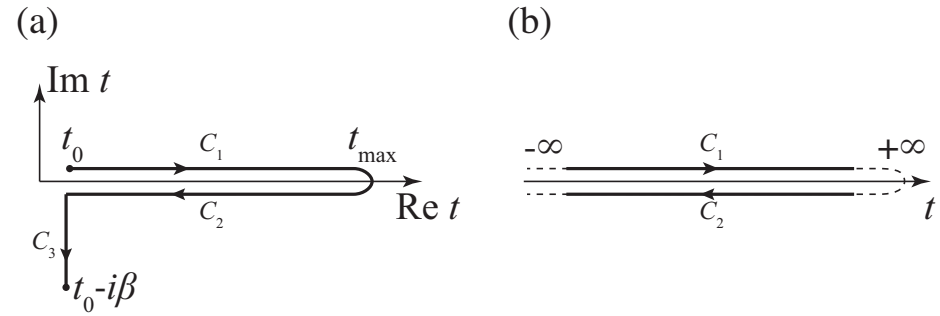

Figure 2-1: (a) L-shape contour $C = C_1 \cup C_2 \cup C_3$. $t_{\max}$ should be taken large enough to contain the time interval in which one would like to simulate. (b) Keldysh contour $C = C_1 \cup C_2$.

Therefore the expression Eq. (2.10) is formally rewritten as

$$\langle \hat{O}_{\rm H}(t) \rangle_0 = \frac{\left\langle {\rm T}_C \exp\left(-i \int_C \mathscr{H}_{1{\rm I}}(\bar{t}) d\bar{t} \right) \hat{O}_I(t) \right\rangle_0}{\left\langle {\rm T}_C \exp\left(-i \int_C \mathscr{H}_{1{\rm I}}(\bar{t}) d\bar{t} \right) \right\rangle_0},$$

where we have introduced the L-shaped contour C defined in the Fig. 2-1(a), and ${\rm T}_C$ is the time-ordering operator along the contour C. The average $\langle \cdots \rangle_0$ is defined as ${\rm tr}[\cdots \rho_0(t_0)]$ where $\rho_0(t) = e^{-\beta \mathscr{H}_0(t)}$ is the noninteracting density matrix in equilibrium. In the same way, a two-body operator (such as correlation operators) is expressed as

$$\langle {\rm T}_C \hat{A}_{\rm H}(t) \hat{B}_{\rm H}(t') \rangle_0 = \frac{\left\langle {\rm T}_C \exp\left(-i \int_C \mathscr{H}_{1{\rm I}}(\bar{t}) d\bar{t} \right) \hat{A}_I(t) \hat{B}_I(t') \right\rangle_0}{\left\langle {\rm T}_C \exp\left(-i \int_C \mathscr{H}_{1{\rm I}}(\bar{t}) d\bar{t} \right) \right\rangle_0}.$$

2.1.2 Keldysh contour

So far, we have developed the general formalism for time dependent quantum systems with a general Hamiltonian Eq. (2.1). Here, let us additionally assume that *the interaction is adiabatically switched on at the infinite past*. Due to this assumption, we can let the initial time be infinite past $t_0 \to -\infty$, and the interaction vertex between C_3 branch and $C_i\,(i = 1, 2)$ vanishes. As a result, the L-shaped contour is reduced to a two-branch contour (Keldish contour) depicted in Fig. 2-1(b). The Green's function method on this reduced two-branch contour, usually called the Keldysh formalism, is first formulated by Keldysh [43].

Let us discuss the relation between the assumption and the situations where the Keldysh formalism is applicable. The assumption of the adiabatic interaction switching-on is usually justified when the dissipation time scale $\tau_{\rm diss}$ is much shorter than the time interval between the initial time t_0 and the time $t_{\rm obs}$ at which we observe the system. This is because the information on the initial state should be wiped out in the time scale of our interest when $\tau_{\rm diss} \ll t_{\rm obs} - t_0$ holds.

Since we should assume the adiabatic switching condition, the Keldysh formalism is limited to some classes of nonequilirium many-body problems. The Keldysh formalism has been widely applied to dissipative systems, such as open systems attached to leads or thermal heat-baths [49, 35].

As we stressed in the introduction, in this thesis we study steady states of many-body systems in external electric fields. For that purpose, we always introduce heat-baths (Sec. 2.1.5), which mimics the dissipation mechanism such as phonons, effects of substrates, and so on. Therefore, the Keldysh formalism should be satisfactory for the purpose of our study.

2.1.3 Green's functions and self-energy

Hereafter, we formulate the Keldysh-Green's function formalism on the Keldysh contour in Fig. 2-1. In diagrammatic perturbation expansions, Green's functions play an important role. The Green's function on the Keldysh contour is defined as

$$iG_{\alpha\beta}(t,t') = \langle \mathrm{T}_C\, \hat{c}_{\alpha\mathrm{H}}(t)\hat{c}^\dagger_{\beta\mathrm{H}}(t')\rangle_0 = \frac{\left\langle \mathrm{T}_C \exp\left(-i\int_C \mathscr{H}_{1\mathrm{I}}(\bar{t})d\bar{t}\right)\hat{c}_{\alpha\mathrm{I}}(t)\hat{c}^\dagger_{\beta\mathrm{I}}(t')\right\rangle_0}{\left\langle \mathrm{T}_C \exp\left(-i\int_C \mathscr{H}_{1\mathrm{I}}(\bar{t})d\bar{t}\right)\right\rangle_0}, \tag{2.11}$$

where $\hat{c}_\alpha(t)$ is the fermionic operator, α and β label internal degrees of freedom (e.g. momentum, spin and band indices) and t and t' belong to the Keldysh contour C. The above expression can be expanded in powers of $\mathscr{H}_{1\mathrm{I}}(t)$, and each term corresponds to Feynman diagrams, as discussed in equilibrium cases [39] and nonequilibrium cases [40, 46, 48]:

$$iG_{\alpha\beta}(t,t') = \left\langle \mathrm{T}_C \exp\left(-i\int_C \mathscr{H}_{1\mathrm{I}}(\bar{t})d\bar{t}\right)\hat{c}_{\alpha\mathrm{I}}(t)\hat{c}^\dagger_{\beta\mathrm{I}}(t')\right\rangle_{0,\mathrm{conn}}, \tag{2.12}$$

where $\langle A(t)B(t')\rangle_{0,\mathrm{conn}}$ represents all the topologically distinct Feynman diagrams connected to the vertices of $A(t)$ and $B(t')$. The self-energy is introduced in the same way as in the equilibrium Green's function theory, and the self-energy satisfies the Dyson's equation,

$$G_{\alpha\beta}(t,t') = G^{(0)}_{\alpha\beta}(t,t') + \sum_{\gamma\delta}\iint_C d\bar{t}d\bar{t}'\, G^{(0)}_{\alpha\gamma}(t,\bar{t})\Sigma_{\gamma\delta}(\bar{t},\bar{t}')G_{\delta\beta}(\bar{t}',t'). \tag{2.13}$$

2.1.4 Properties of time-dependent Green's functions

We have defined Green's functions on the Keldysh contour in Eq. (2.11). The contour C is divided into two branches C_1 and C_2 as in Fig. 2-1. Then the Green's function on C is decomposed into 2×2 elements,

$$G^{ij}_{\alpha\beta}(t,t') = G_{\alpha\beta}(t,t') \quad \text{for} \quad t\in C_i, \quad t'\in C_j. \tag{2.14}$$

It is easily confirmed that each component of Green's functions satisfies[2]

$$G^{11}(t,t') = G^{12}(t,t'), \quad t \le t', \tag{2.15a}$$
$$G^{11}(t,t') = G^{21}(t,t'), \quad t > t', \tag{2.15b}$$
$$G^{22}(t,t') = G^{21}(t,t'), \quad t < t', \tag{2.15c}$$
$$G^{22}(t,t') = G^{12}(t,t'), \quad t \ge t'. \tag{2.15d}$$

Due to Eqs.(2.15), the 2×2 Green's function has a redundancy,

$$G^{11}(t,t') + G^{22}(t,t') = G^{12}(t,t') + G^{21}(t,t'), \quad t \ne t'. \tag{2.16}$$

We can then reduce the 2×2 Green's function, using Eq. (2.16), into a tridiagonal form,

$$\begin{pmatrix} G^R(t,t') & G^K(t,t') \\ 0 & G^A(t,t') \end{pmatrix} = L\tau_3 \begin{pmatrix} G^{11}(t,t') & G^{12}(t,t') \\ G^{21}(t,t') & G^{22}(t,t') \end{pmatrix} L^\dagger, \tag{2.17}$$

where we have introduced a rotating matrix L and a Pauli matrix τ_3,

$$L = \frac{1}{\sqrt{2}} \begin{pmatrix} 1 & -1 \\ 1 & 1 \end{pmatrix}, \quad \tau_3 = \begin{pmatrix} 1 & \\ & -1 \end{pmatrix}. \tag{2.18}$$

This procedure is called the *Keldysh rotation* after the pioneering work done by Keldysh [43]. The matrix elements of the tridiagonal matrix are called retarded Green's function $G^R(t,t')$, advanced Green's function $G^A(t,t')$ and the Keldysh Green's function $G^K(t,t')$. Their explicit forms are

$$G^R(t,t') = -i\theta(t-t')\left\langle \{c(t), c^\dagger(t')\} \right\rangle, \tag{2.19a}$$
$$G^A(t,t') = i\theta(t'-t)\left\langle \{c(t), c^\dagger(t')\} \right\rangle, \tag{2.19b}$$
$$G^K(t,t') = -i\left\langle [c(t), c^\dagger(t')] \right\rangle, \tag{2.19c}$$

where $\{A,B\} = AB + BA$ is the anticommutator. It is also useful to define the lesser [greater] Green's functions $G^<(t,t')[G^<(t,t')]$,

$$G^<(t,t') = -i\left\langle c^\dagger(t')c(t) \right\rangle = \frac{1}{2}[G^K(t,t') - G^R(t,t') + G^A(t,t')], \tag{2.20a}$$
$$G^>(t,t') = -i\left\langle c(t)c^\dagger(t') \right\rangle = \frac{1}{2}[G^K(t,t') + G^R(t,t') - G^A(t,t')]. \tag{2.20b}$$

[2] If the system has a particle-hole symmetry, Green's functions satisfy more strict constraints, which may reduce computation (see Appendix A).

One can apply the Keldysh rotation to Dyson's equation Eq. (2.13) to obtain a reduced form,

$$\begin{aligned}\begin{pmatrix} G^R & G^K \\ 0 & G^A \end{pmatrix}(t,t') &= \begin{pmatrix} G_0^R & G_0^K \\ 0 & G_0^A \end{pmatrix}(t,t') \\ &+ \iint_{-\infty}^{\infty} d\bar{t}\, d\bar{t}' \begin{pmatrix} G_0^R & G_0^K \\ 0 & G_0^A \end{pmatrix}(t,\bar{t}) \cdot \begin{pmatrix} \Sigma^R & \Sigma^K \\ 0 & \Sigma^A \end{pmatrix}(\bar{t},\bar{t}') \cdot \begin{pmatrix} G^R & G^K \\ 0 & G^A \end{pmatrix}(\bar{t}',t'). \end{aligned} \tag{2.21}$$

Here, we have introduced the retarded and advanced component of the self-energy,

$$\begin{pmatrix} \Sigma^R(t,t') & \Sigma^K(t,t') \\ 0 & \Sigma^A(t,t') \end{pmatrix} = L\tau_3 \begin{pmatrix} \Sigma^{11}(t,t') & \Sigma^{12}(t,t') \\ \Sigma^{21}(t,t') & G^{22}(t,t') \end{pmatrix} L^{\dagger}. \tag{2.22}$$

For convenience, we can also define the lesser and greater components,

$$\Sigma^{<}(t,t') = \frac{1}{2}[\Sigma^K(t,t') - \Sigma^R(t,t') + \Sigma^A(t,t')], \tag{2.23a}$$

$$\Sigma^{>}(t,t') = \frac{1}{2}[\Sigma^K(t,t') + \Sigma^R(t,t') - \Sigma^A(t,t')]. \tag{2.23b}$$

The important point in the Keldysh rotation is that the elements $G^R(t,t')$, $G^A(t,t')$, and $G^K(t,t')$ are directly connected to the electronic structure of the system. In equilibrium, we can define the spectral function $A(\omega)$, and the density of occupied states $N(\omega)$ at energy ω as

$$A(\omega) = -\frac{1}{\pi}\mathrm{Im}G^R(\omega), \quad N(\omega) = \frac{1}{2\pi}\mathrm{Im}G^{<}(\omega). \tag{2.24}$$

Also, due to the Kubo-Martin-Schwinger condition [50, 51] for the lesser and greater Green's function,

$$G^{>}(\omega) = -e^{\omega/T}G^{<}(\omega), \tag{2.25}$$

we have the fluctuation-dissipation relation,

$$G^K(t,t') = \int_{-\infty}^{\infty} \left[G^R(t,\bar{t})F(\bar{t},t') - F(t,\bar{t})G^A(\bar{t},t')\right] dt, \tag{2.26}$$

with the distribution kernel $F(t,t')$,

$$F(t,t') = \int_{-\infty}^{\infty} \frac{d\omega}{2\pi} e^{i\omega(t-t')} \tanh\left(\frac{\omega}{2T}\right) \quad \text{(in equilibrium)}. \tag{2.27}$$

In equilibrium, the Fourier transform of the kernel $F(\omega)$ is related to the distribution function $f(\omega)$ as

$$f(\omega) = \frac{1}{2}[1 - F(\omega)] = \frac{1}{e^{\omega/T}+1}. \tag{2.28}$$

In nonequilibrium, the distribution kernel $F(t,t')$ is rather defined by Eq. (2.26) and is regarded as a nonequilibrium analog of the distribution function[48].

In nonequilibrium, the Green's function $G(t,t')$ depends not only on the time interval between observations $t_{\mathrm{rel}} = t - t'$, but also on the starting time t or the average of the measurement time $t_{\mathrm{av}} = (t+t')/2$. Thus there is a slight ambiguity on the definition of the spectral

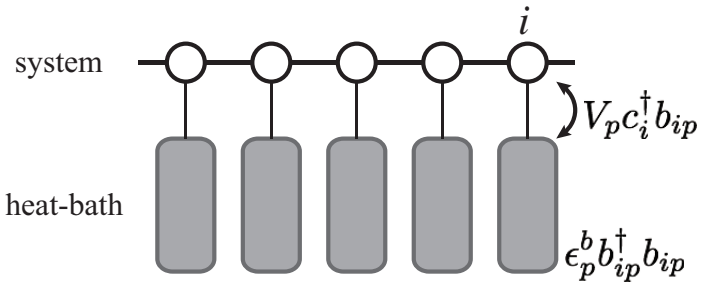

Figure 2-2: Schematic picture of the heat-bath model. Open circles represent sites in the system, whereas the shaded rectangles represent the fermionic heat-bath. The hybridization between the system and the heat-bath is expressed as $V_p c_i^\dagger b_{ip}$, whereas the heat-bath itself is represented as $\epsilon_p^b b_{ip}^\dagger b_{ip}$ in the figure. Details are explained in the text.

functions in nonequilibrium. In this thesis we employ $t_{\rm av}$ for the time-evolution of the spectral functions. Namely, the time-dependent spectral function $A(t_{\rm av},\omega)$ and occupation density $N(t_{\rm av},\omega)$ are defined as

$$A(t_{\rm av},\omega) = -\frac{1}{\pi}{\rm Im}G^R(t_{\rm av},\omega), \quad N(t_{\rm av},\omega) = \frac{1}{2\pi}{\rm Im}G^<(t_{\rm av},\omega), \tag{2.29}$$

where $G^R(t_{\rm av},\omega)$ and $G^<(t_{\rm av},\omega)$ are the Fourier transformations of $G^R(t,t')$ and $G^<(t,t')$ for $t_{\rm rel} = t - t'$, respectively.

2.1.5 Fermionic heat-bath model for dissipative systems

Electrons in real materials are always subject to dissipative environments, such as phonons, substrates, and so on. When the system is excited by applied external fields, the system finally reaches some steady state after some interaction to the dissipative environments. One way to treat such dissipations is to introduce a microscopic model for the dissipative environments, and relate the parameters of the microscopic model to some macroscopic parameters, such as a damping rate or a life-time of particles in the system.

As an example of such strategy, here we recall a pioneering work by Caldeira and Leggett [52, 53], who studied a quantum system subject to dissipative environments. They introduced an exactly solvable model for the dissipative environment, and derived a damping rate for the system as a phenomenological parameter. Following the strategy, we also introduce some exactly solvable model for dissipative environments, and derive some simple expression that serves as dissipative processes for the system.

For that purpose, it is useful to introduce a fermionic heat-bath model, described by a Hamiltonian,

$$\mathscr{H}_{\rm tot}(t) = \mathscr{H}(t) + \mathscr{H}_{\rm mix} + \mathscr{H}_{\rm bath}, \tag{2.30a}$$

where the Hamiltonian $\mathscr{H}_{\rm bath}$ of the heat-bath and the hybridization $\mathscr{H}_{\rm mix}$ between the sys-

tem and the bath are given respectively by

$$\mathscr{H}_{\rm bath} = \sum_{ip} \epsilon_p^b b_{ip}^\dagger b_{ip}, \tag{2.30b}$$

$$\mathscr{H}_{\rm mix} = \sum_{ip} \left(V_{ip} c_i^\dagger b_{ip} + {\rm h.c.} \right), \tag{2.30c}$$

where c_i is the fermionic operator at site i in the system, b_{ip} is the fermionic operator for the mode p of the bath coupled to the site i. ϵ_p^b is the energy of the mode p of the heat-bath, and V_{ip} is the strength of the hybridization between the system and the heat-bath. The heat-bath model is schematically shown in Fig. 2-2, which is first introduced by Büttiker [54] and later applied to determine the steady states of the strongly correlated systems [35]. Following the discussion in Ref. [35], we show below that the heat-bath sector is exactly solved and merged into the self-energy for the system.

Since the heat-bath term is quadratic, we can explicitly perform integration of the heat-bath degrees of freedom. To see this, let us write the system in terms of its action,

$$\begin{aligned} S_{\rm tot}[b, b^\dagger, c, c^\dagger] &= S_{\rm sys}[c, c^\dagger] \\ &+ \int_C dt \sum_{ip} \left[b_{ip}^\dagger(t)(-i\partial_t + \epsilon_p^b) b_{ip}(t) + V_{ip} c_i^\dagger(t) b_{ip}(t) + V_{ip}^* b_{ip}^\dagger(t) c_i(t) \right], \end{aligned} \tag{2.31}$$

where $S_{\rm sys}$ is the action from the Hamiltonian of the system[3] and $b, b^\dagger, c$ and $c^\dagger$ are Grassmannian variables corresponding to the fermionic field operators for the bath and the system in the Hamiltonian Eqs.(2.30). The above action is related to the total partition function as

$$Z_{\rm tot} = \int \mathscr{D}[b^\dagger, b, c^\dagger, c] e^{-iS_{\rm tot}}. \tag{2.32}$$

where $\int \mathscr{D}[b^\dagger, b, c^\dagger, c]$ represents the path integral for the variables $b^\dagger, b, c^\dagger$ and c. We introduce the noninteracting bath Green's function,

$$G_p^b(t, t') = -i \langle {\rm T}_C b_{ip}(t) b_{ip}^\dagger \rangle_0, \tag{2.33}$$

which satisfies an equation of motion,

$$(i\partial_t - \epsilon_p^b) G_p^b(t, t') = \delta_C(t, t'). \tag{2.34}$$

With this, the integration over b and $b^\dagger$ in Eq. (2.32) is explicitly performed. As a result, we obtain the effective action for the system,

$$S_{\rm eff}[c, c^\dagger] = S_{\rm sys}[c, c^\dagger] + \iint_C dt\, dt' \sum_i c_i^\dagger(t) \Sigma_{\rm diss}(t, t') c_i(t'), \tag{2.35}$$

[3] In this thesis, an action S of a field $\psi(x)$ of a fermionic particle is written as $S[\psi^\dagger, \psi]$ in order to emphasize that S is a functional of $\psi(x)$ and $\psi^\dagger(x)$. Here, x contains time t, site indices i, and internal degrees of freedom such as spins and orbitals.

where $\Sigma_{\text{diss}}(t,t')$ is the self-energy correction from the bath,

$$\Sigma_{\text{diss}}(t,t') = \sum_p |V_p|^2 G_p^b(t,t'). \tag{2.36}$$

Now, we assume the heat-bath is large enough and stays in thermal equilibrium with a temperature T. In other words, we assume that the bath Green's function is a function of $t-t'$ and satisfies the fluctuation-dissipation theorem Eqs.(2.26), (2.27),

$$[G_p^b]^R(\omega) - [G_p^b]^A(\omega) = [G_p^b]^K(\omega) F(\omega). \tag{2.37}$$

The explicit form of the Green's function is written as

$$G_p^b(\omega) = \frac{1}{\omega - \epsilon_p + i0^+}. \tag{2.38}$$

Substituting above into Eq. (2.36) with the relation $\dfrac{1}{\omega + i0^+} = \mathscr{P}\dfrac{1}{\omega} - i\pi\delta(\omega)$, we obtain

$$\Sigma_{\text{diss}}^R(\omega) = -i\Gamma, \tag{2.39a}$$

$$\Gamma = \sum_p \pi |V_p|^2 \delta(\omega - \epsilon_p^b). \tag{2.39b}$$

We have dropped the ω-dependence, assuming that the density of states of the heat-bath is constant. Now we obtain the explicit form of the dissipation self-energy as

$$\begin{pmatrix} \Sigma_{\text{diss}}^R(\omega) & \Sigma_{\text{diss}}^K(\omega) \\ 0 & \Sigma_{\text{diss}}^A(\omega) \end{pmatrix} = \begin{pmatrix} -i\Gamma & -2i\Gamma F(\omega) \\ 0 & i\Gamma \end{pmatrix}. \tag{2.40}$$

Hence we have shown that the fermionic heat-bath of the form Eq. (2.30) is incorporated in the self-energy of the system.

2.2 Dynamical mean-field theory

In this section, we briefly introduce the dynamical mean-field theory (DMFT), a powerful tool for studying strongly correlated systems with short-range interactions. As we stated in the introduction, we consider the Hubbard model on multi-orbital systems, namely,

$$\mathscr{H}(t) = \sum_{i\alpha}\sum_{j\beta}\sum_{\sigma} J_{i\alpha,j\beta}(t) c_{i\alpha\sigma}^\dagger c_{j\beta\sigma} + \sum_i \sum_\alpha U_\alpha(t) \hat{n}_{i\alpha\uparrow}\hat{n}_{i\alpha\downarrow}, \tag{2.41}$$

where i and j label the unit cell, and α and β the atomic sites in each unit cell. $J_{i\alpha,j\beta}(t)$ is the hopping matrix between two sites specified by (i,α) and (j,β). $U_\alpha(t)$ is the Hubbard interaction on the atom α. We can also express Eq. (2.41) using a Fourier transform for i and

j as

$$\mathscr{H}(t) = \sum_{\boldsymbol{k},\alpha\beta,\sigma} H_{\boldsymbol{k},\alpha\beta}(t) c^\dagger_{\boldsymbol{k}\alpha\sigma} c_{\boldsymbol{k}\beta\sigma} + \sum_i \sum_\alpha U_\alpha(t) \hat{n}_{i\alpha\uparrow} \hat{n}_{i\alpha\downarrow}, \tag{2.42a}$$

$$H_{\boldsymbol{k}(t),\alpha\beta} = \sum_{\boldsymbol{R}_i - \boldsymbol{R}_j} J_{i\alpha,j\beta}(t) e^{-i\boldsymbol{k}\cdot(\boldsymbol{R}_i - \boldsymbol{R}_j)}. \tag{2.42b}$$

DMFT was first derived by Metzner and Vollhardt [55] for the single-band Hubbard model in equilibrium. Their key observation is that, if we make the spatial dimension d infinitely large, the hopping parameters should scale as

$$t_{ij} = \frac{t^*_{ij}}{\sqrt{d}} \quad (d \to \infty), \quad t^*_{ij}\text{: constant} \tag{2.43}$$

so that the band width may not diverge nor vanish in the $d \to \infty$ limit. Here t^*_{ij} is a constant representing the band width in the limit. As a result of this scaling, it can be shown that the self-energy $\Sigma_{ij,\sigma}(t,t')$, which contains local ($i = j$) and non-local ($i \neq j$) correlations, should satisfy

$$\Sigma_{ij,\sigma}(\omega) = \Sigma_{ii,\sigma}(\omega)\delta_{ij}, \tag{2.44}$$

in the limit of infinite spatial dimension. In this subsection we briefly formulate the DMFT in $d \to \infty$ limit, based on Ref. [56], and show that the approximation of neglecting the nonlocal correlation Eq. (2.44) leads to the self-consistency equations for the Green's functions.

Here we briefly mention how DMFT works in realistic models. As we have stated, DMFT mathematically gives an exact result in the limit of infinite dimensions $d \to \infty$ with the scaling Eq. (2.43), and can be used as an approximation for systems in finite dimensions. As we discuss below, DMFT can surprisingly describe metal-insulator transitions, one of the most important phenomena in strongly correlated systems, without any bias. The Hamiltonian Eq. (2.41) consists of two competing terms, the kinetic term that makes electrons delocalized, and the interaction term that localizes electrons by imposing the Coulomb repulsion with each other. Due to these opposite tendencies, correlated electron systems are roughly divided into weakly correlated metals and strongly correlated insulators [5]. Whether the two phases are described by the same Hamiltonian is therefore one important milestone for numerical methods of strongly correlated electron systems. DMFT indeed describes metal-insulator transitions even for the finite-dimensional systems [57].

The formalism for equilibrium Green's functions can also be extended to the non-equilibrium Green's function method by considering the extended L-shaped or Keldysh contour [58, 35]. For a review on nonequilirium DMFT and its application, see Ref. [32].

2.2.1 Self-consistency equations

Here we briefly sketch the derivation of DMFT formalism. For a detailed review on DMFT, see e.g. Ref. [56]. Let us consider the system with the Hamiltonian Eq. (2.41) in terms of its

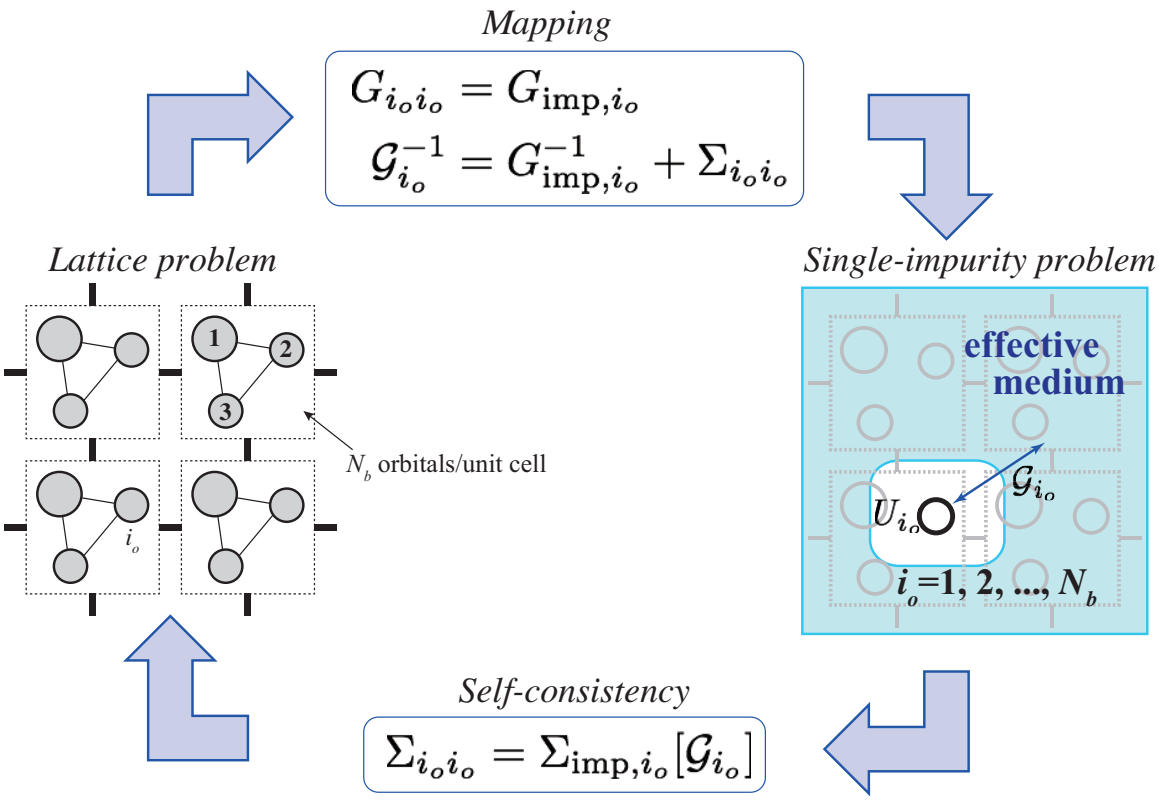

Figure 2-3: Schematics of DMFT self-consistency loop, here depicted for multi-band cases. We take multi-band systems with N_b atoms per unit cell. We have therefore N_b impurity problems to be solved.

action S given by

$$S[c^\dagger, c] = \int_C dt \left[\sum_{i\sigma} c^\dagger_{i\sigma}(t)(-i\partial_t - \mu) c_{j\sigma}(t) + \sum_{ij\sigma} J_{ij}(t) c^\dagger_{i\sigma}(t) c_{j\sigma}(t) + \sum_i U_i(t) \hat{n}_{i\uparrow}(t) \hat{n}_{i\downarrow}(t) \right]. \quad (2.45)$$

The action is related to the partition function Z as

$$Z = \int \mathcal{D}[c^\dagger, c] e^{-iS[c^\dagger, c]}. \quad (2.46)$$

The underlying idea of DMFT is to apply the mean-field picture to correlated lattice problems. In a mean-field picture, one focuses on a certain site and regards the other surrounding sites as an effective medium. As a result, the lattice problem is reduced to a single site problem in an effective medium.

Based on the mean-field picture, we focus on a site i_o in our system. In order to obtain the effective theory on the site i_o, we integrate out the variables $c^\dagger_{i\sigma}$ and $c_{i\sigma}$ except for the

site i_o. Performing this integration one obtains the effective action for the single site i_o:

$$S_{\mathrm{imp}}[c^\dagger_{i_o}, c_{i_o}] = \int_C dt \left[\sum_\sigma c^\dagger_{i_o\sigma}(t)(-i\partial_t - \mu) c_{i_o\sigma}(t) + U_{i_o}(t)\hat{n}_{i_o\uparrow}(t)\hat{n}_{i_o\downarrow}(t) \right] + \iint_C dt\, dt' \sum_\sigma c^\dagger_{i_o\sigma}(t)\Delta_\sigma(t,t')c_{i_o\sigma}(t). \tag{2.47}$$

Here, $\Delta_\sigma(t,t')$ is a certain scalar function specified by the one-body terms that hybridize the i_o-site and surrounding sites. $\Delta_\sigma(t,t')$ is therefore called "the hybridization function". In addition to the hybridization term, there are additional four-point ($c^\dagger c^\dagger cc$) terms or even higher-order terms in the effective action for the i_o-site. The key finding by Metzner and Volhardt [55] is that these higher-order contributions vanish due to the scaling Eq. (2.43) of the hopping parameters.

The effective action is nothing but the action of the single-impurity problem,

$$S_{\mathrm{imp}}[c^\dagger_{i_o}, c_{i_o}] = \iint_C dt\, dt' \sum_\sigma c^\dagger_{i_o\sigma}(t)[-\mathcal{G}^{-1}_\sigma(t,t')]c_{i_o\sigma}(t) + \int_C dt\, U_{i_o}(t)\hat{n}_{i_o\uparrow}(t)\hat{n}_{i_o\downarrow}(t), \tag{2.48}$$

with an effective single-particle Green's function $\mathcal{G}_\sigma(t,t') = i\partial_t + \mu - \Delta_\sigma(t,t')$. After solving the single-impurity problem, we obtain the impurity Green's function $G_{\mathrm{imp}}(t,t')$ and self-energy $\Sigma_{\mathrm{imp}}(t,t')$ with a relation,

$$G^{-1}_{\mathrm{imp},\sigma}(t,t') = \mathcal{G}^{-1}_\sigma(t,t') - \Sigma_{\mathrm{imp},\sigma}(t,t'). \tag{2.49}$$

In addition, we should impose the self-consistency between the original lattice problem Eq. (2.45) and the impurity problem Eq. (2.47). Since the two actions should be equivalent for the i_o-th site, local quantities such as $G_{i_o,i_o,\sigma}$ should also coincide. Therefore we have the self-consistency condition,

$$G_{i_o,i_o,\sigma}(t,t') = G_{\mathrm{imp},\sigma}(t,t'), \quad \Sigma_{i_o,i_o,\sigma}(t,t') = \Sigma_{\mathrm{imp},\sigma}(t,t'). \tag{2.50}$$

In DMFT, we solve Eq. (2.47), Eq. (2.49) and Eq. (2.50) self-consistently. The schematic picture of DMFT is depicted in Fig. 2-3.

Here, we formulate the explicit DMFT self-consistency loop for multi-orbital Hubbard model with the Hamiltonian Eq. (2.42) as

$$\underline{G}^{-1}_{\boldsymbol{k}}(t,t') = \underline{G}^{-1}_{0\boldsymbol{k}}(t,t') - \underline{\Sigma}_{\mathrm{diss}}(t,t') - \Sigma(t,t'), \tag{2.51a}$$
$$\underline{G}_{\mathrm{loc}}(t,t') = \sum_{\boldsymbol{k}} \underline{G}_{\boldsymbol{k}}(t,t'), \tag{2.51b}$$
$$\underline{\mathcal{G}}^{-1}(t,t') = \underline{G}^{-1}_{\mathrm{loc}}(t,t') + \underline{\Sigma}(t,t'), \tag{2.51c}$$
$$\underline{\Sigma}(t,t') = \underline{\Sigma}_{\mathrm{DMFT}}[\underline{\mathcal{G}}](t,t'). \tag{2.51d}$$

In the last equation, one solves a single-impurity problem Eq. (2.48) and obtain the self-

energy of the system. Here we have introduced a notation for triangular matrices of the Keldysh Green's function,

$$\underline{G}(t,t') \equiv \begin{pmatrix} G^R(t,t') & G^K(t,t') \\ 0 & G^A(t,t') \end{pmatrix}.$$

The noninteracting Green's function $\underline{G}_{0\boldsymbol{k}}(t,t')$ is written in an explicit form as

$$\begin{aligned} \underline{G}^{-1}_{0\boldsymbol{k}}(t,t') &= \begin{pmatrix} (G^{-1}_{0\boldsymbol{k}})^R & (G^{-1}_{0\boldsymbol{k}})^K \\ 0 & (G^{-1}_{0\boldsymbol{k}})^A \end{pmatrix}(t,t') \\ &= \begin{pmatrix} \delta(t-t'-0^+)[i\mathbf{1}\partial_t - H_{\boldsymbol{k}}(t)] & 0 \\ 0 & \delta(t-t'+0^+)[i\mathbf{1}\partial_t - H_{\boldsymbol{k}}(t)] \end{pmatrix}(t,t') \end{aligned} \tag{2.52}$$

with an $N_b \times N_b$ matrix $[H_{\boldsymbol{k}}(t)]_{\alpha\beta} = H_{\boldsymbol{k},\alpha\beta}(t)$ and the identity matrix $\mathbf{1}$. We have introduced retarded, advanced and Keldysh components for an inverse $\underline{G}^{-1}$ of the triangular matrix $\underline{G}$ as

$$\underline{G} = \begin{pmatrix} G^R & G^K \\ 0 & G^A \end{pmatrix}, \quad \underline{G}^{-1} = \begin{pmatrix} (G^{-1})^R & (G^{-1})^K \\ 0 & (G^{-1})^A \end{pmatrix}.$$

One can easily verify

$$(G^{-1})^R = (G^R)^{-1}, \quad (G^{-1})^A = (G^A)^{-1}, \quad (G^{-1})^K = -(G^R)^{-1}\cdot(G^K)\cdot(G^A)^{-1},$$

from the relation $\underline{G}\cdot\underline{G}^{-1} = \mathrm{diag}\{\mathbf{1},\mathbf{1}\}$.

2.2.2 Iterative perturbation theory (IPT) as an impurity solver

We have shown that lattice problems of correlated electrons are mapped to a single impurity problem in equilibrium and nonequilibrium situations, by neglecting the nonlocal electron correlations. There are a lot of techniques for solving the single impurity problem in thermal equilibrium (or ground state), such as exact diagonalization, numerical renormalization group, quantum Monte Carlo, etc. [56]. On the other hand, in time-dependent systems, the computational time for solving the impurity problems can become quite large, since the size of the Green's function becomes much larger due to the real-time branch. The difficulty in the computational time becomes even harder when we consider multi-band systems or long time behavior of the system. Therefore, in this thesis, we apply some perturbation methods for the single impurity problems which only require reasonable computational time.

Here, we use one of the most straightforward techniques, that is, weak coupling perturbation. The single impurity problem is explicitly written as

$$S = \sum_\sigma \int_C dt\, dt'\, c^\dagger_\sigma(t)[-\mathcal{G}^{-1}_\sigma(t,t')]c_\sigma(t') + \int_C dt\, U n_\uparrow(t) n_\downarrow(t). \tag{2.53}$$

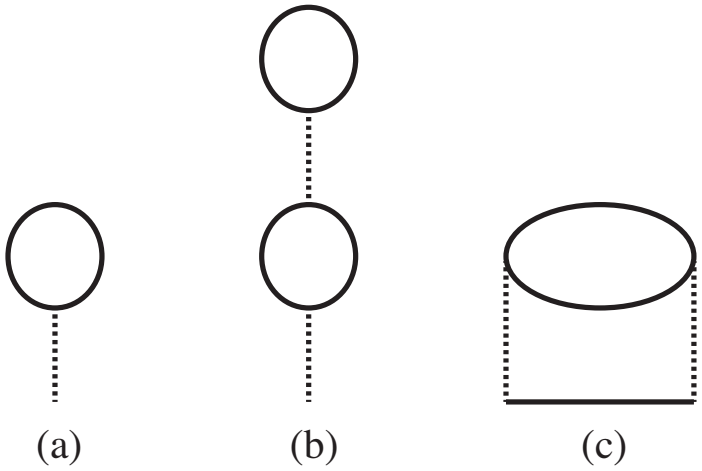

Figure 2-4: Feynman diagrams up to the second order. Solid lines and dashed lines represent modified noninteracting Green's function $\tilde{\mathcal{G}}$ and interaction U, respectively.

Note that one can always introduce c-numbers $\alpha_{\uparrow,\downarrow}$ and rewrite the impurity problem as

$$
\begin{aligned}
S &= S_0 + S_1, \\
S_0 &= \sum_\sigma \int_C dt\, dt'\, c_\sigma^\dagger(t)[\mathcal{G}_\sigma^{-1}(t,t') + (\mu - U\alpha_\sigma)\delta_C(t,t')]c_\sigma(t'), \qquad (2.54) \\
S_1 &= \int_C dt\, U\left[n_\uparrow(t) - \alpha_\downarrow\right]\left[n_\downarrow(t) - \alpha_\uparrow\right]. \qquad (2.55)
\end{aligned}
$$

That is, one can shift the chemical potential in the noninteracting Green's function as

$$
\tilde{\mathcal{G}}_\sigma^{-1}(t,t') := \mathcal{G}_\sigma^{-1}(t,t') + U\alpha_\sigma\delta_C(t,t'), \qquad (2.56)
$$

and expand S_1 in terms of the modified Green's function $\tilde{\mathcal{G}}$. The free parameters α_σ can be arbitrarily chosen and do not give any difference provided the perturbative expansion is exactly performed. In a finite-order perturbation, however, the results may depend on the choice of α. The idea of the modification of α-parameter is recently studied [59] for the study of nonequilibrium dynamics of the Hubbard model away from half-filling.

Following the Feynman rule, the self-energy up to the second order (Fig. 2-4) is obtained as

$$
\begin{aligned}
\Sigma_\sigma(t,t')^{\lessgtr} &= U(n_{\bar\sigma}(t) - \alpha_\sigma - i\chi_{\bar\sigma}^{\lessgtr}(t))\delta(t-t') \\
&\quad + U^2\tilde{\mathcal{G}}_\sigma(t,t')^{\lessgtr}\tilde{\mathcal{G}}_{\bar\sigma}(t,t')^{\lessgtr}\tilde{\mathcal{G}}_{\bar\sigma}(t',t)^{\gtrless}, \qquad (2.57)
\end{aligned}
$$

where the lesser [greater] components $G^<$ [$G^>$] of the self-energy is defined in Eq. (2.20) and $\chi_\sigma^{\lessgtr}(t)$ is defined as

$$
\chi_\sigma(t) = \begin{cases} \chi_\sigma^<(t) & t \in C_1, \\ \chi_\sigma^>(t) & t \in C_2, \end{cases} \qquad (2.58)
$$

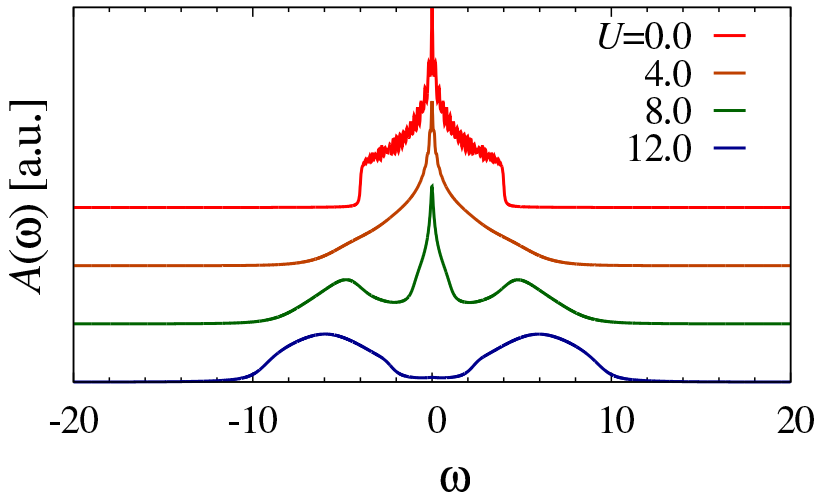

Figure 2-5: Equilibrium density of states of the two-dimensional Hubbard model at half-filling for U increased from 0 to 12. $T = 0.1J$.

where $\chi_\sigma(t)$ is the contribution from the integral for the internal particle lines in Fig. 2-4(b),

$$\chi_\sigma(t) = \int_C d\bar{t} U[n_\sigma(\bar{t}) - \alpha_{\bar{\sigma}}]\tilde{\mathcal{G}}_{\bar{\sigma}}(t,\bar{t})\tilde{\mathcal{G}}_{\bar{\sigma}}(\bar{t},t), \quad t \in C. \tag{2.59}$$

$\bar{\sigma}$ denotes the inversion of the spin index: $\bar{\sigma} = -\sigma$. Derivation of this equation is summarized in Appendix B. Note that the tadpole term (Hartree term) contains the α-parameter, which comes from the modified interaction term S_1. Since the chemical potential is subtracted by $U\alpha_\sigma$, the relation between the lattice Green's functions and self-energy is then given by

$$G^{-1}_{\boldsymbol{k}\sigma}(t,t') = \delta(t,t')\left[i\partial_t - H^{(0)}_{\boldsymbol{k}} - (\mu - U\alpha_\sigma)\mathbf{1}\right] - \Sigma_\sigma(t,t'). \tag{2.60}$$

We still have the freedom of choosing α so that the perturbation theory may give reasonable results. One suitable way is to choose α in such a way that some series of diagrams are automatically taken into the lowest perturbation term, the Hartree term. Therefore, in this thesis we choose α so that it may coincide with the occupation number,

$$\alpha_{\bar{\sigma}} = n_\sigma. \tag{2.61}$$

Due to this choice, the tadpole contribution vanishes and the self-energy up to the second-order is given by

$$\Sigma_\sigma(t,t')^{\lessgtr} = U^2\tilde{\mathcal{G}}_\sigma(t,t')^{\lessgtr}\tilde{\mathcal{G}}_{\bar{\sigma}}(t,t')^{\lessgtr}\tilde{\mathcal{G}}_{\bar{\sigma}}(t',t)^{\gtrless}. \tag{2.62}$$

At half-filling, it is known that the self-energy in the formula Eq. (2.62) gives reasonable results, not only in weakly correlated region but, surprisingly, also in the Mott insulator region with strong correlation. The reason for this is that the expression Eq. (2.62) accidentally gives the exact result in the $U \to \infty$ limit of the impurity problem [60, 61].

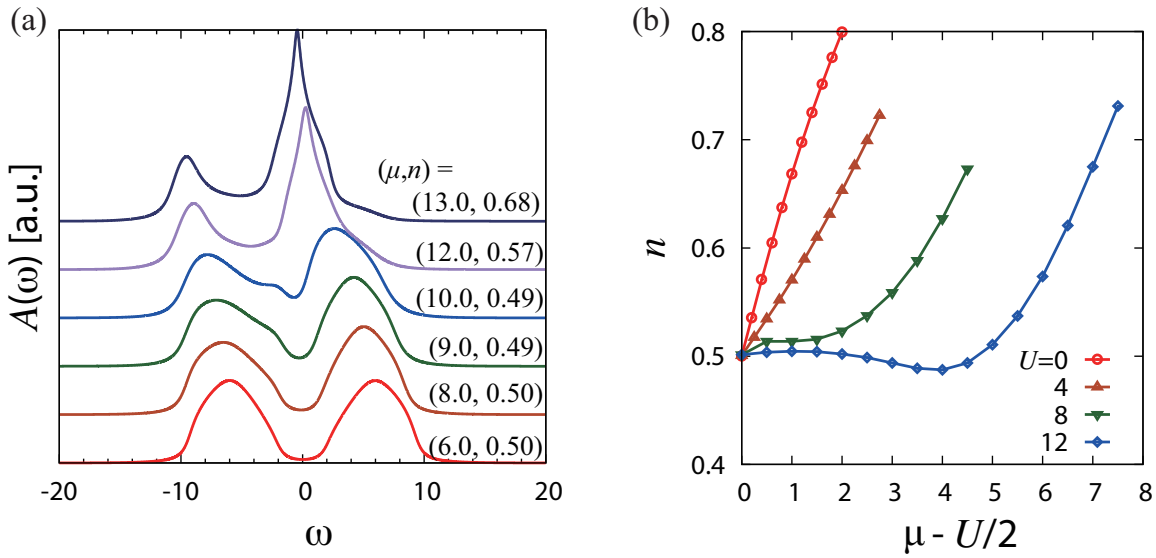

Figure 2-6: (a) Equilibrium density of states of the two-dimensional Hubbard model away from half-filling, for $U = 12J$ and $T = 0.5J$. Here the chemical potential μ is increased from 6.0 (half-filling) to 12. The filling n is shown for each μ. (b) Electron filling n against chemical potential μ for $U = 12J$ and $T = 0.1J$.

In order to check the validity of the approximation, we have solved the two-dimensional Hubbard model in equilibrium both at half-filling and away from half-filling. In Fig. 2-5 we show the density of states of the Hubbard model for several values of U. As U is increased, the Hubbard bands develop at $\omega = \pm U/2$, while the quasiparticle contribution around the Fermi level $\omega = 0$ decreases. At $U \simeq 10$ the quasiparticle disappears and a metal-insulator transition occurs.

In Fig. 2-6(a) we show how the metal-insulator transition takes place when the chemical potential is changed from $\mu = U/2$ (half-filling) at $U = 12$. Around $\mu = 12$ we observe the band-filling-controlled metal-insulator transition. Electron filling against the chemical potential is shown in Fig. 2-6(b). For $U = 12$, the filling is pinned at 0.5 for $0 < \mu - U/2 < 4$ and increases outside the region, indicating a filling controlled Mott transition near $\mu - U/2 \simeq 4$. This behavior qualitatively agrees with previous studies on filling controlled Mott transitions studied by several authors [60, 62, 63]. Kajueter and Kotliar [60, 62] studied μ-dependences of the spectral function and occupation number for the Hubbard model, with DMFT and a modified version of IPT. Although critical values of μ for the phase transition differ for each paper since they use different impurity solvers, our calculation qualitatively agrees with their results. In Chapter 4, we apply IPT with the condition Eq. (2.61) as the simplest approximation for the *dp*-model, where the steady states in strongly correlated multi-band systems are studied for the first time.

2.3 Nonequilibrium Kubo formula

In this section, we develop the Kubo formula for optical conductivities in nonequilibrium. We restrict our Hamiltonian to the class given by Eq. (2.42), for which we further specify the time-dependence as

$$\mathscr{H} = \sum_{\boldsymbol{k},\alpha\beta} H^{(0)}_{\alpha\beta}(\boldsymbol{k}+\boldsymbol{A}(t)) c^\dagger_{\alpha\boldsymbol{k}} c_{\beta\boldsymbol{k}} + \mathscr{H}_{\rm int}, \tag{2.63}$$

where α and β are band indices and $\boldsymbol{A}(t)$ is the vector potential that describes a spatially uniform external electric field $\boldsymbol{E}(t) = -\partial_t \boldsymbol{A}(t)$. Here we have incorporated the external field via Peierls substitution [64], substituting $\boldsymbol{k} \to \boldsymbol{k} + \boldsymbol{A}(t)$ into the static Hamiltonian $H^{(0)}(\boldsymbol{k})$. The electron charge $-e$ is set to -1 hereafter.

Current operator and correlation functions

The current operator is defined as the derivative of $\mathscr{H}$ with respect to $\boldsymbol{A}(t)$,

$$\begin{aligned}
\boldsymbol{j}(t) &= -\frac{1}{\Omega_{\rm vol}} \frac{\delta \mathscr{H}}{\delta \boldsymbol{A}(t)} \\
&= -\frac{1}{\Omega_{\rm vol}} \sum_{\boldsymbol{k},\alpha\beta} \frac{\partial H^{(0)}_{\alpha\beta}(\boldsymbol{k}+\boldsymbol{A}(t))}{\partial \boldsymbol{k}} c^\dagger_{\alpha\boldsymbol{k}} c_{\beta\boldsymbol{k}} \\
&= -\frac{1}{\Omega_{\rm vol}} \sum_{\boldsymbol{k},\alpha\beta} \boldsymbol{v}_{\alpha\beta,\boldsymbol{k}}(t) c^\dagger_{\alpha\boldsymbol{k}} c_{\beta\boldsymbol{k}}.
\end{aligned} \tag{2.64}$$

Here, $\Omega_{\rm vol}$ is the volume of the system and $\boldsymbol{v}_{\alpha\beta,\boldsymbol{k}}(t)$ is the current matrix defined by

$$\boldsymbol{v}_{\alpha\beta,\boldsymbol{k}}(t) = \frac{\partial H^{(0)}_{\alpha\beta}(\boldsymbol{k}+\boldsymbol{A}(t))}{\partial \boldsymbol{k}}. \tag{2.65}$$

Taking the statistical average at time t, we obtain an expression,

$$\langle \boldsymbol{j}(t) \rangle = \frac{i}{\Omega_{\rm vol}} \sum_{\boldsymbol{k},\alpha\beta} \boldsymbol{v}_{\alpha\beta,\boldsymbol{k}}(t) G^<_{\beta\alpha\boldsymbol{k}}(t,t).$$

Hereafter, we abbreviate the $N_b \times N_b$ matrix $(G_{\alpha\beta})$ as G. The current is then written as the trace of the matrix product of $G^<$ and $v_{\boldsymbol{k}}$,

$$\langle \boldsymbol{j}(t) \rangle = \frac{i}{\Omega_{\rm vol}} {\rm tr} \sum_{\boldsymbol{k}} \boldsymbol{v}_{\boldsymbol{k}}(t) G^<_{\boldsymbol{k}}(t,t). \tag{2.66}$$

Now we regard that the field $\boldsymbol{A}(t)$ is divided in two parts,

$$\boldsymbol{A}(t) = \boldsymbol{A}_{\rm pump}(t) + \boldsymbol{A}_{\rm probe}(t), \tag{2.67}$$

where $\boldsymbol{A}_{\rm pump}(t)$ is the (strong) field that is steadily applied to the system, while $\boldsymbol{A}_{\rm probe}(t)$ is a weak field that probes the nonequilibrium states. The optical conductivity is then defined by

the derivative with respect to the probe field,

$$\sigma^{ij}(t,t') \equiv \frac{\delta\langle j^i(t)\rangle}{\delta E^j_{\text{probe}}(t')}, \tag{2.68}$$

where $\boldsymbol{E}_{\text{probe}}(t) = -\partial_t \boldsymbol{A}_{\text{probe}}(t)$. We also define the current-current correlation function,

$$\chi^{ij}(t,t') \equiv \frac{\delta\langle j^i(t)\rangle}{\delta A^j_{\text{probe}}(t')}. \tag{2.69}$$

In the linear response we can choose the probe field as sinusoidally oscillating, $\boldsymbol{A}_{\text{probe}}(t) \propto e^{-i\omega t}$. Then, due to the relation $\boldsymbol{E}_{\text{probe}}(t) = i\omega \boldsymbol{A}_{\text{probe}}(t)$, the conductivity $\sigma_{ij}(t,t')$ and the correlation function $\chi_{ij}(t,t')$ are related as

$$\sigma_{ij}(t,t') = \frac{1}{i\omega}\chi_{ij}(t,t'). \tag{2.70}$$

Substituting the current Eq. (2.66) into the expression for the correlation function Eq. (2.69) we have

$$\chi^{ij}(t,t') = \frac{i}{\Omega_{\text{vol}}}\text{tr}\sum_{\boldsymbol{k}}\left[\delta(t-t')\mu^{ij}(t)G^<_{\boldsymbol{k}}(t,t) + v^i_{\boldsymbol{k}}(t)\frac{\delta G^<_{\boldsymbol{k}}(t,t)}{\delta A^j(t')}\right], \tag{2.71}$$

$$\mu^{ij}(t) = \frac{\partial^2 H^{(0)}(\boldsymbol{k}+\boldsymbol{A}(t))}{\partial k^i \partial k^j}. \tag{2.72}$$

The first term in Eq. (2.71) is called the diamagnetic part (χ_{dia}), while the second term is the paramagnetic part (χ_{pm}). The paramagnetic part contains "vertex corrections" in terms of Green's function expansion as shown below.

Vertex correction

To obtain the detailed expression for χ_{pm}, we need to calculate $\delta G^<_{\boldsymbol{k}}(t,t)/\delta A^j(t')$. We note the Dyson equation,

$$\left[(G^{-1}_{0\boldsymbol{k}} - \Sigma)\star G_{\boldsymbol{k}}\right](t,t') = \delta_C(t,t'), \tag{2.73a}$$

$$G^{-1}_{0\boldsymbol{k}}(t,t') = \delta_C(t,t')[i\mathbf{1}\partial^C_t - H^{(0)}(\boldsymbol{k}+\boldsymbol{A}(t))], \tag{2.73b}$$

where $\star$ denotes the convolution, $(F\star G)(t,t') \equiv \int_C d\bar{t} F(t,\bar{t})G(\bar{t},t')$ and $\delta_C(t,t')$ is the Kronecker delta on the contour C. From Eqs.(2.73) we have

$$\begin{aligned}\frac{\delta G_{\boldsymbol{k}}(t,t)}{\delta A^j(t')} &= -\int_C d\bar{t}d\bar{t}' G_{\boldsymbol{k}}(t,\bar{t})\left[\frac{\delta G^{-1}_{0\boldsymbol{k}}(\bar{t},\bar{t}')}{\delta A^j(t')} - \frac{\delta\Sigma(\bar{t},\bar{t}')}{\delta A^j(t')}\right]G_{\boldsymbol{k}}(\bar{t}',t) \\ &= \int_C d\bar{t}d\bar{t}' G_{\boldsymbol{k}}(t,\bar{t})\left[v^j_{\boldsymbol{k}}(t')\delta_C(\bar{t},\bar{t}')\delta_C(\bar{t},t') + \frac{\delta\Sigma(\bar{t},\bar{t}')}{\delta A^j(t')}\right]G_{\boldsymbol{k}}(\bar{t}',t).\end{aligned} \tag{2.74}$$

The first term in the angle brackets gives a bubble diagram for the susceptibility, while the second term gives the vertex correction.

In equilibrium, the vertex correction does not contribute to the susceptibility within DMFT [65, 66, 67]. Let us assume that our system is in equilibrium and has a spatial inversion symmetry against $\boldsymbol{k} \to -\boldsymbol{k}$. Due to this assumption, the Green's function $G_{\boldsymbol{k}}(t,t')$ and the current matrix $\boldsymbol{v}_{\boldsymbol{k}}(t)$ are even and odd functions of $\boldsymbol{k}$, respectively. Thus the bubble and the vertex correction terms in Eq. (2.74) are odd and even in total, respectively. If one substitutes Eq. (2.74) into the susceptibility Eq. (2.71) and takes the summation over $\boldsymbol{k}$, the vertex correction therefore vanishes while the bubble term remains.

This argument breaks down in nonequilibrium, since the inversion symmetry explicitly breaks down due to external fields. In fact, it is known that the vertex gives non-vanishing contribution to the conductivity [35]. Although the vertex correction is present in general, we ignore the vertex correction as a first approximation throughout this thesis. Since the vertex correction comes from the higher-order contributions of the self-energy, this approximation becomes exact in noninteracting cases, and should work at least in the weak coupling region, as we shall see in study the honeycomb-Hubbard model in Chapter 5.

Nonequilibrium Kubo formula for optical conductivities

Within the approximation we have a simple expression,

$$\frac{\delta G^<_{\boldsymbol{k}}(t,t)}{\delta A^j(t')} = G^T_{\boldsymbol{k}}(t,t')v^j_{\boldsymbol{k}}(t')G^<_{\boldsymbol{k}}(t',t) - G^<_{\boldsymbol{k}}(t,t')v^j_{\boldsymbol{k}}(t')G^{\tilde{T}}_{\boldsymbol{k}}(t',t). \tag{2.75}$$

Substituting the above expression to Eq. (2.71), we have

$$\begin{aligned}\chi^{ij}(t,t') = {}& \frac{i}{\Omega_{\mathrm{vol}}}\delta(t-t')\mathrm{tr}\sum_{\boldsymbol{k}}\mu^{ij}_{\boldsymbol{k}}(t)G^<_{\boldsymbol{k}}(t,t) \\ & + \frac{i}{\Omega_{\mathrm{vol}}}\mathrm{tr}\sum_{\boldsymbol{k}}\left[v^i_{\boldsymbol{k}}(t)G^R_{\boldsymbol{k}}(t,t')v^j_{\boldsymbol{k}}(t')G^<_{\boldsymbol{k}}(t',t) + v^i_{\boldsymbol{k}}(t)G^<_{\boldsymbol{k}}(t,t')v^j_{\boldsymbol{k}}(t')G^A_{\boldsymbol{k}}(t',t)\right].\end{aligned} \tag{2.76}$$

Plugging Eq. (2.76) into Eq. (2.70), we finally obtain the expression for the optical conductivity as

$$\begin{aligned}\sigma^{ij}(t,t') = {}& \frac{1}{\omega}\delta(t-t')\frac{1}{\Omega_{\mathrm{vol}}}\mathrm{tr}\sum_{\boldsymbol{k}}\mu^{ij}_{\boldsymbol{k}}(t)G^<_{\boldsymbol{k}}(t,t') \\ & + \frac{1}{\omega}\frac{1}{\Omega_{\mathrm{vol}}}\mathrm{tr}\sum_{\boldsymbol{k}}\left[v^i_{\boldsymbol{k}}(t)G^R_{\boldsymbol{k}}(t,t')v^j_{\boldsymbol{k}}(t')G^<_{\boldsymbol{k}}(t',t) + v^i_{\boldsymbol{k}}(t)G^<_{\boldsymbol{k}}(t,t')v^j_{\boldsymbol{k}}(t')G^A_{\boldsymbol{k}}(t',t)\right].\end{aligned} \tag{2.77}$$

This is the formula for the optical conductivities in nonequilibrium for multi-band systems. We shall further obtain the formula, based on Eq. (2.77), for ac-driven systems in terms of Floquet-Green's functions in the next chapter.

In some cases, it is better to rewrite the volume as $\Omega_{\mathrm{vol}} = N_c\Omega_{\mathrm{cell}}$ with the number of unit cells N_c and the volume of the unit cell Ω_{cell}. N_c coincides with the number of $\boldsymbol{k}$-points. Ω_{cell} is a^2 for a two-dimensional square lattice or the dp-model with the length a of the unit cell, and $\sqrt{3}a^2/2$ for the honeycomb lattice with distance a between the nearest neighbor sites.

Chapter 3

Floquet theory and its applications to multi-band systems

In this chapter, we review the Floquet theory, a theoretical framework for periodically driven quantum systems. As we show in Sec.3.1, the time-dependent systems with a periodic Hamiltonian, $\mathscr{H}(t+T) = \mathscr{H}(t)$, has stationary solutions called "Floquet states", the temporal analog of Bloch states in spatially periodic systems. Choosing the set of Floquet states as a basis, one can reduce the procedure of solving the time-dependent Schrödinger equation to an eigenvalue problem of Hermitian matrices with finite dimensions.

As we have discussed in the previous chapter, we are interested in steady states of correlated systems. We shall show, after Ref. [35], that the method of Floquet theory can be applied to the Keldysh-Green's function theory for dissipative systems. We shall apply the Floquet theory and obtain the DMFT formula and Kubo formula, which have been derived in the previous chapter, in terms of Floquet Green's functions. This is the first application of Floquet-DMFT method to multi-band systems.

In noninteracting systems in ac-fields, it is also known that the Floquet states can carry non-trivial Chern density (Berry curvature) in the $\boldsymbol{k}$-space. We shall also, for the first time, clarify the relation between the photo-induced Berry curvature and the nonequilibrium Kubo formula for the Hall conductivity.

3.1 Floquet theorem

We start with deriving the Floquet theorem in time-periodic systems, the temporal analog of the Bloch theorem in lattice systems in equilibrium. Suppose that our Hamiltonian is T-periodic in time. The time-dependent Shrödinger equation is written as

$$[\mathscr{H}(t) - i\partial_t]|\psi(t)\rangle = 0, \tag{3.1}$$

where $\mathscr{H}(t)$ is the time-dependent Hamiltonian with a period T,

$$\mathscr{H}(t+T) = \mathscr{H}(t). \tag{3.2}$$

Next, we extend the Hilbert space by adding an extra time axis. In order to avoid confusion with notation, let us regard a time-dependent state $|\psi(t)\rangle$ as an image of a function $\psi : \mathbb{R} \ni t \mapsto |\psi(t)\rangle \in \mathscr{V}_{\mathrm{H}}$, where $\mathscr{V}_{\mathrm{H}}$ is the Hilbert space, and introduce the "extended" Hilbert space $\tilde{\mathscr{V}}_{\mathrm{H}} = \mathscr{V}_{\mathrm{H}} \otimes \mathscr{F}$ to which ψ belongs. Then the operator $\mathscr{H}(t) - i\partial_t$ is a linear operator acting on $\tilde{\mathscr{V}}_{\mathrm{H}}$. Now, let us introduce the time-translation operator $\tilde{T} : \tilde{\mathscr{V}}_{\mathrm{H}} \to \tilde{\mathscr{V}}_{\mathrm{H}}$ defined by

$$|\tilde{\mathscr{T}}\psi(t)\rangle = |\psi(t+T)\rangle. \tag{3.3}$$

$\tilde{\mathscr{T}}$ forms an Abelian group $G := \{\mathbf{1}, \tilde{\mathscr{T}}, \tilde{\mathscr{T}}^2, \cdots\}$. From the periodicity Eq. (3.2), $\tilde{\mathscr{T}}$ commutes with $\mathscr{H}(t) - i\partial_t$. Therefore, the solutions ψ_α of Eq. (3.1) can be chosen so that each of them is one-dimensional representation of the Abelian group G,

$$\tilde{\mathscr{T}}\psi_\alpha = C_\alpha \psi_\alpha =: e^{-i\epsilon_\alpha T}\psi_\alpha, \tag{3.4}$$

where we have defined the *quasienergy* ϵ_α, that characterizes the one-dimensional representation. Equation (3.4) assures that $|u_\alpha(t)\rangle := e^{i\epsilon_\alpha t}|\psi_\alpha(t)\rangle$ is T-periodic in time. Substituting into Eq. (3.1), we obtain a set of equations,

$$\psi_\alpha(t) = e^{-i\epsilon_\alpha t}u_\alpha(t), \tag{3.5a}$$

$$u_\alpha(t) = u_\alpha(t+T), \tag{3.5b}$$

$$\epsilon_\alpha u_\alpha(t) = [\mathscr{H}(t) - i\partial_t]u_\alpha(t), \tag{3.5c}$$

or, taking the discrete Fourier transform for t, we obtain an eigenvalue problem,

$$\sum_n (\hat{\mathscr{H}}_{mn} - n\Omega\delta_{mn})u_{\alpha,n} = \epsilon_\alpha u_{\alpha,m}, \tag{3.6}$$

where we have defined the Floquet representation of the Hamiltonian $\hat{\mathscr{H}}$ and u_α as

$$\hat{\mathscr{H}}_{mn} = \mathscr{H}_{m-n} = \int_0^T \frac{dt}{T}\mathscr{H}(t)e^{i(m-n)\Omega t}, \tag{3.7}$$

$$u_{\alpha,n} = \int_0^T \frac{dt}{T}u_\alpha(t)e^{in\Omega t}. \tag{3.8}$$

Now we obtained the Floquet theorem: *all the solutions of the time-dependent Hamiltonian have the form $\psi_\alpha(t)$ in Eq. (3.5), and are obtained by solving the matrix eigenvalue problem Eq. (3.6).*

The quasienergy, the eigenvalue of Eq. (3.6), has a redundancy: if ϵ^0_α and $\{u^0_{\alpha,n}\}$ are a solution for Eq. (3.6), then $\epsilon^0_\alpha + m\Omega$ and $\{u^0_{\alpha,n+m}\}$ ($m \in \mathbb{Z}$) are trivial solutions for Eq. (3.6). Although they are apparently different, they are all physically equivalent in a sense that they give the same Floquet state $\psi_\alpha(t)$ in Eq. (3.5). In order to avoid these trivial solutions, we impose a condition $\epsilon_\alpha \in [-\Omega/2, \Omega/2)$ for quasienergies.

3.2 Floquet-Green's functions and its relation to Floquet states

It is important to note the relation between the Floquet states and the retarded and advanced Green's functions in periodically driven systems. Recall the differential equation for $G^R(t,t')$ and $G^A(t,t')$ in an explicit form:

$$[i\partial_t - H(t)]G^{R,A}(t,t') = \delta(t-t' \mp 0^+), \tag{3.9}$$

from which $G^{R,A}(t,t')$ are uniquely determined. Since the kernel $i\partial_t - \mathscr{H}(t)$ and the source term $\delta(t-t'\mp 0^+)$ remain unchanged for a time translation $(t,t') \to (t+T,t'+T)$, the retarded and advanced Green's functions should satisfy

$$G^{R,A}(t+T,t'+T) = G^{R,A}(t,t'). \tag{3.10}$$

Note that the Keldysh component does not have the symmetry in general. Due to the translation symmetry in time axis, we can take the discrete Fourier transformation with respect to $t_{\rm av} = (t+t')/2$ for the Green's functions. In order to transform the time variables to $t_{\rm av}$ and $t_{\rm rel} = t - t'$, we introduce a Wigner representation,

$$\bar{G}_n(\omega) = \int_{-\infty}^{\infty} dt_{\rm rel} \int_0^T \frac{dt_{\rm av}}{T} G\left(t_{\rm av} + \frac{t_{\rm rel}}{2}, t_{\rm av} - \frac{t_{\rm rel}}{2}\right) e^{in\Omega t_{\rm av}} e^{i\omega t_{\rm rel}}. \tag{3.11}$$

The Wigner representation has a physical meaning: $\bar{G}(t_{\rm av},\omega)$ is the amplitude of the ω-oscillating mode at time $t_{\rm av}$, which is T-periodic in $t_{\rm av}$. In particular, $\bar{G}_{n=0}(\omega)$ is the amplitude of ω-oscillating mode averaged over the period $t_{\rm av} \in [0,T]$.

For convenience, we also introduce a Floquet representation, defined by

$$\hat{G}_{mn}(\omega) = \bar{G}_{m-n}\left(\omega + \frac{m+n}{2}\Omega\right). \tag{3.12}$$

The advantage of the Floquet representation is that the convolution of the form $A(t,t') = \int B(t,\bar{t})C(\bar{t},t')d\bar{t}$ is transformed as $A_{mn}(\omega) = \sum_l B_{ml}C_{ln}$. Using this property, we can transform the differential equation Eq. (3.9) as

$$\sum_l [(\omega + m\Omega)\delta_{ml} - \hat{H}_{ml}]\hat{G}^{R,A}_{ln} = \delta_{mn}. \tag{3.13}$$

Recalling the eigenvalue problem for the Floquet states Eq. (3.5), we notice that $m\Omega\delta_{ml} - \hat{H}_{ml}$ is diagonalized by the Floquet states $u_\alpha = \{u_{\alpha,n}\}$. Therefore we can explicitly diagonalize the retarded and advanced Green's functions as

$$\hat{\Lambda}^{-1}\hat{G}^{R,A}\hat{\Lambda} = \mathrm{diag}\left\{\frac{1}{\omega - \epsilon_\alpha \pm i0^+}\right\}_{\alpha\in\mathbb{N}}, \tag{3.14}$$

where $\hat{\Lambda} = (\cdots, u_{\alpha_1}, u_{\alpha_2}, \cdots)$ is a unitary matrix.

3.3 Structure of spectral functions for Floquet states

Having related the retarded Green's function and Floquet states, we present a typical structure of the Green's function for periodically driven systems. Due to the redundancy of quasienergies, the Green's functions $\bar{G}_0^{R,A}(\omega)$ turn out to have characteristic structures in ω-axis, with spacing Ω.

In fact, the Floquet-Green's functions in Eq. (3.13) are explicitly written down for one-band systems [68] as

$$\hat{G}_{mn}^{R,A}(\omega) = \sum_l \frac{\Lambda_{ml}\Lambda_{ln}}{\omega + l\Omega - \hat{H}_{00} \pm i0^+}, \tag{3.15}$$

and thus the time-averaged Green's function $\bar{G}_0^R(\omega)$, connected to the Floquet-Green's function by Eq. (3.12), turns out to have poles $\omega = \hat{H}_{00} - n\Omega$ ($n = 0, \pm 1, \pm 2, \cdots$). The presence of poles of the retarded Green's function implies some absorptions and emission processes exist. In fact, the residues at $\omega = \hat{H}_{00} \pm n\Omega$ ($n = 1, 2, \cdots$) correspond to a n-photon absorption or emission process, and give rise to a ladder structure for the spectral function $A(\omega) = -(1/\pi)\mathrm{Im}\bar{G}_0^R(\omega)$, known as the *Wannier-Stark ladder* [69, 70]. In particular, in lattice systems, electrons form a band structure and the the original band splits to sidebands with energy spacing Ω, the so called Floquet sidebands [68]. Optical properties of electronic systems are described by the spectral function and thus the Floquet sidebands can be observed in various electronic systems subject to external ac-fields.

3.4 DMFT formalism in terms of Floquet-Green's functions

We have introduced the Floquet representation of time-dependent Green's functions. We have also clarified its relation to the Floquet states and eigenvalues in Eq. (3.14). Next we would like to deal with the DMFT self-consistency equations with the Floquet-Green's functions.

As we have shown, G^R and G^A have the time-translational symmetry $(t, t') \to (t+T, t'+T)$ but G^K does not in general. However, for steady states in periodically driven systems, we can show that G^K indeed has the time-translational symmetry. In order to show that, let us recall the DMFT self-consistency equations that we have established in Chapter 2,

$$\underline{G}_{\boldsymbol{k}}^{-1}(t,t') = \underline{G}_{0\boldsymbol{k}}^{-1}(t,t') - \underline{\Sigma}_{\mathrm{diss}}(t,t') - \underline{\Sigma}(t,t'), \tag{3.16a}$$

$$\underline{G}_{\mathrm{loc}}(t,t') = \sum_{\boldsymbol{k}} \underline{G}_{\boldsymbol{k}}(t,t'), \tag{3.16b}$$

$$\underline{\mathscr{G}}^{-1}(t,t') = \underline{G}_{\mathrm{loc}}^{-1}(t,t') + \underline{\Sigma}(t,t'), \tag{3.16c}$$

$$\underline{\Sigma}(t,t') = \underline{\Sigma}_{\mathrm{DMFT}}[\underline{\mathscr{G}}](t,t'). \tag{3.16d}$$

We can regard Eqs.(3.16) as deterministic equations for $\underline{\Sigma}(t,t')$, with a kernel $\underline{G}_{0\boldsymbol{k}}^{-1}(t,t')$ and a source term $\underline{\Sigma}_{\mathrm{diss}}(t,t')$. We have discarded the Keldysh component $G_{0\boldsymbol{k}}^K(t,t')$ of the noninteracting Green's function, assuming that the distribution function in the initial state is irrelevant to the steady state. Due to this assumption, the noninteracting Green's function $G_{0\boldsymbol{k}}(t,t')$ consists of the retarded and advanced components only, and therefore has the time-translational symmetry. As we have discussed in Sec.2.1.5, the heat-bath is assumed

to be in equilibrium and thus the source term of the equation, $\underline{\Sigma}_{\rm diss}(t,t')$, also has the time-translational symmetry. This observation suggests that, if there exists a unique solution $\underline{\Sigma}(t,t')$ of Eqs.(3.16), we have another solution $\underline{\Sigma}(t+T,t'+T)$ and the two should coincide with each other due to the assumption. Therefore the solution of Eq. (3.16) should have the time-translational symmetry. We have just assumed that the solution of Eqs.(3.16) is unique. However, within our experience, the numerical calculations show that the solution is uniquely determined without any numerical instability in almost every case, supporting the uniqueness of the solution.

Having proved that the unique solution of Eqs.(3.16) has the time-translational symmetry, we can take the Floquet representation of Eqs.(3.16) by taking the Fourier transformation with respect to $t_{\rm av} = (t+t')/2$ and $t_{\rm rel} = t - t'$. We finally obtain the Floquet representation of the DMFT self-consistency equations,

$$\hat{\underline{G}}_{\boldsymbol{k}}^{-1}(\omega)_{mn} = \hat{\underline{G}}_{0\boldsymbol{k}}^{-1}(\omega)_{mn} - \hat{\underline{\Sigma}}_{\rm diss}(\omega)_{mn} - \hat{\underline{\Sigma}}(\omega)_{mn}, \tag{3.17a}$$

$$\hat{\underline{G}}_{\rm loc}(\omega)_{mn} = \sum_{\boldsymbol{k}} \hat{\underline{G}}_{\boldsymbol{k}}(\omega)_{mn}, \tag{3.17b}$$

$$\hat{\underline{\mathscr{G}}}^{-1}(\omega)_{mn} = \hat{\underline{G}}_{\rm loc}^{-1}(\omega)_{mn} + \hat{\underline{\Sigma}}(\omega)_{mn}, \tag{3.17c}$$

$$\hat{\underline{\Sigma}}(\omega)_{mn} = \hat{\underline{\Sigma}}_{\rm DMFT}[\underline{\mathscr{G}}](\omega)_{mn}. \tag{3.17d}$$

3.5 Optical conductivity in multiband electron systems

In this section, we give the formula for the optical conductivity in ac-driven steady states in terms of Floquet-Green's functions. In the preceding studies [68, 35], the formula for optical conductivities for ac-driven single-band fermion systems is presented. Here we extend the formula for multi-band system, and present the formula in terms of Floquet-Green' functions. Based on the Floquet-Green's function formula, we further clarify the relation between the Hall conductivity and photo-induced Berry curvature that characterizes the topology of the ac-driven mult-band systems [29].

3.5.1 Formula for optical conductivity in periodically driven systems

Let us recall the formula for the optical conductivity Eq. (2.77) in nonequilibrium. For convenience, we divide the optical conductivity into two parts as

$$\sigma^{ij}(t,t') = \sigma^{ij}_{\rm dia}(t,t') + \sigma^{ij}_{\rm pm}(t,t'), \tag{3.18}$$

with the so-called *diamagnetic conductivity* $\sigma^{ij}_{\rm dia}(t,t')$ and the *paramagnetic conductivity* $\sigma^{ij}_{\rm pm}(t,t')$ [67],

$$\sigma^{ij}_{\rm dia}(t,t') = \frac{1}{\omega}\delta(t-t')\frac{1}{\Omega_{\rm vol}}{\rm tr}\sum_{\boldsymbol{k}}\mu^{ij}_{\boldsymbol{k}}(t)G^{<}_{\boldsymbol{k}}(t,t'),, \tag{3.19a}$$

$$\sigma^{ij}_{\rm pm}(t,t') = \frac{1}{\omega}\frac{1}{\Omega_{\rm vol}}{\rm tr}\sum_{\boldsymbol{k}}\left[v^{i}_{\boldsymbol{k}}(t)G^{R}_{\boldsymbol{k}}(t,t')v^{j}_{\boldsymbol{k}}(t')G^{<}_{\boldsymbol{k}}(t',t)+v^{i}_{\boldsymbol{k}}(t)G^{<}_{\boldsymbol{k}}(t,t')v^{j}_{\boldsymbol{k}}(t')G^{A}_{\boldsymbol{k}}(t',t)\right]. \tag{3.19b}$$

Note that matrix elements $\mu^{ij}_{\boldsymbol{k}}(t)$ and $v^{i}_{\boldsymbol{k}}(t)$ are T-periodic and their Floquet representations are given as

$$(\hat{\mu}^{ij}_{\boldsymbol{k}})_{mn} = \mu^{ij}_{\boldsymbol{k}\,m-n} = \int_0^T \frac{dt}{T}\mu^{ij}_{\boldsymbol{k}}(t)e^{i(m-n)\Omega t}, \tag{3.20a}$$

$$(\hat{v}^{i}_{\boldsymbol{k}})_{mn} = v^{i}_{\boldsymbol{k}\,m-n} = \int_0^T \frac{dt}{T}v^{i}_{\boldsymbol{k}}(t)e^{i(m-n)\Omega t}. \tag{3.20b}$$

In the following, we derive the formula for the time-averaged optical conductivity,

$$\bar{\sigma}(\omega) = {\rm Re}\int_{-\infty}^{\infty}dt_{\rm rel}\int_0^T\frac{dt_{\rm av}}{T}\sigma\left(t_{\rm av}+\frac{t_{\rm rel}}{2},t_{\rm av}-\frac{t_{\rm rel}}{2}\right)e^{i\omega t_{\rm rel}}, \tag{3.21}$$

which is an important observable of steady states of the ac-driven systems.

We note that the time-averaged value of the product $C(t,t') = A(t,t')B(t',t)$ are expressed as

$$C(\omega) = \int_{-\Omega/2}^{\Omega/2}\frac{d\nu}{2\pi}{\rm tr}\hat{A}(\nu)\hat{B}(\nu-\omega). \tag{3.22}$$

Using this formula, we can rewrite the conductivities in Eq. (3.19a) and Eq. (3.19b) in terms of Floquet-Green's functions.

Diamagnetic conductivity. — $\sigma^{ij}_{\rm dia}(t,t')$ can be regarded as the product of $\delta(t-t')$, whose Floquet representation is δ_{mn}, and $\mu^{ij}_{\boldsymbol{k}}(t)G^{<}_{\boldsymbol{k}}(t,t')$. In general, the product $f(t)G(t,t')$ with

$$f(t+T) = f(t), \quad G(t+T,t'+T) = G(t,t')$$

can be transformed as

$$\begin{aligned}(fG)_n(\omega) &= \int_{-\infty}^{\infty}dt_{\rm rel}\int_0^T\frac{dt_{\rm av}}{T}f\left(t_{\rm av}+\frac{t_{\rm rel}}{2}\right)G(t_{\rm av},t_{\rm rel})\cdot e^{i\omega t_{\rm rel}}e^{in\Omega t_{\rm av}}\\ &= \sum_{l=-\infty}^{\infty}\int_{-\infty}^{\infty}dt_{\rm rel}\int_0^T\frac{dt_{\rm av}}{T}f_{-l}G(t_{\rm av},t_{\rm rel})\cdot e^{i(\omega+l\Omega/2)t_{\rm rel}}e^{i(n+l)\Omega t_{\rm av}}.\end{aligned}$$

Substituting $n\to n-m, \omega\to\omega+(m+n)\Omega/2$ and $l\to l-m$, we obtain

$$\widehat{(fG)}_{mn}(\omega) = \sum_l \hat{f}_{ml}\hat{G}_{ln}(\omega) = (\hat{f}\hat{G}(\omega))_{mn}. \tag{3.23}$$

Using Eq. (3.22) and Eq. (3.23), we obtain the Floquet representation for the time-averaged

optical conductivity $\bar{\sigma}^{ij}_{\mathrm{dia}}(\omega)$ as

$$\bar{\sigma}^{ij}_{\mathrm{dia}}(\omega) = \frac{1}{\omega}\frac{1}{\Omega_{\mathrm{vol}}}\mathrm{tr}\sum_{\boldsymbol{k}}\int_{-\Omega/2}^{\Omega/2}\frac{d\nu}{2\pi}\hat{\mu}^{ij}_{\boldsymbol{k}}\hat{G}^{<}_{\boldsymbol{k}}(\nu). \tag{3.24}$$

Actually, $\sigma^{ij}_{\mathrm{dia}}$ always gives a pure imaginary value (that is why we have divided the conductivity into two parts). In fact, the matrix $\hat{\mu}^{ij}_{\boldsymbol{k}}$ is Hermitian with

$$(\hat{\mu}^{ij}_{\boldsymbol{k}})^{\dagger} = \frac{\partial^2\hat{H}^{\dagger}_{0\boldsymbol{k}}}{\partial k_i\partial k_j} = \frac{\partial^2\hat{H}_{0\boldsymbol{k}}}{\partial k_i\partial k_j} = \hat{\mu}^{ij}_{\boldsymbol{k}},$$

and $\hat{G}^{<}_{\boldsymbol{k}}(\omega)$ is anti-Hermitian, since $G^{<}(t,t')^* = -G^{<}(t',t)$ holds from the definition Eq. (2.20a). Thus Eq. (3.24) always gives a pure imaginary value, and we may neglect the diamagnetic conductivity if we are interested in the real part of optical conductivity.

Paramagnetic conductivity. — $\sigma^{ij}_{\mathrm{pm}}(t,t')$ can be regarded as the product of $v^i_{\boldsymbol{k}}(t)G^{\mathrm{R}}(t,t')$ and $v^j_{\boldsymbol{k}}(t)G^{<}_{\boldsymbol{k}}(t,t')$, whose Floquet representations are, from Eq. (3.23), $\hat{v}^i_{\boldsymbol{k}}\hat{G}^{\mathrm{R}}_{\boldsymbol{k}}(\omega)$ and $\hat{v}^j_{\boldsymbol{k}}\hat{G}^{<}_{\boldsymbol{k}}(\omega)$, respectively. Applying Eq. (3.22), we obtain

$$\bar{\sigma}^{ij}_{\mathrm{pm}}(\omega) = \frac{1}{\omega}\frac{1}{\Omega_{\mathrm{vol}}}\mathrm{tr}\sum_{\boldsymbol{k}}\int_{-\Omega/2}^{\Omega/2}\frac{d\nu}{2\pi}\left[\hat{v}^i_{\boldsymbol{k}}\hat{G}^{\mathrm{R}}_{\boldsymbol{k}}(\nu)\hat{v}^j_{\boldsymbol{k}}\hat{G}^{<}_{\boldsymbol{k}}(\nu-\omega) + \hat{v}^i_{\boldsymbol{k}}\hat{G}^{<}_{\boldsymbol{k}}(\nu)\hat{v}^j_{\boldsymbol{k}}\hat{G}^{\mathrm{A}}_{\boldsymbol{k}}(\nu-\omega)\right]. \tag{3.25}$$

Finally, we obtain the Floquet representation for the optical conductivity,

$$\sigma(\omega)^{ij} = \mathrm{Re}\,\frac{1}{\omega}\frac{1}{\Omega_{\mathrm{vol}}}\mathrm{tr}\sum_{\boldsymbol{k}}\int_{-\Omega/2}^{\Omega/2}\frac{d\nu}{2\pi}\left[\hat{v}^i_{\boldsymbol{k}}\hat{G}^{\mathrm{R}}_{\boldsymbol{k}}(\nu+\omega)\hat{v}^j_{\boldsymbol{k}}\hat{G}^{<}_{\boldsymbol{k}}(\nu) + \hat{v}^i_{\boldsymbol{k}}\hat{G}^{<}_{\boldsymbol{k}}(\nu)\hat{v}^j_{\boldsymbol{k}}\hat{G}^{\mathrm{A}}_{\boldsymbol{k}}(\nu-\omega)\right]. \tag{3.26}$$

3.5.2 Hall conductivity and Berry curvature in nonequilibrium

The static Hall conductivity $\sigma^{xy}(\omega=0)$ is a quantity of particular importance. The relation between the Hall conductivity and the topological aspects of the system is first recognized in the integer quantum Hall effect, where the Hall conductivity is quantized as

$$\sigma^{xy}(0) = \frac{e^2}{h}\nu, \quad \nu\in\mathbb{N}, \tag{3.27}$$

and the integer ν is a topological invariant, given by the integral of the Berry curvature $\mathscr{B}_{m\boldsymbol{k}}$ of the mth band over the whole Brillouin zone,

$$\nu = \sum_m\int_{\mathrm{BZ}}\frac{d\boldsymbol{k}^2}{2\pi}\mathscr{B}_{m\boldsymbol{k}}f_{\mathrm{FD}}(\epsilon_{m\boldsymbol{k}}), \tag{3.28}$$

$$\mathscr{B}_{m\boldsymbol{k}} = -i\nabla_{\boldsymbol{k}}\times\left[\langle u_{m\boldsymbol{k}}|\nabla_{\boldsymbol{k}}|u_{m\boldsymbol{k}}\rangle\right]_z \tag{3.29}$$

with the mth Bloch wave function $|u_{m\boldsymbol{k}}\rangle$, the energy $\epsilon_{m\boldsymbol{k}}$, and the Fermi-Dirac distribution function $f(\omega)$. This is the well-known Thouless-Kohmoto-Nightingale-Nijs (TKNN) formula

[18], which is applicable to general multi-band systems in equilibrium.

In a similar way, one can define a curvature and a topological invariant in ac-driven systems in terms of Floquet states [29, 34]. Therefore, the Hall conductivity in ac-driven systems can also be regarded as the *indicator of photo-induced topological phase transitions*. In the following, restricting ourselves to noninteracting cases, we obtain a Floquet topological invariant starting from the Kubo formula, and obtain the clear relation with the expression in the extended TKNN formula in ac-diven systems, which was first discussed by Oka, *et al.* [29].

dc-Hall conductivity in ac-driven systems

Here we recall Eq. (3.26) and rewrite it for $(i,j)=(x,y)$ and in the limit $\omega\to 0^+$. The integrand of Eq. (3.26) can be rewritten as

$$\begin{aligned}
&\mathrm{Re}\,\mathrm{tr}\,\frac{1}{\omega}\left[\hat{v}^x_{\boldsymbol{k}}\hat{G}^{\mathrm{R}}_{\boldsymbol{k}}(\nu+\omega)\hat{v}^y_{\boldsymbol{k}}\hat{G}^{<}_{\boldsymbol{k}}(\nu)+\hat{v}^x_{\boldsymbol{k}}\hat{G}^{<}_{\boldsymbol{k}}(\nu)\hat{v}^y_{\boldsymbol{k}}\hat{G}^{\mathrm{A}}_{\boldsymbol{k}}(\nu-\omega)\right]\\
&=\mathrm{tr}\,\frac{1}{2\omega}\left\{\left[\hat{v}^x_{\boldsymbol{k}}\hat{G}^{\mathrm{R}}_{\boldsymbol{k}}(\nu+\omega)\hat{v}^y_{\boldsymbol{k}}\hat{G}^{<}_{\boldsymbol{k}}(\nu)+\hat{v}^x_{\boldsymbol{k}}\hat{G}^{<}_{\boldsymbol{k}}(\nu)\hat{v}^y_{\boldsymbol{k}}\hat{G}^{\mathrm{A}}_{\boldsymbol{k}}(\nu-\omega)\right]+\mathrm{h.c.}\right\}\\
&=\mathrm{tr}\,\frac{1}{2\omega}\left\{\left[\hat{v}^x_{\boldsymbol{k}}\hat{G}^{\mathrm{R}}_{\boldsymbol{k}}(\nu+\omega)\hat{v}^y_{\boldsymbol{k}}\hat{G}^{<}_{\boldsymbol{k}}(\nu)+\hat{v}^x_{\boldsymbol{k}}\hat{G}^{<}_{\boldsymbol{k}}(\nu)\hat{v}^y_{\boldsymbol{k}}\hat{G}^{\mathrm{A}}_{\boldsymbol{k}}(\nu-\omega)\right]\right.\\
&\qquad\left.+\left[-\hat{v}^x_{\boldsymbol{k}}\hat{G}^{<}_{\boldsymbol{k}}(\nu)\hat{v}^y_{\boldsymbol{k}}\hat{G}^{\mathrm{A}}_{\boldsymbol{k}}(\nu+\omega)-\hat{v}^y_{\boldsymbol{k}}\hat{G}^{\mathrm{R}}_{\boldsymbol{k}}(\nu-\omega)\hat{v}^y_{\boldsymbol{k}}\hat{G}^{<}_{\boldsymbol{k}}(\nu)\right]\right\},
\end{aligned}$$

where in the last transformation we have used $[\hat{G}^{<}(\omega)]^\dagger=-\hat{G}^{<}(\omega)$ and $[\hat{G}^{R}(\omega)]^\dagger=\hat{G}^{A}(\omega)$. We can further transform the above as

$$\begin{aligned}
&=\mathrm{tr}\left[\hat{v}^x_{\boldsymbol{k}}\frac{\hat{G}^{\mathrm{R}}_{\boldsymbol{k}}(\nu+\omega)-\hat{G}^{\mathrm{R}}_{\boldsymbol{k}}(\nu-\omega)}{2\omega}\hat{v}^y_{\boldsymbol{k}}\hat{G}^{<}_{\boldsymbol{k}}(\nu)-\hat{v}^x_{\boldsymbol{k}}\hat{G}^{<}_{\boldsymbol{k}}(\nu)\hat{v}^y_{\boldsymbol{k}}\frac{\hat{G}^{\mathrm{A}}_{\boldsymbol{k}}(\nu+\omega)-\hat{G}^{\mathrm{A}}_{\boldsymbol{k}}(\nu-\omega)}{2\omega}\right]\\
&\xrightarrow{\omega\to 0}\mathrm{tr}\left[\hat{v}^x_{\boldsymbol{k}}\frac{\partial\hat{G}^{\mathrm{R}}_{\boldsymbol{k}}(\nu)}{\partial\nu}\hat{v}^y_{\boldsymbol{k}}\hat{G}^{<}_{\boldsymbol{k}}(\nu)-\hat{v}^x_{\boldsymbol{k}}\hat{G}^{<}_{\boldsymbol{k}}(\nu)\hat{v}^y_{\boldsymbol{k}}\frac{\partial\hat{G}^{\mathrm{A}}_{\boldsymbol{k}}(\nu)}{\partial\nu}\right].
\end{aligned}\tag{3.30}$$

Next, we would like to express the integrand Eq. (3.30) in terms of the Floquet states and quasi-energies. As we have shown in Sec.3.2, the retarded and advanced Green's functions are diagonalized by taking the Floquet eigenstates $\hat{\Lambda}_{\boldsymbol{k}}=(u_{1\boldsymbol{k}},u_{2\boldsymbol{k}},\cdots)$ as a basis as

$$\hat{\Lambda}^{-1}_{\boldsymbol{k}}\hat{G}^{R,A}_{\boldsymbol{k}}(\omega)\hat{\Lambda}_{\boldsymbol{k}}=\mathrm{diag}\left\{\frac{1}{\omega-\epsilon_{\alpha\boldsymbol{k}}\pm i0^+}\right\}_{\alpha\in\mathbb{Z}},\tag{3.31}$$

where $\epsilon_{\alpha\boldsymbol{k}}$ is the quasi-energy of the αth Floquet state.

Now, we introduce the distribution function $f_{\alpha\boldsymbol{k}}$ for the Floquet states in terms of the lesser Green's function. Recall the nonequilibrium distribution kernel $\hat{F}$ is given by

$$\hat{G}^{K}_{\boldsymbol{k}}(\omega)=\hat{G}^{R}_{\boldsymbol{k}}(\omega)\hat{F}_{\boldsymbol{k}}(\omega)-\hat{F}_{\boldsymbol{k}}(\omega)\hat{G}^{A}_{\boldsymbol{k}}(\omega),\tag{3.32}$$

and $\hat{F}(\omega)$ is related to the nonequilibrium distribution function as $\hat{f}_{\boldsymbol{k}}(\omega)=[\hat{1}-\hat{F}_{\boldsymbol{k}}(\omega)]/2$.

In equilibrium, $F_{\boldsymbol{k}}(t,t')$ is independent of $t_{\mathrm{av}}=(t+t')/2$ and therefore $\hat{F}(\omega)$ is a diagonal

matrix. In that case, $\hat{G}^{<}_{\boldsymbol{k}}(\omega)$ is also diagonalized by $\hat{\Lambda}_{\boldsymbol{k}}$ as

$$\hat{\Lambda}^{-1}_{\boldsymbol{k}}\hat{G}^{<}_{\boldsymbol{k}}(\omega)\hat{\Lambda}_{\boldsymbol{k}} = \mathrm{diag}\{2\pi i\delta(\omega-\epsilon_{\alpha\boldsymbol{k}})f_{\mathrm{FD}}(\omega-\epsilon_{\alpha\boldsymbol{k}})\}_{\alpha\in\mathbb{Z}}, \tag{3.33}$$

with the Fermi-Dirac distribution $f_{\mathrm{FD}}(\omega) = (1+e^{\omega/T})^{-1}$. The diagonal elements can be regarded as the $\boldsymbol{k}$-resolved density of states at ω, $2\pi\delta(\omega-\epsilon_{\alpha\boldsymbol{k}})$, multiplied by the distribution function $f_{\mathrm{FD}}(\omega-\epsilon_{\alpha\boldsymbol{k}})$.

With the physical interpretation, we can naturally extend this to nonequilibrium steady states as

$$\hat{\Lambda}^{-1}_{\boldsymbol{k}}\hat{G}^{<}_{\boldsymbol{k}}(\omega)\hat{\Lambda}_{\boldsymbol{k}} = \mathrm{diag}\{2\pi i\delta(\omega-\epsilon_{\alpha\boldsymbol{k}})f_{\alpha\boldsymbol{k}}\}_{\alpha\in\mathbb{Z}}, \tag{3.34}$$

with the distribution function $f_{\alpha\boldsymbol{k}}$ for the Floquet state $\psi_{\alpha\boldsymbol{k}}$. Here we implicitly assumed that the diagonal elements of $\hat{\Lambda}^{-1}_{\boldsymbol{k}}\hat{G}^{<}_{\boldsymbol{k}}(\omega)\hat{\Lambda}_{\boldsymbol{k}}$ are completely absorbed in $f_{\alpha\boldsymbol{k}}$. With this assumption, $\hat{G}^{R,A,<}_{\boldsymbol{k}}(\omega)$ are diagonalized by the Floquet states as in Eq. (3.31) and Eq. (3.34), and thus we can express the integrand Eq. (3.30) in terms of Floquet states with the unitary transformation $\hat{\Lambda}_{\boldsymbol{k}}$ as

$$\begin{aligned}
&\mathrm{tr}\left[\hat{v}^x_{\boldsymbol{k}}\frac{\partial\hat{G}^{\mathrm{R}}_{\boldsymbol{k}}(\nu)}{\partial\nu}\hat{v}^y_{\boldsymbol{k}}\hat{G}^{<}_{\boldsymbol{k}}(\nu) - \hat{v}^x_{\boldsymbol{k}}\hat{G}^{<}_{\boldsymbol{k}}(\nu)\hat{v}^y_{\boldsymbol{k}}\frac{\partial\hat{G}^{\mathrm{A}}_{\boldsymbol{k}}(\nu)}{\partial\nu}\right] \\
&\quad= \sum_{\alpha,\beta\in\mathbb{Z}}\Big[\hat{w}^x_{\alpha\beta,\boldsymbol{k}}\frac{-1}{(\nu-\epsilon_{\beta\boldsymbol{k}}+i0^+)^2}\hat{w}^y_{\beta\alpha,\boldsymbol{k}}\cdot 2\pi i\delta(\nu-\epsilon_{\alpha\boldsymbol{k}})f_{\alpha\boldsymbol{k}} \\
&\qquad\quad - \hat{w}^x_{\beta\alpha,\boldsymbol{k}}\cdot 2\pi i\delta(\nu-\epsilon_{\alpha\boldsymbol{k}})f_{\alpha\boldsymbol{k}}\cdot\hat{w}^y_{\alpha\beta\boldsymbol{k}}\frac{-1}{(\nu-\epsilon_{\beta\boldsymbol{k}}-i0^+)^2}\Big] \\
&\quad= -i\sum_{\alpha\neq\beta}\frac{\hat{w}^x_{\alpha\beta}\hat{w}^y_{\beta\alpha}-\hat{w}^y_{\alpha\beta}\hat{w}^x_{\beta\alpha}}{(\epsilon_{\alpha\boldsymbol{k}}-\epsilon_{\beta\boldsymbol{k}})^2}\cdot 2\pi\delta(\nu-\epsilon_{\alpha\boldsymbol{k}})f_{\alpha\boldsymbol{k}},
\end{aligned} \tag{3.35}$$

where we have defined the transformed current matrix $\hat{w}_{\boldsymbol{k}}$,

$$\hat{w}^i_{\boldsymbol{k}} = \hat{\Lambda}^{-1}_{\boldsymbol{k}}\hat{v}_{\boldsymbol{k}}\hat{\Lambda}_{\boldsymbol{k}}, \quad i=x,y. \tag{3.36}$$

Plugging this into Eq. (3.26), we obtain the dc-Hall conductivity formula for noninteracting systems in intense ac-fields as

$$\sigma_{xy}(0) = \frac{1}{\Omega_{\mathrm{vol}}}\sum_{\boldsymbol{k}}\sum_{\alpha\neq\beta}(-i)\frac{\hat{w}^x_{\alpha\beta}\hat{w}^y_{\beta\alpha}-\hat{w}^y_{\alpha\beta}\hat{w}^x_{\beta\alpha}}{(\epsilon_{\alpha\boldsymbol{k}}-\epsilon_{\beta\boldsymbol{k}})^2}f_{\alpha\boldsymbol{k}}. \tag{3.37}$$

In the following, we discuss the relation between Eq. (3.37) and the Berry curvature defined for the Floquet bands. We introduce a quantity,

$$\mathscr{B}^z_{\alpha\boldsymbol{k}} = \sum_{\beta(\neq\alpha)}(-i)\frac{\hat{w}^x_{\alpha\beta}\hat{w}^y_{\beta\alpha}-\hat{w}^y_{\alpha\beta}\hat{w}^x_{\beta\alpha}}{(\epsilon_{\alpha\boldsymbol{k}}-\epsilon_{\beta\boldsymbol{k}})^2}, \tag{3.38}$$

which is determined solely from the structure of the Floquet Hamiltonian $\hat{H}_{mn,\boldsymbol{k}}$. This quan-

tity, in fact, coincides with the Berry curvature for the Floquet state $|u_{\alpha\boldsymbol{k}}\rangle$,

$$\mathscr{B}^z_{\alpha\boldsymbol{k}} = \big[-i\nabla \times \langle u_{\alpha\boldsymbol{k}}|\nabla|u_{\alpha\boldsymbol{k}}\rangle \big]_z. \tag{3.39}$$

For detailed calculations, see Appendix D. Thus we can conclude that the dc-Hall conductivity calculated from the Kubo formula is the sum of the photo-induced Berry curvature Eq. (3.39) of each Floquet band, muitlplied by the nonequilibrium distribution function $f_{\alpha\boldsymbol{k}}$.

The Berry curvature is determined solely from the structure of the Floquet Hamiltonian $\hat{H}_{\boldsymbol{k}}$, while the distribution $f_{\alpha\boldsymbol{k}}$ is not universal and need to be calculated for each problem. As we shall show in the Chapter 5, not only the Berry curvature, but also the nonequilibrium distribution function play important roles in the observables.

Chapter 4

Nonequilibrium steady states in dp-model in ac-electric fields

In this chapter, we study nonequilibrium steady states of the dp-model in strong external ac-fields, motivated by recent pump-probe measurements for high-T_c cuprates.

Oka and Aoki [36] studied the noninteracting dp-model in circularly polarized light. The electron correlation in the ac-driven dp-model, however, is not studied so far. Our study is the first application of Floquet-DMFT technique for the dp-model in strongly correlated regime.

We investigate electronic structures in the dp-model in strong circularly polarized ac-fields and obtain novel photon-dressed band structures and nonequilibrium distribution functions which indicates a population inversion, which are found to be significantly different from those in equilibrium. Specifically, we have calculated optical conductivities and found negative optical contuctivities in the spectra of optical conductivities in the nonequilibrium situation. We have also discussed how the Zhang-Rice singlet band behave under the influence of external fields.

4.1 Introduction — Why dp-model?

4.1.1 Physics of doped cuprates

The high-T_c cuprates have been studied extensively since Bednorz and Müller discovered superconductivity [71], whose critical temperature $T_c = 35$K. After their first discovery, dozens of copper oxide superconductors are found. Mercury-based copper oxides [72] are among the cuprate families that have the highest transition temperature $T_c = 135$ K, which is far above the critical temperature of conventional superconductors. The series of copper-oxide-based superconductors, *cuprates*, are therefore regarded as the most prospective candidate for room temperature superconductors.

The lattice structure of cuprates are shown in Fig. 4-1(a). Cuprates consist of conducting CuO_2 planes and insulating block layers. Since the atomic copper d-orbital is strongly localized, the Coulomb repulsion on the copper site is quite large, and thus cuprates are categorized as strongly correlated systems.

Undoped cuprates are themselves Mott insulators, and superconductivity manifests itself

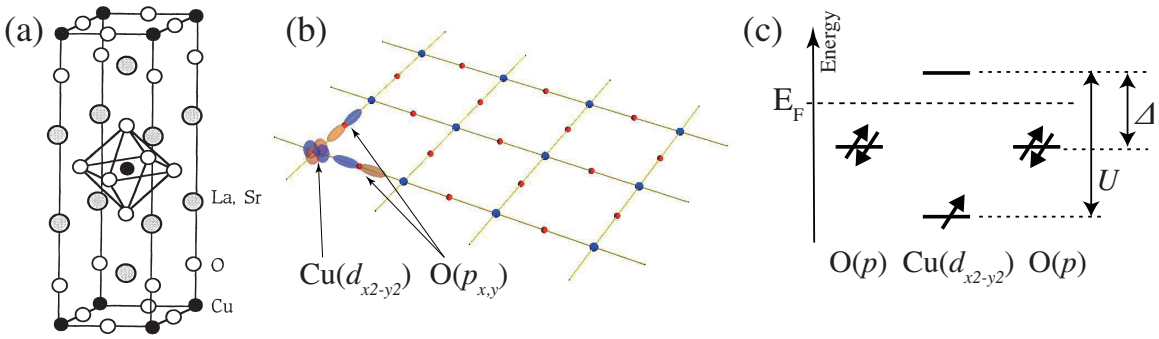

Figure 4-1: (a) Crystal structure of $Nd_{2-x}Ce_xCuO_4$ after Ref. [73] (Copyright (2014) by the American Physical Society). (b) CuO_2 plane in cuprates. $d_{x^2-y^2}$-orbital in a copper atom and p-orbitals in oxygen atoms are shown. (c) Energy scheme of atomic orbitals of copper and oxygen atoms in CuO_2 plane. U is the Coulomb repulsion energy at copper sites, and Δ is the energy required when an electron hops from a copper site to an adjacent oxygen site (charge-transfer energy).

only when electrons or holes are doped in the system, by means of replacing elements, applying pressures and so on. In Fig. 4-1(c), we show the energy scheme of atomic orbitals in CuO_2 plane. Due to the strong electron repulsion on d-orbitals, a doubly occupied d-orbital has a large energy U. Thus electrons tend to avoid each other on each copper site, and copper sites are half-filled in undoped case. On the other hand, the electron correlation on p-orbitals (Fig. 4-1(b)) at oxygen sites is negligibly small compared to U. The Fermi level E_F of undoped cuprates resides between the energy levels of p-orbitals and doubly occupied d-orbitals (see Fig. 4-1(c)). In this case, the lowest electronic excitation takes place between an electronic state at oxygen sites and a hole state at cooper sites. We define the level offset of d- and p-orbitals as Δ, which corresponds to the excitation energy required for electron transfer from an oxygen site to a copper site. As we have stated, cuprates satisfy $U > \Delta$ and the lowest excitation is inter-site (copper to oxygen) transitions. Thus cuprates are called a *charge-transfer insulator*.

In Fig. 4-2(a), we show the global phase diagram of carrier doped cuprates. Near the undoped regime, the system is insulating, with antiferromagnetic long range order, due to the super-exchange interaction between the neighboring copper sites. Further doping into the insulating phase gives rise to the superconductivity with the d-wave pairing order parameter.

Here, let us briefly mention how to treat cuprates theoretically. In order to understand the physics of cuprates, it is important to construct an effective model that contains essential physics of the system. Such an effective lattice model for cuprates can be constructed by focusing on CuO_2 layers and discard other insulating block layers. A CuO_2 plane, shown in Fig. 4-1(b), consists of three atoms per unit cell: one copper site and two oxygen sites. As we have stated, the strong electron repulsion on copper sites is important to describe the energy scheme of a CuO_2 plane. Thus we introduce the Hubbard interaction U on copper sites and neglect long-range Coulomb interactions as a minimal model. This three-band model is called the dp-model, first proposed by Emery [8]. The Hamiltonian of the dp-model

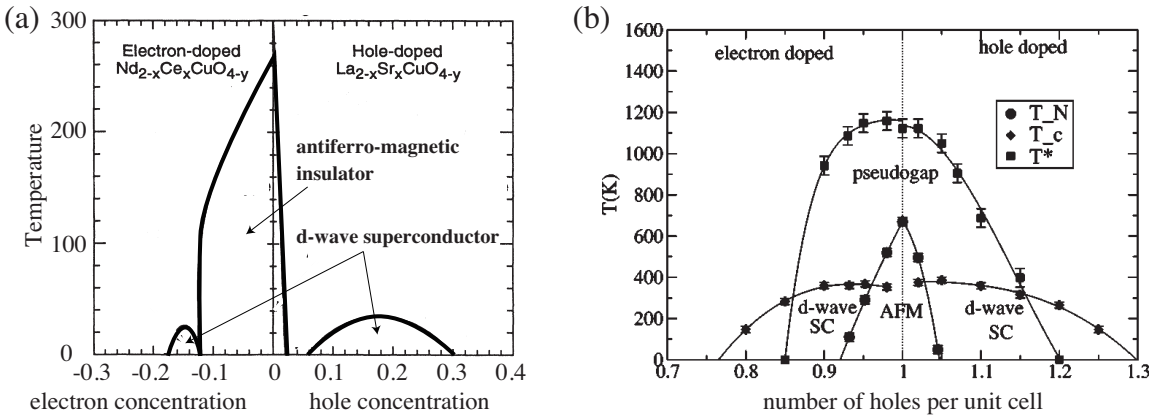

Figure 4-2: (a) Schematic phase diagram of high-T_c cuprates, after Ref. [73] (Copyright (2014) by the American Physical Society). The horizontal and vertical axes represent hole concentration x and temperature T, respectively. (b) A numerical phase diagram of the dp-model with dynamical cluster approximation [74] (Copyright (2014) by the American Physical Society). The horizontal and vertical axes are number of holes per unit cell and temperature, respectively. SC and AFM represent superconducting and antiferromagnetic phase, respectively.

is given in the next section, in Eq. (4.1). In Fig. 4-2(b) we show a phase diagram of the dp-model obtained by dynamical cluster approximation by Macridin, *et al.* [74]. Similarly to the experimental phase diagram (Fig. 4-2(a)), there are d-wave superconducting phases adjacent to the metal-insulator transition boundary in the phase diagram of the dp-model. In Fig. 4-2(b), there is also a "pseudo gap" phase where low-lying excitations have energy gap at higher temperatures than T_c [75], which is also consistent with experiments [76]. Thus the dp-model, although being a simple lattice model for a single CuO_2 layer with minimal Hubbard interactions, contains enough physical processes to understand the rich phase diagram of cuprates.

4.1.2 Optical manipulations of cuprates

Due to the rich phases in the carrier-doped regime, cuprates are also regarded as a fascinating playground for novel photo-induced phase transitions. Carrier injection by optical pumping is one possibility of photo-induced phase transitions in cuprates. Okamoto, *et al.* [24] demonstrated such a photo-carrier doping in cuprates. In Fig. 4-3(a) we show an optical absorption spectra of undoped La_2CuO_4(LCO) by pump-probe measurements. The horizontal axis represents the frequency $\omega_{\rm probe}$ of the probe field, while the vertical axis, the optical absorption ΔOD, is proportional to the optical conductivity. The symbols represent the transient absorption spectra for LCO at $t = 0.3, 2.0$ and 50 ps after pumping. The spectrum for doped LCO is also plotted as a solid curve. One can see the rise of the structure around $\omega_{\rm probe} = 0$, the so-called *Drude peak*, after pumping, indicating that the system has finite dc-longitudinal conductivity. Since the Drude peak survives for ~ 2 ps after the pumping, they concluded that a photo-induced insulator-to-metal transition occurs in their system.

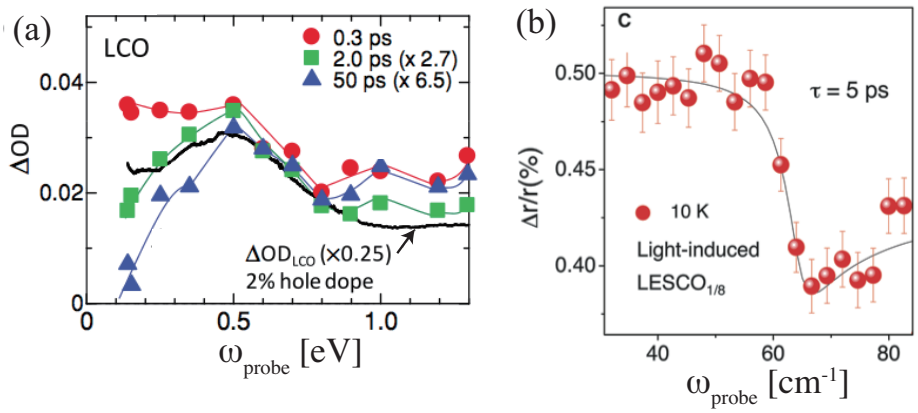

Figure 4-3: (a) Optical absorption spectra (ΔOD) in La_2CuO_4(LCO) with 2.25 eV pump light [24] (Copyright (2014) by the American Physical Society). The solid line is the ΔOD spectrum for 2% hole-doped LCO, while symbols are ΔOD spectra for pumped LCO at $t = 0.3, 2.0$ and 50 ps after pumping. The rise of the transient spectrum near the zero probe frequency $\omega_{\rm probe} = 0$ indicates a metallic response due to the photo-carriers. (b) Optical reflectance in $La_{1.675}Eu_{0.2}Sr_{0.125}CuO_4$($LESCO_{1/8}$) at $T = 10$K, which is in stripe-ordered insulating phase [25], reprinted with kind permission from AAAS. Transient spectra $t = 5$ ps after a mid-infrared pumping are measured and we plot the result normalized by the static spectra. The edge structure at the probe frequency $\omega_{\rm probe} = 60{\rm cm}^{-1}$ is the plasma edge which originates from the Josephson coupling between two superconducting CuO_2 layers.

The photo-induced superconductivity was also reported by Fausti, *et al*. [25] in the stripe-ordered cuprates, $La_{1.675}Eu_{0.2}Sr_{0.125}CuO_4$($LESCO_{1/8}$). They applied a mid-infrared pump light and observed the transient refractivity by pump-probe measurements. They found a plasma-edge response at $\omega_{\rm probe} \simeq 60{\rm cm}^{-1}$, which coincides with the Josephson plasma-edge response of the $LESCO_{1/8}$ in superconducting phase. This suggests an insulator-to-superconductor phase transition by irradiating light.

Since there are dozens of fascinating experiments on the photo-induced phase transitions in cuprates, it is quite interesting to investigate the physical properties of photo-induced cuprates in a theoretical manner. The difficulty in understanding the physics of photo-induced phase transitions is that universal laws in optically driven systems have not been established. The notion of band structures and distribution functions, which works well for the physics in equilibrium, may not be applicable to non-equilibrium situations. Our motivation in this chapter is to clarify how the photo-induced carriers in cuprates differ from chemically doped carriers. To be more specific, we would like to address the following questions.

- *Is a "rigid band picture" valid for photo-doped cuprates?*

  In equilibrium, electron or hole doping are often treated by a "rigid band picture". In this picture, one first calculates electronic states for the undoped case, and simulate electron or hole doping by shifting the chemical potential. This treatment is reasonable when doped carriers do not alter the low-lying electronic structures. In fact, this

simulation gives reasonable results for cuprates, as we have confirmed the comparison between experiments and numerical phase diagram of cuprates in Fig. 4-2.

However, in optical carrier doping, many kinds of excitations, not only low-lying excitations, but also high-energy excitations such as inter-band transitions, are continuously activated while ac-fields are applied. In such a situation, there is no reason why the rigid band picture is justified. We should therefore fully incorporate the external fields and obtain the band structure which may drastically change in ac-driven situations.

- *How do the photo-carriers distribute in the band?* In the above we stressed that the band structure may severely depend on external fields. In nonequilibrium we should also examine how the electrons are distributed in the (deformed) band structure. In equilibrium, the distribution function is universally given by the Fermi-Dirac distribution. However, in nonequilibrium, there are no longer universal functions for distribution. In some cases, the nonequilibrium distribution gives rise to the so called *population inversion* [35], where the population of electrons and holes are partially inverted. There, characteristic features appear in some observables which clearly distinguishes the nonequilibrium states from equilibrium ones. Therefore, we would like to investigate the nonequilibrium distribution and resulting effects for observables in optical measurements, such as optical conductivities.

4.2 Model

In this section we review the basics of the *dp*-model and derive the noninteracting Floquet Green's functions in linearly and circularly polarized fields.

4.2.1 *dp*-model

The *dp*-model consists of the Cu($d_{x^2-y^2}$) orbitals and O(p_x,p_y) orbitals shown in Fig. 4-4. The Hamiltonian for the *dp*-model reads

$$\mathscr{H} = \mathscr{H}_0 + \mathscr{H}_1 + \mathscr{H}_2, \tag{4.1a}$$

$$\mathscr{H}_0 = \sum_{i\sigma} \epsilon_d d^\dagger_{i\sigma} d_{i\sigma} + \sum_{l\sigma} \epsilon_p p^\dagger_{l\sigma} p_{l\sigma}, \tag{4.1b}$$

$$\mathscr{H}_1 = \sum_{i\sigma} \sum_{l\in\Lambda_i} \tau^{dp}_{il} t_{dp} d^\dagger_{i\sigma} p_{l\sigma} + \sum_{\langle ll'\rangle\sigma} \tau^{pp}_{ll'} t_{pp} p^\dagger_l p_{l'} \tag{4.1c}$$

$$\mathscr{H}_2 = \sum_i U_d d^\dagger_{i\uparrow} d_{i\uparrow} d^\dagger_{i\downarrow} d_{i\downarrow} + \sum_l U_p p^\dagger_{i\uparrow} p_{i\uparrow} p^\dagger_{i\downarrow} p_{i\downarrow}, \tag{4.1d}$$

where $\mathscr{H}_0$ represents the d-p level offset, $\mathscr{H}_1$ is the electron-hopping term, and $\mathscr{H}_2$ is the Hubbard interaction term. Due to the parity of the orbitals, the signs of the hopping parameters $\tau^{dp}_{il} = \pm 1$ and $\tau^{pp}_{ll'} = \pm 1$ are determined as in Fig. 4-4, where t_{dp} and t_{pp} are respectively the amplitudes of the corresponding hopping parameters. Taking the Fourier transformation

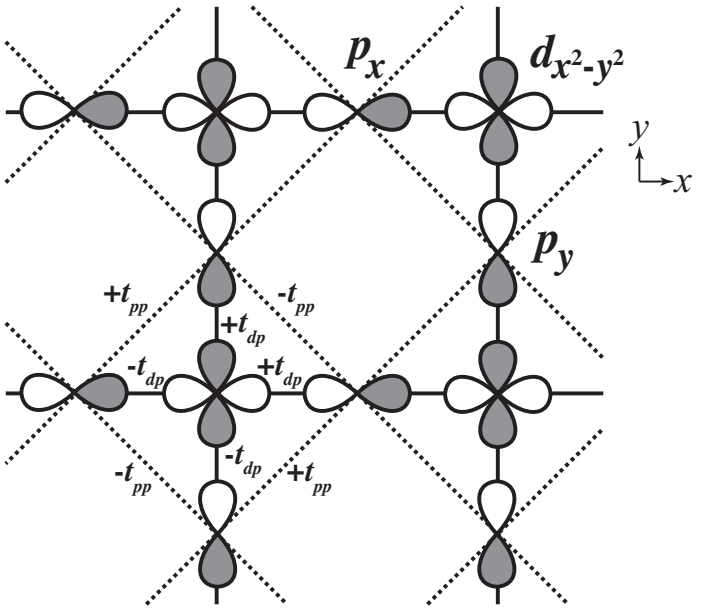

Figure 4-4: Lattice structure of the *dp*-model in real space. The atomic orbitals are schematically shown, where sign of the wave functions are shown by open and shaded regions. Solid and dotted lines represent the hopping paths between Cu-O and O-O hoppings, respectively.

for site indices in Eq. (4.1), we obtain the noninteracting Hamiltonian $\mathscr{H}_0$ in the $\boldsymbol{k}$-space as

$$\mathscr{H}_0 = \sum_{\boldsymbol{k}\sigma} \psi^\dagger_{\boldsymbol{k}\sigma} H_{0\boldsymbol{k}} \psi_{\boldsymbol{k}\sigma}, \tag{4.2a}$$

$$\psi_{\boldsymbol{k}\sigma} = {}^t\left(d_{\boldsymbol{k}\sigma} \quad p_{x,\boldsymbol{k}\sigma} \quad p_{y,\boldsymbol{k}\sigma}\right), \tag{4.2b}$$

$$H_{0\boldsymbol{k}} = \begin{pmatrix} -\mu & -2it_{dp}\sin\frac{k_x}{2} & -2it_{dp}\sin\frac{k_y}{2} \\ 2it_{dp}\sin\frac{k_x}{2} & \Delta-\mu & -4t_{pp}\sin\frac{k_x}{2}\sin\frac{k_y}{2} \\ 2it_{dp}\sin\frac{k_y}{2} & -4t_{pp}\sin\frac{k_x}{2}\sin\frac{k_y}{2} & \Delta-\mu \end{pmatrix}. \tag{4.2c}$$

We take the lattice constant (the distance between nearest Cu sites) to be unity.

4.2.2 *dp*-model in linearly and circularly polarized electric fields

We consider the linearly and circularly polarized electric field $\boldsymbol{E}(t) = -\partial_t \boldsymbol{A}(t)$ given by the vector potential

$$\boldsymbol{A}(t) = \begin{cases} {}^t(A\cos\Omega t, A\cos\Omega t), & \text{linearly polarized,} \\ {}^t(A\cos\Omega t, A\sin\Omega t), & \text{circularly polarized.} \end{cases} \tag{4.3}$$

The external fields are included as the Peierls substitution: $\boldsymbol{k} \to \boldsymbol{k} + \boldsymbol{A}(t)$, and the Floquet matrix elements introduced in Chapter 3 are calculated as

$$\hat{H}_{mn}(\boldsymbol{k}) = H_{0\boldsymbol{k},m-n} = \int_0^T \frac{dt}{T} H_{0,\boldsymbol{k}+\boldsymbol{A}(t)} e^{i(m-n)\Omega t}. \tag{4.4}$$

The Floquet matrices $H_{0\boldsymbol{k},n}$ are 3×3 ones of a form

$$H_{0\boldsymbol{k},n} = \begin{pmatrix} \epsilon_d\delta_{n0} & a^*_{-n} & b^*_{-n} \\ a_n & \epsilon_p\delta_{n0} & c^*_{-n} \\ b_n & c_n & \epsilon_d\delta_{n0} \end{pmatrix}. \tag{4.5}$$

The parameters a_n, b_n and c_n are obtained by calculating Eq. (4.4) with the noninteracting Hamiltonian Eq. (4.2c) and vector potentials Eq. (4.3) for linearly and circularly polarized cases. The detailed calculations are given in Appendix F. The results are the following.

Linearly polarized light—

$$a_n = 2it_{dp}J_n\left(\frac{A}{2}\right)\sin\left(\frac{k_x+n\pi}{2}\right), \tag{4.6a}$$

$$b_n = 2it_{dp}J_n\left(\frac{A}{2}\right)\sin\left(\frac{k_y+n\pi}{2}\right), \tag{4.6b}$$

$$c_n = 2t_{pp}\left[J_n(A)\cos\left(\frac{k_x+k_y+n\pi}{2}\right) - \delta_{n0}\cos\left(\frac{k_x-k_y}{2}\right)\right]. \tag{4.6c}$$

Circularly polarized light—

$$a_n = 2it_{dp}J_n\left(\frac{A}{2}\right)\sin\left(\frac{k_x+n\pi}{2}\right), \tag{4.7a}$$

$$b_n = 2it_{dp}J_n\left(\frac{A}{2}\right)(-i)^n\sin\left(\frac{k_y+n\pi}{2}\right), \tag{4.7b}$$

$$c_n = 2t_{pp}J_n\left(\frac{A}{\sqrt{2}}\right)\left[e^{-in\pi/4}\cos\left(\frac{k_x+k_y+n\pi}{2}\right) - e^{in\pi/4}\cos\left(\frac{k_x-k_y+n\pi}{2}\right)\right]. \tag{4.7c}$$

With the noninteracting Floquet Hamiltonian, we can explicitly write down the Dyson equation as

$$\begin{pmatrix} \hat{G}^R_{\boldsymbol{k}} & \hat{G}^K_{\boldsymbol{k}} \\ 0 & \hat{G}^A_{\boldsymbol{k}} \end{pmatrix}(\omega) = \begin{pmatrix} \omega\hat{1}+\hat{\Omega}-\hat{H}(\boldsymbol{k}) & 0 \\ 0 & \omega\hat{1}+\hat{\Omega}-\hat{H}(\boldsymbol{k}) \end{pmatrix} - \begin{pmatrix} \hat{\Sigma}^R & \hat{\Sigma}^K \\ 0 & \hat{\Sigma}^A \end{pmatrix}(\omega) - \begin{pmatrix} \hat{\Sigma}^R_{\rm diss} & \hat{\Sigma}^K_{\rm diss} \\ 0 & \hat{\Sigma}^A_{\rm diss} \end{pmatrix}(\omega), \tag{4.8}$$

where

$$\hat{\Omega}_{\alpha\beta;mn} = n\Omega\delta_{\alpha\beta}\delta_{mn}, \tag{4.9a}$$

$$\hat{\Sigma}^{R,A}_{\rm diss}(\omega) = \mp i\Gamma\delta_{\alpha\beta}\delta_{mn}, \tag{4.9b}$$

$$\hat{\Sigma}^K_{\rm diss}(\omega) = -2i\Gamma\tanh\frac{\omega+n\Omega}{2T}\delta_{\alpha\beta}\delta_{mn}, \quad \alpha,\beta = d,p_x,p_y, \quad m,n\in\mathbb{Z}. \tag{4.9c}$$

Throughout this chapter we set, after the DMFT analysis of the *dp*-model by Macridin, *et al.* [74], the model parameters as follows:

$$t_{dp} = 1.6\text{eV}, \quad t_{pp} = 0.0\text{eV}, \quad \Delta = 4.5\text{eV}, \quad U = 9.0\text{eV}. \tag{4.10}$$

We also set a fermion heat bath at each site to study the steady states in the ac-fields. The heat bath parameters are taken as $\Gamma = 0.1$ eV and $T = 0.5$ eV. Hereafter, we set eV as the unit

of the energy.

4.3 Results

In this section we present the results on the steady states of the dp-model in circularly polarized ac-fields. The results essentially depend on the photon energy of the ac-electric field Ω. Here, we choose $\Omega = 4,8$, and 20 eV. As we shall discuss in the following subsections, $\Omega = 4,8$ eV correspond to charge excitation energies from Zhang-Rice band to the upper Hubbard band, and the p-band to the upper Hubbard band, respectively. $\Omega = 20$ eV is larger than the energy difference between the lower and the upper Hubbard bands and thus lies in an off-resonant regime.

Experimentally, mid-infrared to near-infrared light (100 meV ~ 2 eV) are chosen as a pump light, in pump-probe measurements. The reason for the choice of relatively large photon energies $\Omega \geq 4$ compared to experiments in our study is related to the computational cost of our calculation scheme. The bottleneck of our calculation is the process of solving the Dyson equation Eq. (4.8). The matrix size of the Green's functions is $(N_b N_F) \times (N_b N_F)$, where $N_b = 3$ is the number of orbitals and N_F is the size of the Floquet Green's functions, respectively. The computational cost for solving the Dyson equation equals to that for inversion of the matrices and thus $O(N_b^3 N_F^3)$. N_F should be chosen so that the total band width may be covered by the energy window $\Omega \times N_F$ of the Floquet Green's function. Thus, as Ω becomes smaller, the required value of N_F becomes larger and computational costs increase as the cube of N_F. For this reason, we have to take $N_F < 20$ so that the calculation may finish in realistic computational time. Our strategy is therefore to take Ω as small as possible ($\Omega \gtrsim 4$) and examine the tendency of the resulting steady states.

4.3.1 Off-resonant regime: Ω = 20 eV

First, we show the results in the off-resonant regime, that is, the photon energy Ω is much larger than the total band width. We set $\Omega = 20$, which turns out to satisfy the off-resonant condition. The bath temperature and the bath coupling strength are set $T = 0.5$ and $\Gamma = 0.1$, respectively.

In Fig. 4-5(a), we show the time-averaged total density of states $A(\omega)$ and the occupation density $N(\omega)$,

$$A(\omega) = \int_0^T \frac{dt_{\rm av}}{T} A(t_{\rm av}, \omega), \quad N(\omega) = \int_0^T \frac{dt_{\rm av}}{T} N(t_{\rm av}, \omega), \tag{4.11}$$

for various values of A. $A(t_{\rm av}, \omega)$ and $N(t_{\rm av}, \omega)$ are the density of states and the occupation density at time $t_{\rm av}$, defined in Eq. (2.29). Our results in equilibrium qualitatively agree with the preceding DMFT study of the dp-model reported by Macridin, *et al*. [77], except that the bath coupling makes the structure broader. The character of the density of states is given by partial density of states in Fig. 4-5(b). The structure around $\omega = -8$ and $\omega = 2$ are the lower Hubbard band (LHB) and the upper Hubbard band (UHB), respectively. They are mainly composed of the d-orbitals and separated by $U = 9$. A sharp structure at $\omega = -4$ is the the p-band.

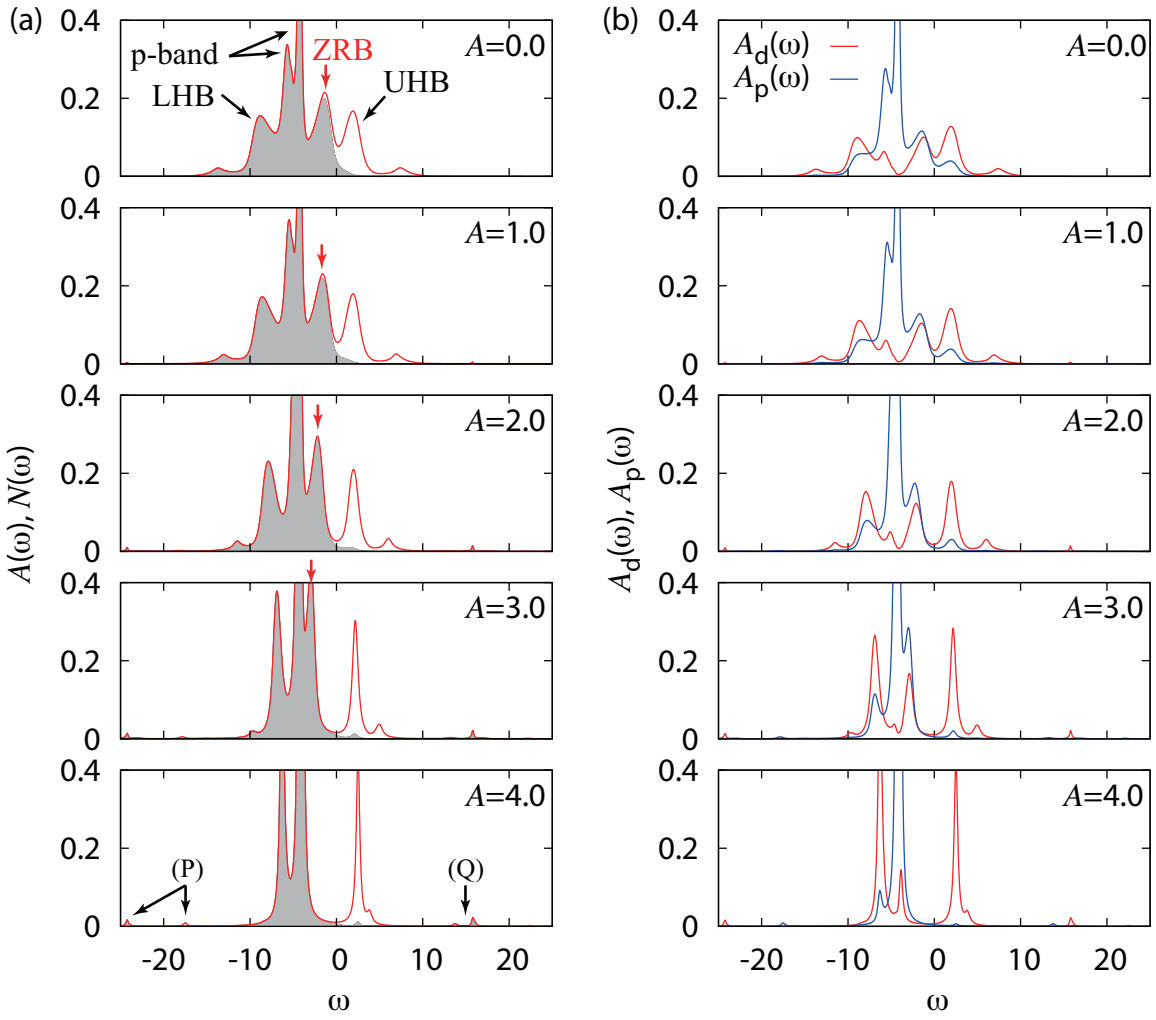

Figure 4-5: (a) Total density of states $A(\omega)$ (red solid lines) and the density of occupied states $N(\omega)$ (shaded region), and (b) partial density of states, $A_d(\omega)$ and $A_p(\omega)$, for each orbital, in an off-resonant circularly polarized light $\Omega = 20$. Parameters are $T = 0.5$ and $\Gamma = 0.1$. The intensity of the field A is varied from 0 to 4. LHB (lower Hubbard band), UHB (upper Hubbard band), ZRB (Zhang-Rice band) and the p-bands are assigned. Photo-induced bands that appear in a large intensity regime ($A = 4.0$) are marked as (P) and (Q).

More importantly, the structure at $\omega = -1$ is the so called Zhang-Rice band (ZRB), a hybridized band composed of the p-band and the d-band. Doped holes in equilibrium are doped into ZRB and thus an effective single-band picture proposed by Zhang, *et al*. [9] is justified in equilibrium.

The width of each peak is reduced as the intensity A is increased for the following reason. As shown in the Floquet Hamiltonian Eq. (4.7), an external field gives the factor $J_0(A/2)$ to the hopping matrix element t_{dp} and causes effective shrinking of the band width. Therefore the system becomes completely dispersionless as $A/2$ reaches the zeros of the Bessel function $J_0(x)$, i.e. $A \simeq 4.8$. The physical reason for this shrinkage is understood by time average over

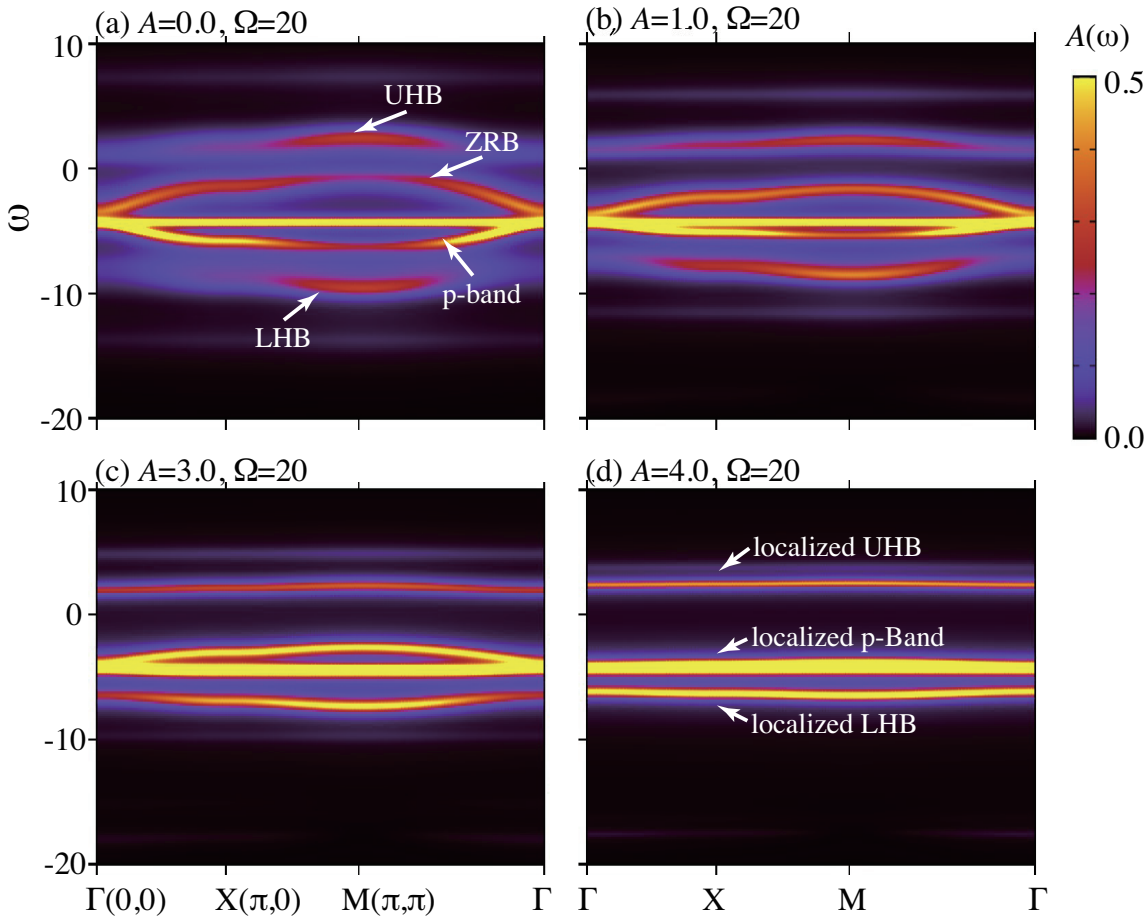

Figure 4-6: $\boldsymbol{k}$-resolved density of states in an off-resonant linearly polarized light. $\boldsymbol{k}$-points are sampled along $\Gamma(0,0)$-X$(\pi,0)$-M(π,π)-$\Gamma(0,0)$. Parameters are $T = 0.5$ and $\Gamma = 0.1$. The intensity of the fields A is varied from 0 to 4.

the Bloch oscillation, known as the *dynamical localization* of electrons in ac-fields [78].

For large intensity of the field, Floquet sidebands grow. In fact, there exist photo-induced bands far above the Fermi level, marked as (P) and (Q) in Fig. 4-5(a).

To investigate the detailed electronic structure, in Fig. 4-6 we plot the $\boldsymbol{k}$-resolved spectral function for various values of A. We clearly see that electrons become dispersionless as the intensity A is increased. Subsequently, due to the reduction of the d-p hybridization t_{dp}, the ZRB, a hybridized band with a d-orbital and a p-orbital, is suppressed. In other words, ZRB is not rigid against photo-irradiation and therefore the single-band picture can be degraded in the photo-doping case.

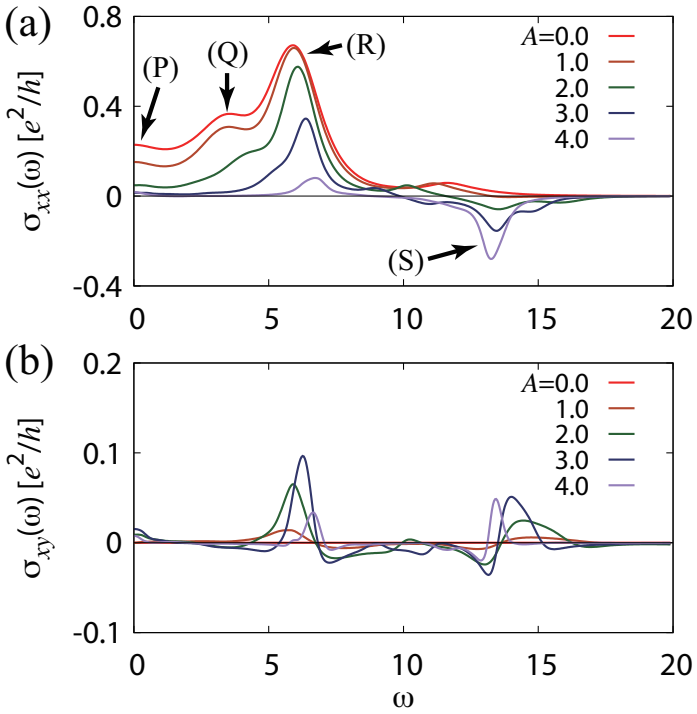

Figure 4-7: Optical conductivities $\sigma_{xx}(\omega)$ and $\sigma_{xy}(\omega)$ in an off-resonant circularly polarized light, $\Omega = 20$. Parameters are $T = 0.5$ and $\Gamma = 0.1$. The intensity of the field A is varied from 0 to 4. For the explanation of the structures marked as (P) , (Q), (R) and (S), see the text.

Optical conductivities are also shown in Fig. 4-7. The longitudinal conductivity $\sigma_{xx}(\omega)$ (Fig. 4-7(a)) for $A = 0$ is consistent with the previous study by Wang, *et al*. [77]. The structure (P) around $\omega = 0$ is due to the thermal excitations near the Fermi level. The structure (Q) corresponds to the photo-excitation process ZRB→UHB, while (R) to the p-band→UHB. The deformation of the spectra with increasing A is understood as follows. The peak (P) is due to the electronic states near the Fermi levels and therefore suppressed as the system becomes dispersionless and the density of states decreases near the Fermi level. The peak (Q) is also suppressed since ZRB itself vanishes.

Interestingly, a negative conductivity grows near $\omega = 14$, labeled as (S) in Fig. 4-7. In general, a negative conductivity at ω indicates the population inversion between the electronic states with the distance ω in energy.

The population inversion can be visualized by considering the distribution function $f_{\boldsymbol{k}}(\omega) \equiv A_{\boldsymbol{k}}(\omega)/N_{\boldsymbol{k}}(\omega)$. In Fig. 4-8 we show the distribution function for several values of A. We see that the Fermi-Dirac distribution function at $A = 0$ is deformed and has a characteristic structure around $\omega \simeq \pm 15$. This suggests that the photo-induced band marked as (P) and (Q) in Fig. 4-5(a) are filled with holes and electrons, respectively. Therefore, the population inversion, a necessary condition for the negative optical conductivity, is indeed realized in this case.

The optical Hall conductivity $\sigma_{xy}(\omega)$ is also calculated and shown in Fig. 4-7(b). $\sigma_{xy}(\omega)$ is related to the Kerr and Faraday rotations [79], and thus we expect our calculation gives some insights into the experiments of Kerr and Faraday rotations for cuprates under the influence of circularly polarized fields. The analysis of $\sigma_{xy}(\sigma)$ is a future consideration.

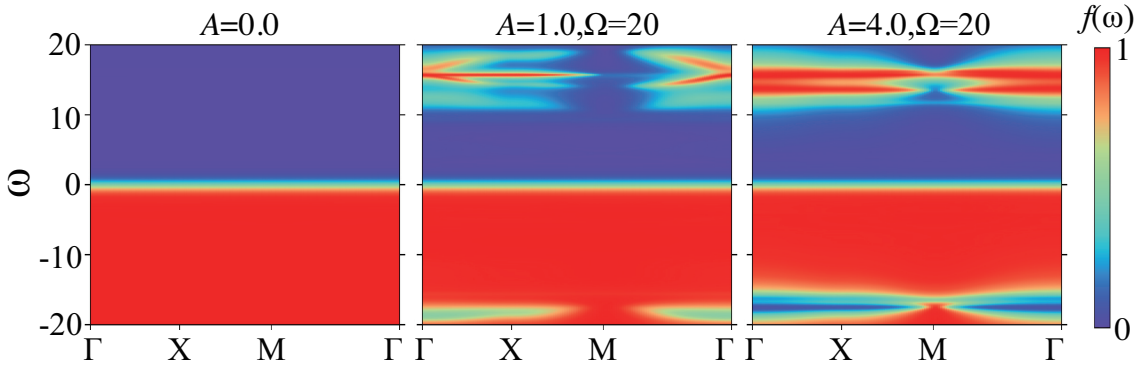

Figure 4-8: $\boldsymbol{k}$-resolved distribution function in an off-resonant circularly polarized light with $\Omega = 20$. $\boldsymbol{k}$-points are sampled along $\Gamma(0,0)$-X$(\pi,0)$-M(π,π)-$\Gamma(0,0)$. Parameters are $T = 0.5$ and $\Gamma = 0.1$. The intensity of the field A is varied from 0 (a) to 4 (d).

4.3.2 Resonant regime: Ω = 4.0 eV and 8.0 eV

Next we turn to the resonant regime. We choose two photon energies, $\Omega = 4.0$ ($\simeq$ excitation energy from ZRB to UHB), and $\Omega = 8.0$ ($\simeq$ excitation energy from the p-band to UHB).

The total density of states and partial density of states are shown in Fig. 4-9(a)(b). A substantial difference from the off-resonant case appears in the photo-carriers for the relatively weak intensity A. By observing the occupation density $N(\omega)$ in Fig. 4-9(a), we can see that holes and electrons are doped to the p-band and UHB, respectively, as the intensity A increases. On the other hand, the position of each band is almost unchanged, in contrast to the off-resonant case ($\Omega = 20$), in which the band structure highly deviates from equilibrium. For example, ZRB marked as red arrows in Fig. 4-9(a), survives in the large intensity regime, while in an off-resonant case (Fig. 4-5(a)) ZRS vanishes. This indicates that the rigid-band picture may hold for weak intensity fields in a resonant regime.

The momentum-resolved distribution function is plotted in Fig. 4-10. For $\Omega = 4.0$ (Fig. 4-10(a)), the distribution function is almost monotonic, which resembles the Fermi-Dirac distribution function at high temperatures. For $\Omega = 8.0$ (Fig. 4-10(b)), on the other hand, the distribution function is highly non-monotonic. In particular, there is a structure around $\omega \simeq 5$, suggesting population inversion at UHB.

In Fig. 4-11(a), we plot optical conductivities. For $\Omega = 4.0$ (left top panel), we observe the reduction of the longitudinal conductivity. This behavior is understood as the effective high-temperature effect. When the temperature becomes higher, electrons below [holes above] the Fermi level are decreased due to the thermal excitations, and thus the optical transition is suppressed. This results in the reduction of optical conductivities. For $\Omega = 8.0$ (right top panel), we have a negative optical conductivity near $\omega = 3$ for higher values of A. This is again due to the population inversion, as we stated above.

4.4 Concluding remarks

4.4.1 Summary of our calculation

In this chapter, we have investigated steady states in the dp-model in circularly polarized ac electric fields for various values of photon energy Ω and intensity A, and observed significant qualitative differences in the steady states between off-resonant and resonant cases. We numerically calculated the momentum-resolved density of states, distribution functions and optical conductivities and we obtained the following results.

- For off-resonant photon energy $\Omega = 20$ eV, the distribution function stays almost monotonic near the Fermi level (Fig. 4-8) for large $A \geq 2$, while the band structure highly deviates from the original one. The population inverted photo-induced bands appear far away from the Fermi level, and thus we observe negative optical conductivities.

- For a smaller photon energy $\Omega = 8.0$ eV, corresponding to the resonance energy between the p-band and UHB, we observe deformation of the distribution function for small A, and the band structure is almost unchanged in that intensity of A. The distribution

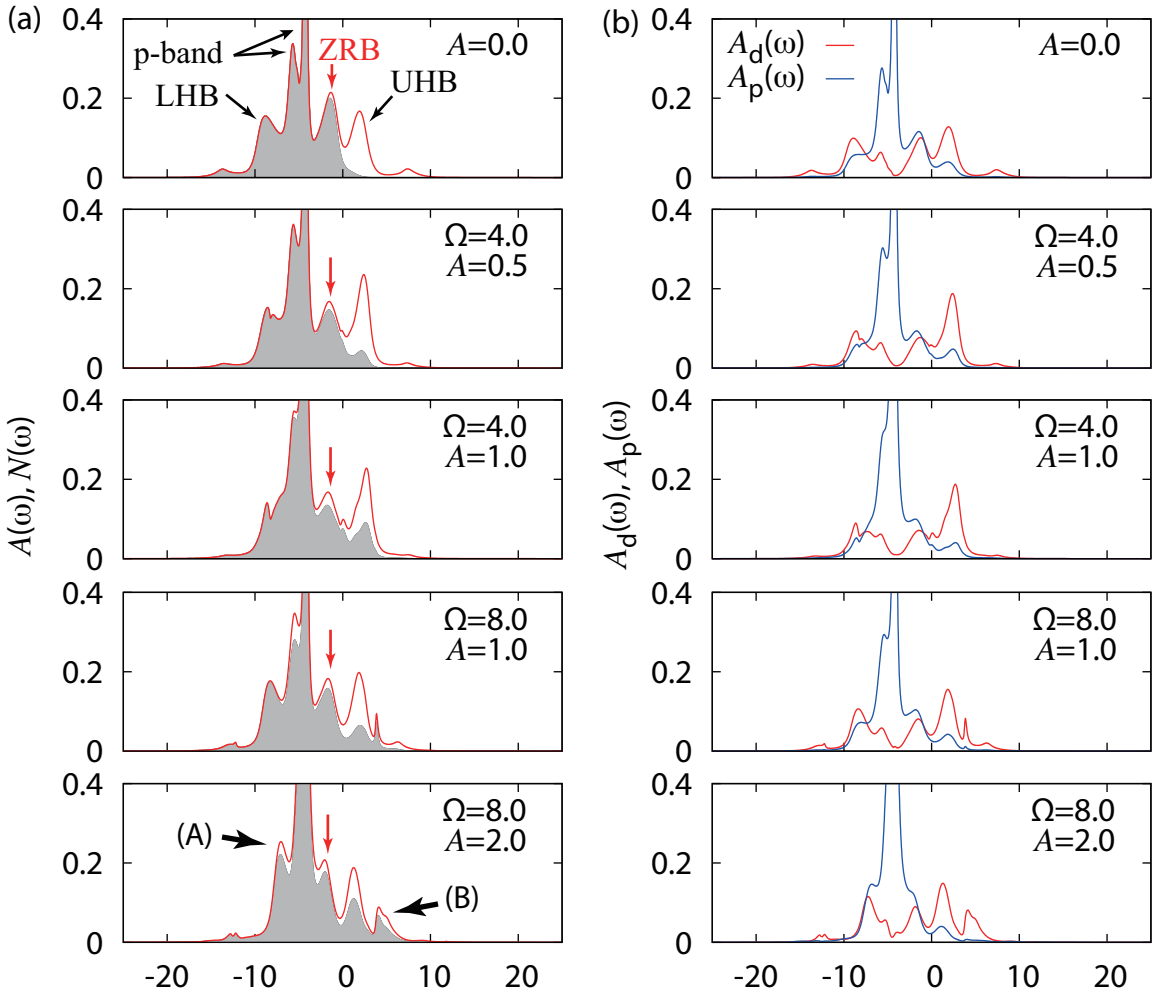

Figure 4-9: (a) Total density of states $A(\omega)$ (red solid lines) and the density of occupied states $N(\omega)$ (shaded region), and (b) partial density of states, $A_d(\omega)$ and $A_p(\omega)$, for each orbital, in a resonant circularly polarized light $\Omega = 4.0, 8.0$. Parameters are $T = 0.5$ and $\Gamma = 0.1$. The intensity of the field A is varied from 0 to 2. Population-inverted bands are marked as (A) and (B).

function suggests the population inversion (Fig. 4-10(b)) and the system exhibits negative optical conductivities.

- For a small photon energy $\Omega = 4.0$ eV, corresponding to the resonance energy between ZRB and UHB, the distribution function deviates from the original distribution function for small $A < 2$ (Fig. 4-10(a)), and resembles the Fermi-Dirac distribution function at higher temperatures. Therefore, the effect of the external fields may be understood as the effective rise of the temperature of the system.

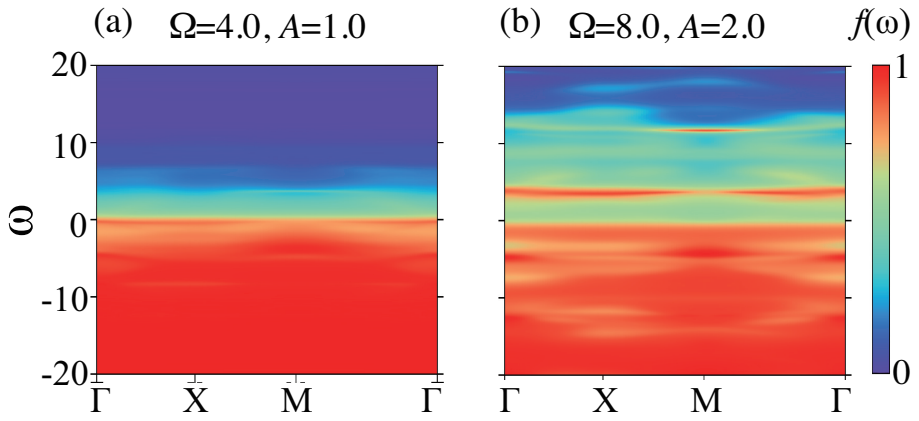

Figure 4-10: $\boldsymbol{k}$-resolved distribution function in a resonant circularly polarized lights, $(\Omega, A) = (4.0, 1.0)(a), (8.0, 2.0)(b)$. $\boldsymbol{k}$-points are sampled along $\Gamma(0,0)$-X$(\pi,0)$-M(π,π)-$\Gamma(0,0)$. Parameters are $T = 0.5$ and $\Gamma = 0.1$.

4.4.2 Required electric field intensities

Finally, let us remark on the intensity of the field experimentally required for the phenomena predicted here. From the definition of A, the amplitude of the electric field is $E = A\Omega$, and thus we have

$$E = \left(\frac{eaA}{\hbar}\right)\left(\frac{\hbar\Omega}{e}\right)\frac{1}{a}, \tag{4.12}$$

where a is the lattice constant. $(eaA/\hbar)$ is dimensionless, while $\hbar\Omega/e$ and a have the dimension of voltage and length, respectively. Thus we can express the amplitude in units of kV/cm, which is commonly used in optical experiments as

$$E = 2.5\left(\frac{eaA}{\hbar}\right)\left(\frac{\hbar\Omega}{1\mathrm{eV}}\right) \times 10^4\,[\mathrm{kV/cm}], \tag{4.13}$$

where we have set $a = 4$Å, a typical lattice constant in the cuprates. The intensity of the field is calculated as

$$\begin{aligned} I &\equiv \frac{1}{2}\epsilon_0 E^2 c \\ &= 8.3\left(\frac{eaA}{\hbar}\right)^2\left(\frac{\hbar\Omega}{1\mathrm{eV}}\right)^2 \times 10^{11}\,[\mathrm{W/cm^2}], \end{aligned} \tag{4.14}$$

where $\epsilon_0 = 8.854 \times 10^{-12}$ F/m is the vacuum permittivity and $c = 3.0 \times 10^8$ m/s is the velocity of light.

Let us compare the value of Eq. (4.14) with the intensity of pump light in pump-probe measurements. The typical photon energy Ω is in the range of 1 eV to 10 eV, while the absorption energy is estimated as 10-100 mJ/cm^2 [25, 80, 81]. Assuming that the typical pulse-width is ~100 fs, we estimate that the intensity in pump-probe measurements is about $10^{12} \sim 10^{13}$ W/cm^2. In our calculation we have used $(eaA/\hbar) \sim 1$ and $\hbar\Omega \sim 10$ eV. Substituting

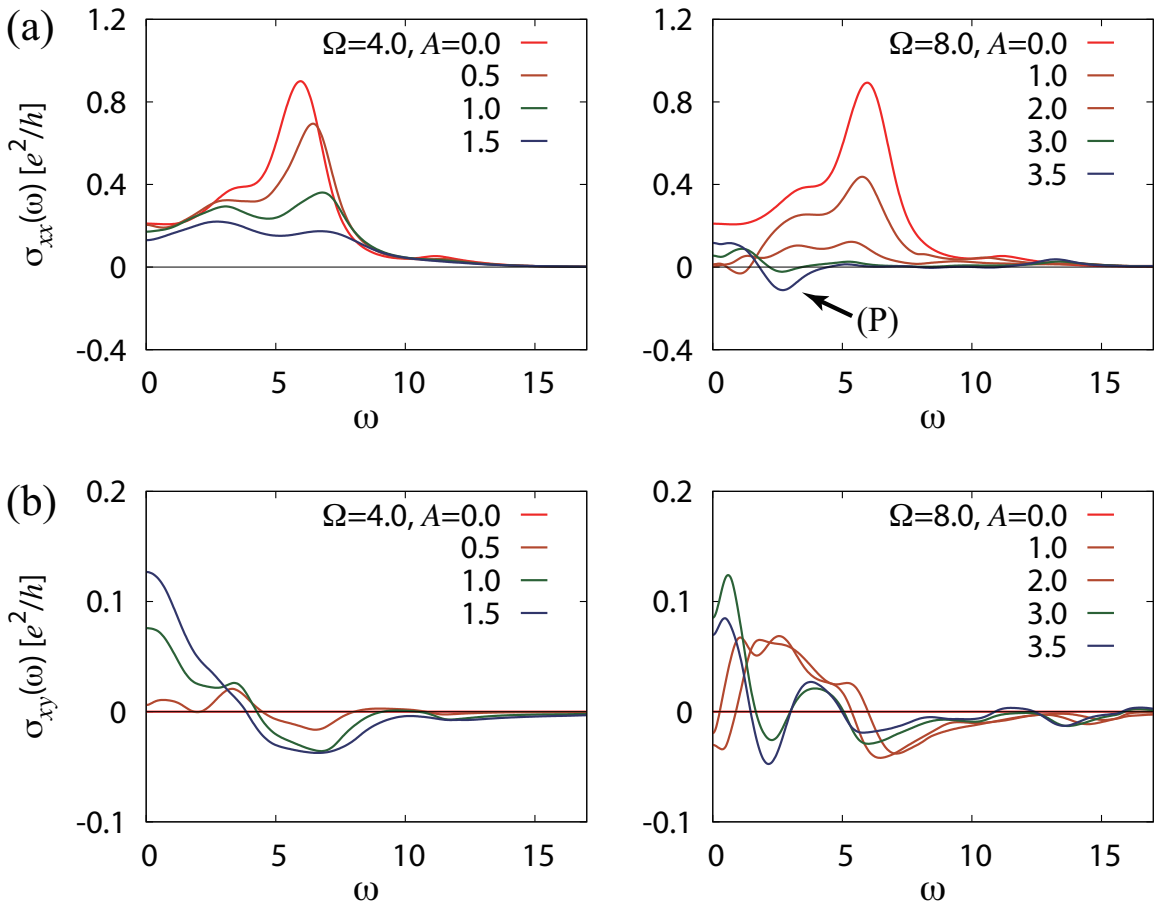

Figure 4-11: Optical conductivities $\sigma^{xx}(\omega)$ and $\sigma^{xy}(\omega)$ in an off-resonant circularly polarized light. Parameters are $T = 0.5$ and $\Gamma = 0.1$. The photon energy is set to $\Omega = 4.0, 8.0$ and the intensity of field A is varied from 0 to 3.5.

this into Eq. (4.14), we estimate the intensity of the field I at $10^{13} \sim 10^{14}$, which is comparable to the situations of real experiments. This rough estimation of the injected amount of energy indicates that the intensity of the fields required in our study may be realized in the pump-probe measurements.

4.4.3 Discussions and future works

We have obtained the results based on Floquet-DMFT with an impurity solver based on a weak-coupling perturbation theory. The validity of our approximation should be checked by comparing with other numerical impurity solvers. One candidate is the non-crossing approximation (NCA) [82, 83], which is based on a strong-coupling perturbation theory. NCA is analytically formulated in terms of Green's functions and can be extended to time-dependent problems [84]. Steady state formalism for NCA can also be established by extending the Green's function to Floquet-Green's functions.

To investigate ordered phases is also important works that we have left in this study.

As we stated in the introduction, doped cuprates exhibit antiferromagnetic order or d-wave superconductivity. Oka, *et al.* [85] studied the dc-biased Hubbard model and obtained the nonequilibrium phase diagram for antiferromagnetic and superconducting phases. It is important to investigate the phase diagram for the ac-driven dp-model and to present a guideline for pump-probe experiments for cuprates.

Chapter 5

Photo-induced phase transitions in Hubbard model on honeycomb lattice

In this chapter, we study the nonequilibrium steady state of the honeycomb-Hubbard model in circularly polarized electric fields, as a paradigm of the interplay between photo induced topological properties and electron correlations.

We study intense-field and strongly correlated regimes with multi-band Floquet-DMFT for the first time, and investigate how the photo-induced phase transition manifests itself under the influence of circularly polarized fields.

We show that the system exhibits a novel photo-induced Mott transition and topological-topological phase transitions. We shall discuss the properties of the phases by numerical calculation of electronic structures and transport coefficients. Besides the numerical simulation, we develop an analytic perturbation theory for Floquet states. We shall show that the honeycomb lattice in the circularly polarized light can be mapped to an effective model, whose properties are consistent with our numerical results.

5.1 Introduction

5.1.1 Discovery of topological phenomena: the integer quantum Hall effects

Topological properties in condensed matter are one of the most important topics in multi-band systems and have been studied intensively to uncover beautiful connections between topological aspects in quantum physics and quantum phenomena in real materials. The study of topology in condensed matter originates from the discovery of the integer quantum Hall effect (IQHE) in a two-dimensional electron system by Klitzing, *et al.* [86]. They measured the Hall conductivity σ_{xy} of the inversion layer in the MOSFETs (metal-oxide semiconductor field-effect transistors) in an intense magnetic field, and discovered that σ_{xy}

is quantized as

$$\sigma_{xy} = n\frac{e^2}{h}, \quad n \in \mathbb{N}. \tag{5.1}$$

IQHE can be explained by the formation of Landau levels in magnetic fields. According to the quantum mechanics of free electrons in magnetic fields, the energy levels of electrons in a magnetic field B are quantized as

$$E_n = \hbar\omega_c\left(n + \frac{1}{2}\right), \quad n \in \mathbb{N}, \tag{5.2a}$$

$$\omega_c = \frac{eB}{mc}, \tag{5.2b}$$

where ω_c is the cyclotron frequency. In the presence of the Landau levels, the Hall conductivity is given by Eq. (5.1) when n Landau levels are fully occupied while other Landau levels are empty. After the discovery of IQHE, Thouless *et al.* pointed out [18] that the quantization of σ_{xy} can be understood in terms of topological invariants for each Landau level. They showed the so-called TKNN formula

$$\sigma_{xy} = \sum_{\alpha:\text{occupied}} \frac{e^2}{h}\nu_\alpha, \tag{5.3a}$$

$$\nu_\alpha = \int \frac{d\boldsymbol{k}}{2\pi}\mathscr{B}_{\alpha\boldsymbol{k}}, \tag{5.3b}$$

$$\mathscr{B}_{\alpha\boldsymbol{k}} = \left[-i\nabla_{\boldsymbol{k}} \times \langle u_{\alpha\boldsymbol{k}}|\nabla_{\boldsymbol{k}}|u_{\alpha\boldsymbol{k}}\rangle\right]_z, \tag{5.3c}$$

for noninteracting multi-band systems, where α is a band index and $|u_{\alpha\boldsymbol{k}}\rangle$ is a Bloch wave function. $\mathscr{B}_{\alpha\boldsymbol{k}}$, defined by $\boldsymbol{k}$-derivatives of the Bloch wave function for the αth band, serves as a curvature of the Brillouin zone, and thus called the *Berry curvature* [87]. Accoring to differential geometry, ν_α, the integral of $\mathscr{B}_{\alpha\boldsymbol{k}}$ over the Brillouin zone, is always an integer. ν_α, the so-called *Chern number* [88], is a topological invariant that is pinned to an integer as long as the system is continuously deformed without crossing any phase boundaries. The fact that σ_{xy} is proportional to the sum of topological invariants of occupied bands implies that σ_{xy} is pinned to a quantized value which topologically classifies the electronic state. Applying this argument to two-dimensional electron systems in magnetic fields, Thouless, *et al*. clearly explained the relation between the topological aspects of multi-band electron systems and IQHE.

Thouless, *et al.* showed that the existence of topologically nontrivial bands with nonzero Chern numbers $\nu_\alpha \neq 0$ is a requirement for IQHE and thus nontrivial topological bands are indeed realized in integer quantum Hall systems. Then it is natural to pose a question, "in which systems the nontrivial topological bands show up, besides electron systems with intense magnetic fields?."

5.1.2 Novel topological phases in honeycomb lattice: topological insulator

The pioneering work was done by Haldane [19], who found novel topological states of fermions on a honeycomb lattice *even in the absence of net magnetic fields*. In Fig. 5-1(a) we depict the lattice structure of Haldane's toy model, where black dots represent atoms of the same kind,

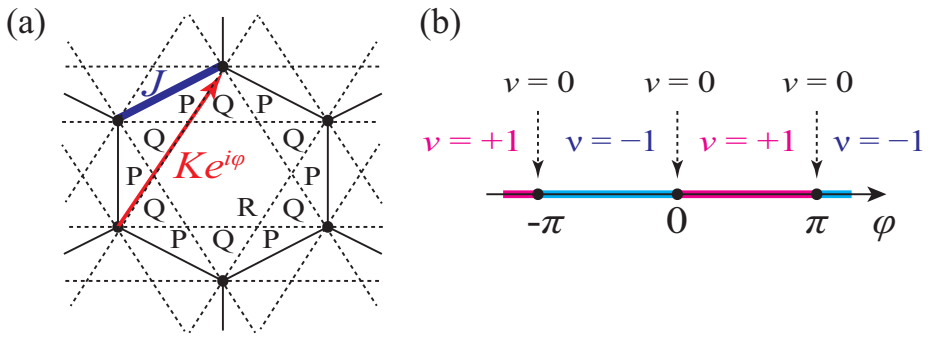

Figure 5-1: (a) The Haldane model [19]. Black solid and dashed lines represent NN and NNN hopping paths, respectively. These lines divide the unit cell into three regions, P, Q and R as labeled in the figure. Magnetic fluxes $\pm\varphi$ are passing through P and Q regions, respectively, while no magnetic field is applied to R regions. J and $Ke^{i\varphi}$ are NN and NNN hopping matrices, respectively. (b) A phase diagram of the Haldane model [19]. The flux φ is varied with a fixed ratio $K/J \neq 0$. For $\varphi \equiv 0 \mod \pi$, the system is trivial with $\nu = 0$, otherwise topologically nontrivial states with finite Chern numbers ($\nu = \pm 1$ for pink and blue regions in the fugure, respectively) appear.

and solid and dashed lines are nearest-neighbor (NN) and next-nearest-neighbor (NNN) hopping paths, respectively. The parameters J and K are amplitudes of NN and NNN hopping. This lattice structure is indeed realized in real materials, such as graphene [89] and silicene [90]. He assumed spatially alternating magnetic fields applied perpendicular to the lattice plane, and he set magnetic fluxes $\pm\varphi$ passing through P and Q regions in Fig. 5-1, respectively. As a result of the alternating flux, the NNN hopping acquires a phase factor as $Ke^{i\varphi}$. In Fig. 5-1(b) we show the phase diagram of the Haldane model for a fixed ratio K/J. By calculating the Chern number of the occupied band ν, he found a topological phase for $\varphi \neq 0$. His finding is quite interesting in two points: (1) nontrivial topological state ($\nu \neq 0$) appears even in the absence of Landau levels as in integer quantum Hall states, and (2) electronic system in a honeycomb lattice is at a marginal point between trivial ($\nu = 0$) and nontrivial ($\nu \neq 0$) topological states and thus topological phase transitions take place for an infinitely small perturbation, the alternating flux φ, which explicitly breaks the time-reversal symmetry.

Recently, Kane and Mele [20, 21] extended Haldane's argument to a more realistic model *having the time-reversal symmetry*. If we write the Hamiltonian for the Haldane model with the alternating flux φ as $\mathscr{H}_{\text{Haldane}}(\varphi)$, the Kane-Mele model is simply written as

$$\mathscr{H}_{\text{Kane-Mele}} = \begin{pmatrix} \mathscr{H}^{\uparrow}_{\text{Haldane}}(\varphi) & \mathscr{R}^{\dagger} \\ \mathscr{R} & \mathscr{H}^{\downarrow}_{\text{Haldane}}(-\varphi) \end{pmatrix}, \tag{5.4}$$

where the symbols $\uparrow, \downarrow$ are spin indices and $\mathscr{R}$ is a spin-spin scattering process that does not violate the time-reversal symmetry. The point is that the Kane-Mele model has the time-reversal symmetry, that is, the Hamiltonian Eq. (5.4) is unchanged by the time-reversal operation: $\varphi \to -\varphi$ and $\uparrow [\downarrow] \to \downarrow [\uparrow]$. The Kane-Mele model can be realized when some intrinsic spin-mixing processes, such as spin-orbit interactions, are present, and fictitious alternating

magnetic fields, assumed in the Haldane model, are no longer necessary. They constructed a topological number, called $\mathbb{Z}_2$ topological invariant, as a natural extension of the Chern number, and showed the Kane-Mele model indeed has nontrivial topological states that is classified by the $\mathbb{Z}_2$ topological invariant. The topologically nontrivial state in the Kane-Mele model carries a spin current (the quantum spin-Hall effect) and has characteristic edge states (chiral edge states). Based on the theoretical predictions, band insulators with nontrivial topological bands, *topological insulators* [23], are recently found in various materials with a strong spin-orbit interaction, such as two-dimensional HgTe quantum wells [91], or even three-dimensional materials, Bi_2Se_3 [92] and Bi_2Te_3 [93].

5.1.3 Topological states in an ac-driven honeycomb lattice

Besides Kane and Mele's idea, Oka and Aoki [29] showed that topologically nontrivial state can also be realized by applying external electric fields. They showed, as we have shown in Chapter 3, that the Hall conductivity in ac-electric fields can be written in terms of Floquet states as

$$\sigma_{xy} = \sum_m \frac{e^2}{h} \int \frac{d\boldsymbol{k}}{2\pi} \mathscr{B}_{m\boldsymbol{k}} f_{m\boldsymbol{k}}, \tag{5.5a}$$

$$\mathscr{B}_{m\boldsymbol{k}} = \left[-i\nabla_{\boldsymbol{k}} \times \langle u_{m\boldsymbol{k}} | \nabla_{\boldsymbol{k}} | u_{m\boldsymbol{k}} \rangle \right]_z, \tag{5.5b}$$

where m labels Floquet bands, $|u_{m\boldsymbol{k}}\rangle$ and $f_{m\boldsymbol{k}}$ are a Floquet wave function and its occupation number, respectively. The photo-induced Berry curvature $\mathscr{B}_{m\boldsymbol{k}}$ also serves as a curvature and its $\boldsymbol{k}$-integral over the Brillouin zone gives a topological invariant, analogous to the TKNN formula. Oka and Aoki observed the low-lying electron dispersion in circularly polarized fields and analytically showed that a metal-to-topological-insulator phase transition indeed takes place. They also numerically demonstrated that the Hall effect does appear under the influence of circularly polarized fields, as a result of the photo-induced Berry curvature. The quantization of the photo-induced Hall conductivity is confirmed by a numerical study of the transport properties of graphene ribbons in circularly polarized fields [94].

Photo-induced topological states are further investigated by Kitagawa, *et al.* [34], who uncovered a connection between topological states in an ac-driven honeycomb lattice and the original Haldane model. They start from the honeycomb lattice with NN hopping J in circularly polarized ac-fields. In the ac-electric fields with frequency Ω, electrons can absorb or emit photon energy $\hbar\Omega$, and transfer to another Floquet states. In the limit of weak intensity of the field, the transition amplitude is proportional to the intensity. They developed the perturbation technique with respect to the external field and concluded that the second-order perturbation of the field gives rise to an effective NNN hopping, $K \propto iJ^2$, which is analogous to the Haldane model in the case of the alternating flux $\varphi = \pi/2$. The NNN hopping appears due to the two photo-assisted hopping processes, as depicted in Fig. 5-2. Thus the photo-induced phase transition in a honeycomb lattice is understood by the analogy of the Haldane model, at least in the weak-field regime.

There are still unanswered questions for the photo-induced topological states. One is the effect of nonequilibrium distribution function $f_{m\boldsymbol{k}}$ which appeared in Eq. (5.5). As is already

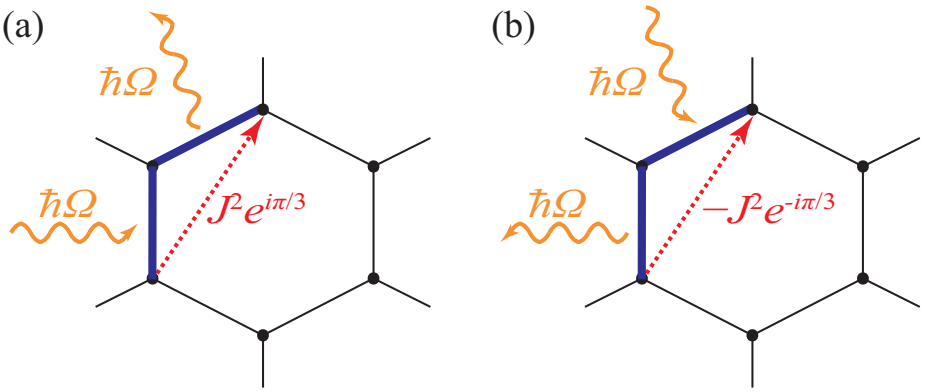

Figure 5-2: Effective NNN hopping processes on a honeycomb lattice in circularly polarized ac-fields, discussed by Kitagawa, *et al.* [34]. J is the NN hopping amplitude and Ω is the frequency of the ac-field. In (a) we show a second-order perturbation process, with NN hoping with single photon absorption and subsequent NN hoping with single photon emission, resulting in an effective NNN hopping matrices $J^2e^{i\pi/3}$. In (b) we show another second-order perturbation process, with single photon absorption process after single photon emission process. The two matrices add up to an effective NNN hopping matrix $i\sqrt{3}J^2$, which is equivalent to Haldane's NNN hopping for the flux $\varphi = \pi/2$.

demonstrated in a Floquet-DMFT study in the single-band Hubbard model [35], nonequilibrium distribution functions can highly deviate from the Fermi-Dirac distribution function. Since the external ac-fields induce not only the Berry curvature but also the deformation of the distribution function, it is important to clarify how the nonequilirium distributions affect the topological nature under the influence of ac-fields. Another question is about the topological states in circularly polarized ac-fields with strong intensity. When the field intensity becomes large, the mapping to the Haldane model, studied previously in the weak intensity regime, may not hold. Thus it is interesting to investigate whether or not the new topological states appear in the strong field regime.

5.1.4 Electron correlation in a honeycomb lattice

So far, we have assumed that electrons on a honeycomb lattice are noninteracting. However, electron correlation is also an important physics that drives the system into qualitatively different states.

At half-filling, the honeycomb-lattice model is semimetallic in the one-body picture. The low-lying dispersion is gapless, while the density of states is exactly zero at the Fermi level, at which the low-lying dispersions touch at special points in the $\boldsymbol{k}$-space. The semimetalic nature makes the Mott transition qualitatively different from that of correlated massive electrons as we mention below. This characteristic Mott transition in the semimetal is called "semimetal-insulator transition (SMIT)". Physics of SMIT in the honeycomb-Hubbard model has been studied by various authors. Santoro *et al.* [95] developed DMFT on the infinite diamond lattice, an extension of the honeycomb lattice to the infinite coordination number, and revealed that the model possesses a rich phase diagram that includes semimetallic, Mott

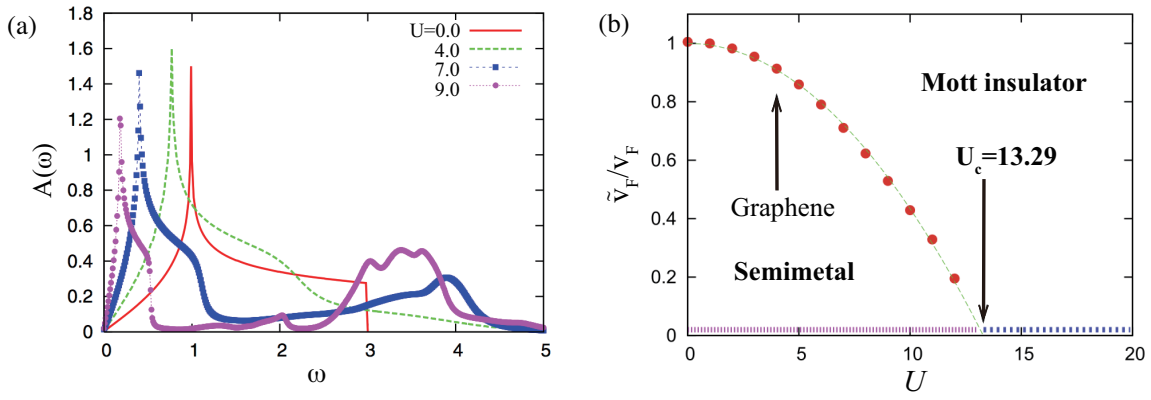

Figure 5-3: (a) The local density of states $A(\omega)$ against ω and (b) the renormalized Fermi velocity $\tilde{v}_F$ against v_F normalized by the free Fermi velocity v_F for the honeycomb-Hubbard model [97], reprinted with kind permission from Springer Science + Business Media. The impurity solver of DMFT is the second-order iterated perturbation theory. The nearest-neighbor hopping is taken as the unit of energy.

insulating, and antiferromagnetic phases.

Ebrahimkhas and Jafari [96, 97] studied SIMT in the two-dimensional honeycomb-Hubbard model with DMFT and revealed that SIMT is accompanied by a renomalization of the Fermi velocity. In Fig. 5-3 we show the spectral function and the renormalized Fermi velocity for various values of U, after Ref. [97]. The density of states in Fig. 5-3(a) have the V-shaped structure at the Fermi level $\omega = 0$ for each U, showing that there exist Dirac points at $\omega = 0$ up to a large value of U and thus the Dirac dispersion is robust against the Hubbard interaction. As U becomes larger, the structure around ω shrinks due to the reduction of the quasiparticle weight Z, as we discuss in this chapter. Instead, another structure develops around $\omega \simeq U/2$ which corresponds to the upper Hubbard band. Since the bare Fermi velocity v_F is also renormalized by the quasiparticle weight Z as $\tilde{v}_F = Zv_F$, one can estimate the value of Z by taking the ratio $\tilde{v}_F/v_F$, which is plotted in Fig. 5-3(b) against U. In this case, the critical value U, over which the quasi particle weight Z vanishes, is around $U_c \simeq 13.3$.

It is important to mention actual values of U in real materials. Wehling, *et al.* [98] estimated the Coulomb interactions in graphene within the constrained random phase approximation (cRPA) [99], and they calculated the on-site repulsion $U = 3.3J$ and the nearest-neighbor repulsion $V = 2.0J$, where $J = 2.8$ eV is the NN hopping amplitude for graphene. By carrying out the renormalization of the nearest-neighbor interaction V based on a variational principle, Schüler, *et al.* [100] evaluated the effective Hubbard interaction $U = 1.6J$ for graphene. The estimated value is much smaller than the critical value U_c for SMIT.

However, the value of U/J can vary from system to system. In fact, Schüler, *et al.* also calculated for silicene, a two-dimensional material with honeycomb lattice composed of silicon atoms, and they reported $U/J = 2.0$ [100]. Moreover, the honeycomb lattice is recently simulated in bosonic [101, 102] and fermionic cold atoms [103]. In the cold atoms, the Hubbard interaction can become even stronger due to the strong localization of the atoms, and thus the strongly correlated regime in a honeycomb lattice may be realized.

Even if the system is weakly correlated with small U/J, effects of electron correlation on topological properties are not at all trivial. The electron correlation does not explicitly break the time-reversal symmetry and therefore one may expect that the topological characters are not disturbed by electron correlation. However, the topological invariants that we have discussed in the previous section are constructed by *noninteracting* Bloch wave functions. When the interaction is switched on, the electronic state may significantly differ from noninteracting states and thus one needs to extend the notion of topological invariant to interacting systems, which has not been fully understood [104, 105].

5.1.5 Motivation and key results of this study

Having overviewed the recent developments in electronic systems in the honeycomb lattice, we are now in the position to pose an interesting question that have not been answered yet: "how the photo-induced phase transition manifests itself in the intense-field regime, or in the correlated regime?" To investigate the correlated and intense-field regimes on a equal footing, we apply the multi-band Floquet-DMFT formalism, which we established in Chapter 3, to the Hubbard model on the honeycomb lattice. We investigated the honeycomb-lattice systems from the weakly correlated regime to the highly correlated regime, under the influence of circularly polarized field with frequency Ω. The key results are summarized as follows.

- For the high-frequency regime $\Omega > W$ (W is the band width), the system exhibits a novel photo-induced Mott transition, even for small value of U/J. Further, for strong field regime, the system exhibits topological-topological phase transition which is characterized by quantized values of the Hall conductivity.

- We shall extend the perturbation technique that Kitagawa, *et al.* [106]) developed to the regime of large photon energy ($\Omega/W \gg 1$). Using the formalism we shall show that the honeycomb lattice in the circularly polarized light can be mapped to an effective Haldane model in the limit of small W/Ω, and demonstrate that the novel phase transitions in the high-frequency regime can be understood by the static properties of the effective Hamiltonian.

- For the small-frequency regime $\Omega \leq W$, the Hall conductivity has sign-change dependence on the frequency Ω. We shall clarify the origin of this sign change as an effect of the nonequilibrium distribution function.

5.2 Model

In this section we review the basics of the honeycomb-Hubbard model and derive the noninteracting Floquet Green's functions in circularly polarized fields.

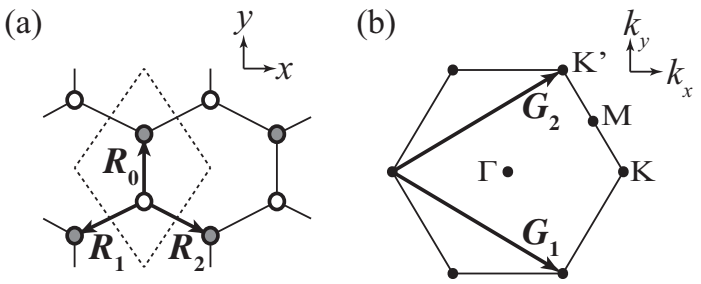

Figure 5-4: (a) Honeycomb lattice in real space. Open and shaded circles represent atoms in A- and B-sublattices, respectively. $\boldsymbol{R}_{0,1,2}$ are vectors to the nearest-neighboring sites. (b) The reciprocal lattice space. $\boldsymbol{G}_{1,2} = (2\pi/3\sqrt{3}a, \mp 2\pi/3a)$ is the reciprocal lattice vectors: .

5.2.1 Honeycomb-Hubbard model

The tight-binding Hamiltonian for the honeycomb-Hubbard model reads

$$\mathscr{H} = \mathscr{H}_0 + \mathscr{H}_1, \tag{5.6a}$$

$$\mathscr{H}_0 = \sum_{\langle ij\rangle,\sigma} J c^\dagger_{i\sigma} c_{j\sigma}, \tag{5.6b}$$

$$\mathscr{H}_1 = \sum_i U c^\dagger_{i\uparrow} c_{i\uparrow} c^\dagger_{i\downarrow} c_{i\downarrow}, \tag{5.6c}$$

where $\mathscr{H}_0$ is the non-interacting tight-binding Hamiltonian and $\mathscr{H}_1$ is the Hubbard interaction term. The sum in $\mathscr{H}_0$ is over all the nearest-neighbor pairs (i,j) in the honeycomb lattice, depicted in Fig. 5-4. The directions to the nearest neighbors are given by $\boldsymbol{R}_0 = {}^t(0,a)$, $\boldsymbol{R}_1 = {}^t(-\sqrt{3}a/2, -a/2)$ and $\boldsymbol{R}_2 = {}^t(\sqrt{3}a/2, -a/2)$, where a is the distance of the nearest-neighbor sites (hereafter we take a as the unit of length: $a = 1$). By the standard tight-binding model calculation, we obtain the noninteracting Hamiltonian $\mathscr{H}_0$ in the $\boldsymbol{k}$-space as

$$\mathscr{H}_0 = \sum_{\boldsymbol{k}\sigma} \psi^\dagger_{\boldsymbol{k}\sigma} H_{0\boldsymbol{k}} \psi_{\boldsymbol{k}\sigma}, \tag{5.7a}$$

$$\psi_{\boldsymbol{k}\sigma} = {}^t\begin{pmatrix} c_{A\boldsymbol{k}\sigma} & c_{B\boldsymbol{k}\sigma} \end{pmatrix}, \tag{5.7b}$$

$$H_{0\boldsymbol{k}} = \sum_{j=0,1,2} \begin{pmatrix} 0 & e^{-i\boldsymbol{k}\cdot\boldsymbol{R}_j} \\ e^{i\boldsymbol{k}\cdot\boldsymbol{R}_j} & 0 \end{pmatrix} \tag{5.7c}$$

$$= \begin{pmatrix} 0 & e^{-ik_y} + 2\cos\left(\frac{\sqrt{3}}{2}k_x\right) e^{ik_y/2} \\ e^{ik_y} + 2\cos\left(\frac{\sqrt{3}}{2}k_x\right) e^{-ik_y/2} & 0 \end{pmatrix}. \tag{5.7d}$$

The eigenvalues of $H_{0\boldsymbol{k}}$, $\omega = \pm\epsilon_{\boldsymbol{k}}$, give the noninteracting band structure of the honeycomb lattice, where

$$\epsilon_{\boldsymbol{k}} = \sqrt{1 + 4\cos^2\left(\frac{\sqrt{3}k_x}{2}\right) + 4\cos\left(\frac{\sqrt{3}k_x}{2}\right)\cos\left(\frac{3k_y}{2}\right)}. \tag{5.8}$$

5.2.2 Honeycomb-Hubbard model in circulary polarized electric fields

We then consider the circularly polarized electric field $\boldsymbol{E}(t) = -\partial_t \boldsymbol{A}(t)$, given by the vector potential

$$\boldsymbol{A}(t) = {}^t(A\cos\Omega t, A\sin\Omega t), \tag{5.9}$$

where Ω and A are the frequency and the amplitude of the vector potential. The intensity of the electric field is $E = |A\Omega|$. The external field can be included as the Peierls substitution: $\boldsymbol{k} \to \boldsymbol{k} + \boldsymbol{A}(t)$. Due to this substitution, each component of the noninteracting Hamiltonian is transformed as

$$e^{-i\boldsymbol{k}\cdot\boldsymbol{R}_j} \to e^{-i\boldsymbol{k}\cdot\boldsymbol{R}_j} e^{-i\boldsymbol{A}(t)\cdot\boldsymbol{R}_j} = e^{-i\boldsymbol{k}\cdot\boldsymbol{R}_j} e^{-iA\sin(\Omega t - 2\pi j/3)}, \tag{5.10}$$

where we have used $\boldsymbol{R}_j = {}^t(\cos\phi_j, \sin\phi_j)$ with $\phi_j = \pi/2 + 2\pi j/3 (j = 0,1,2)$ representing the angle between x-axis and $\boldsymbol{R}_j$. Therefore, the time-dependent Hamiltonian reads

$$\mathscr{H}(t) = \mathscr{H}_0(t) + \mathscr{H}_1, \tag{5.11}$$

$$\mathscr{H}_0(t) = \sum_{\boldsymbol{k},\sigma} \psi^\dagger_{\boldsymbol{k}\sigma} H_{0,\boldsymbol{k}+\boldsymbol{A}(t)} \psi_{\boldsymbol{k},\sigma}, \tag{5.12}$$

$$H_{0,\boldsymbol{k}+\boldsymbol{A}(t)} = \sum_{j=0,1,2} \begin{pmatrix} 0 & e^{-i\boldsymbol{k}\cdot\boldsymbol{R}_j} e^{-iA\sin(\Omega t - 2\pi j/3)} \\ e^{i\boldsymbol{k}\cdot\boldsymbol{R}_j} e^{iA\sin(\Omega t - 2\pi j/3)} & 0 \end{pmatrix}. \tag{5.13}$$

In order to study steady states of this Hamiltonian, we need to solve the Dyson equation for Floquet-Green's functions, where the Floquet matrix element,

$$\hat{H}_{mn}(\boldsymbol{k}) = \int_0^T \frac{dt}{T} H_{0,\boldsymbol{k}+\boldsymbol{A}(t)} e^{i(m-n)\Omega t}, \tag{5.14}$$

plays an important role, with T the period of the field $T = 2\pi/\Omega$. Each component of $H_{0,\boldsymbol{k}+\boldsymbol{A}(t)}$ in Eq. (5.13) is transformed as

$$\begin{aligned} &\int_0^T \frac{dt}{T} e^{-i\boldsymbol{k}\cdot\boldsymbol{R}_j} e^{\pm iA\sin(\Omega t - 2\pi j/3)} e^{i(m-n)\Omega t} \\ &= e^{i(m-n)\cdot 2\pi j/3} e^{-i\boldsymbol{k}\cdot\boldsymbol{R}_j} \int_0^T \frac{dt}{T} e^{\pm iA\sin\Omega t} e^{i(m-n)\Omega t} \\ &= e^{i(m-n)\cdot 2\pi j/3} e^{-i\boldsymbol{k}\cdot\boldsymbol{R}_j} J_{\mp(m-n)}(A), \end{aligned}$$

where $J_n(A)$ is the Bessel function. Then the Floquet matrix element of the noninteracting Hamiltonian $\hat{H}_{mn}$ reads

$$\hat{H}_{mn}(\boldsymbol{k}) = \sum_{j=0,1,2} \begin{pmatrix} 0 & J_{-(m-n)}(A) e^{-i\boldsymbol{k}\cdot\boldsymbol{R}_j} \\ J_{m-n}(A) e^{i\boldsymbol{k}\cdot\boldsymbol{R}_j} & 0 \end{pmatrix} e^{2\pi i(m-n)j/3}. \tag{5.15}$$

With the Floquet matrix element, the Dyson equation for Floquet-Green's functions reads (see Chap. 5)

$$\begin{pmatrix} \hat{G}^R_{\boldsymbol{k}} & \hat{G}^K_{\boldsymbol{k}} \\ 0 & \hat{G}^A_{\boldsymbol{k}} \end{pmatrix}(\omega) = \begin{pmatrix} \omega\hat{1} + \hat{\Omega} - \hat{H}(\boldsymbol{k}) & 0 \\ 0 & \omega\hat{1} + \hat{\Omega} - \hat{H}(\boldsymbol{k}) \end{pmatrix} - \begin{pmatrix} \hat{\Sigma}^R & \hat{\Sigma}^K \\ 0 & \hat{\Sigma}^A \end{pmatrix}(\omega) - \begin{pmatrix} \hat{\Sigma}^R_{\mathrm{diss}} & \hat{\Sigma}^K_{\mathrm{diss}} \\ 0 & \hat{\Sigma}^A_{\mathrm{diss}} \end{pmatrix}(\omega), \tag{5.16a}$$

where

$$\hat{\Omega}_{\alpha\beta;mn} = n\Omega\delta_{\alpha\beta}\delta_{mn}, \tag{5.16b}$$

$$\hat{\Sigma}^{R,A}_{\mathrm{diss}}(\omega) = \mp i\Gamma\delta_{\alpha\beta}\delta_{mn}, \tag{5.16c}$$

$$\hat{\Sigma}^{K}_{\mathrm{diss}}(\omega) = -2i\tanh\left(\frac{\omega+n\Omega}{2T}\right)\delta_{\alpha\beta}\delta_{mn}, \quad \alpha,\beta = A,B, \quad m,n\in\mathbb{Z}. \tag{5.16d}$$

5.3 Result and discussions

In this section, using the two-band Floquet-DMFT formalism for honeycomb-Hubbard model in the previous section, we study the properties of steady states in the honeycomb-Hubbard model in circularly polarized fields. We set the Fermi level at the Dirac point (half filling) throughout this chapter. We show our results in three parts: equilibrium (no external fields), nonequilibrium steady states in ac-fields with off-resonant, and those for resonant frequencies.

5.3.1 Equilibrium case

First we show the results for the equilibrium case, where the field strength is set to zero ($A = 0$). Since we have attached heat baths as dissipative environments, non-analytic behaviors at phase boundaries will be rounded and thus phase transitions appear as a crossover. At sufficiently small bath strength Γ the observables show anomalous behavior in the vicinity of the transition line.

In Fig. 5-5, we show the transition in the density of states $A(\omega)$ and the occupation density $N(\omega)$ defined in Eq. (4.11) as U is changed. For $0 \le U \le 10$ we observe a V-shaped dip around the Fermi level, which is the manifestation of the quasiparticle with the Dirac dispersion. Thus the system is semimetallic in this regime, having quasiparticles with Dirac dispersion around the Fermi level. The quasiparticle weight Z and the renormalized Fermi velocity $\tilde{v}_F$ are given respectively as

$$Z = \left(1 - \frac{\partial\Sigma^R}{\partial\omega}\right)^{-1}_{\omega=0}, \tag{5.17}$$

$$\tilde{v}_F = Z v_F. \tag{5.18}$$

For $U \ge 14$, the quasiparticle weight almost vanishes and a broad structure with the lower Hubbard band (LHB) and the upper Hubbard band (UHB) grows around $\omega = \pm U/2$. The critical value U_c, at which the quasiparticle weight vanishes, is therefore situated around $U = 14$.

To estimate the critical strength U_c more qualitatively, we plot the double occupancy,

$$D_{\mathrm{occ}} = \langle n_\uparrow n_\downarrow \rangle, \tag{5.19}$$

the quasiparticle weight Z, and dc-conductivity σ_{xx} against U for various values of bath coupling strength Γ. As we have shown in Fig. 5-3(b), the quasiparticle weight Z can be a good indicator for SMIT from the standpoint of the Fermi-liquid picture [97]. From the

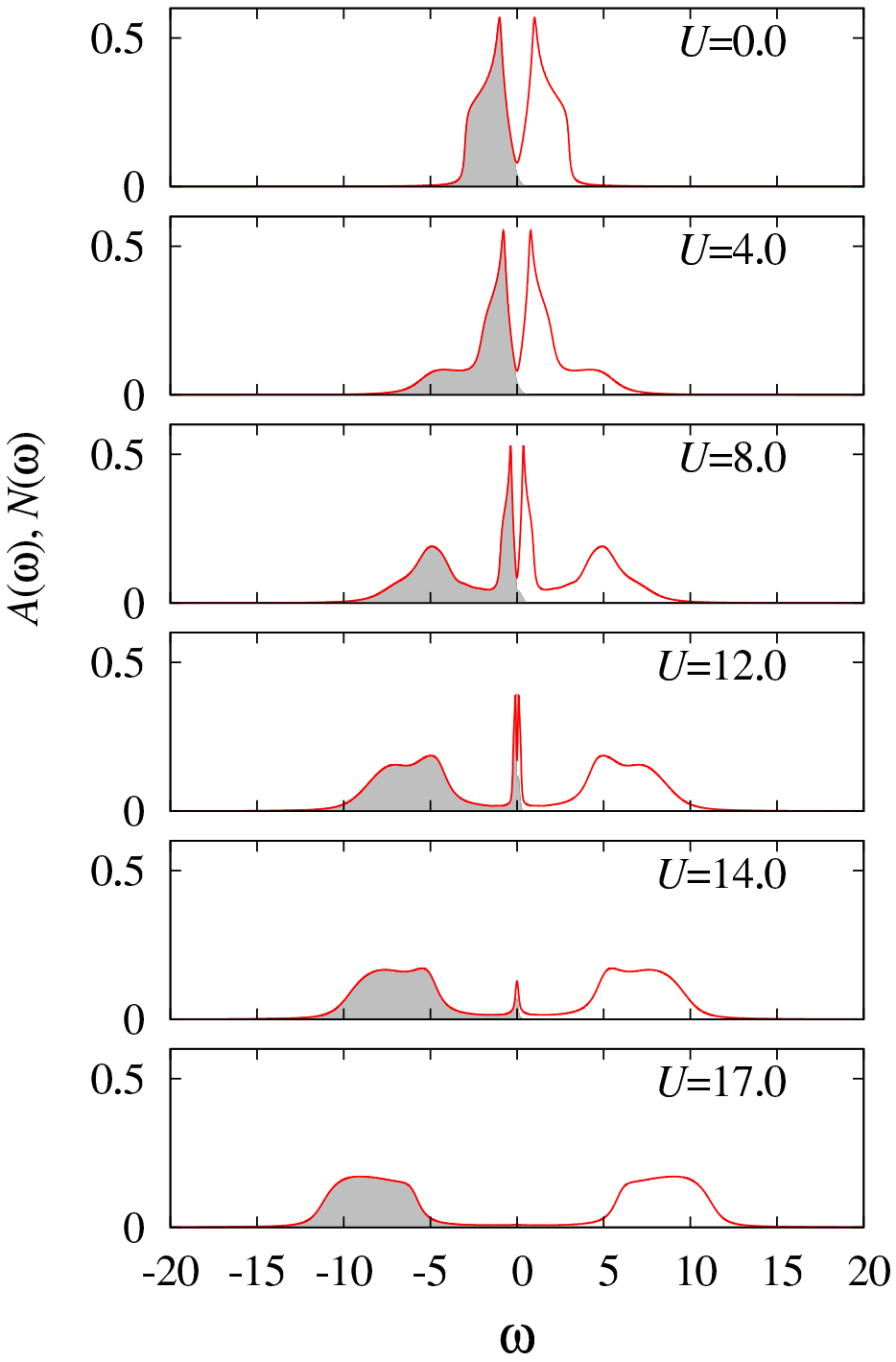

Figure 5-5: Equilibrium density of states $A(\omega)$ for the honeycomb-Hubbard model in equilibrium, obtained by solving the Dyson equation (5.16a) with $A = 0$. The energy ω is measured from the Fermi level. The electron occupation density $N(\omega)$ is depicted as the shaded regions. Parameters are chosen as $J = 1, T = 0.1$ and $\Gamma = 0.06$ and U increased from 0 to 17.

standpoint of Mott physics, D_{occ} can be a good indicator, since it shows the probability for

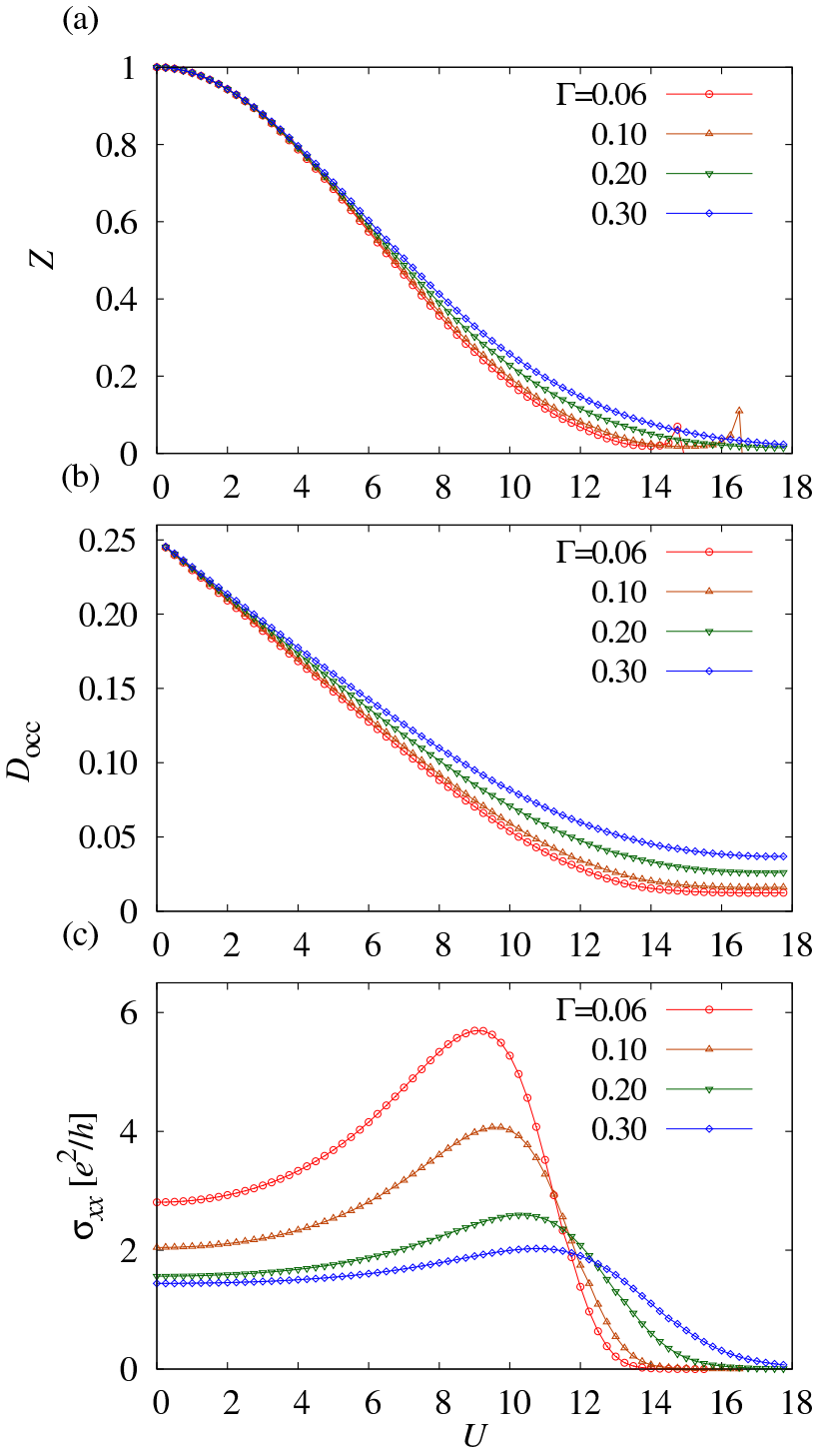

Figure 5-6: (a) Quasiparticle weight Z, (b) double occupancy D_{occ}, and (c) dc-conductivity $\sigma_{xx}(\omega = 0)$ against U for the bath coupling strength Γ increased from 0.06 to 0.3. Parameters are chosen as $J = 1$ and $T = 0.1$.

finding two electrons on the same site, which drops to zero in the Mott regime. Besides,

optical conductivity $\sigma_{xx}(\omega)$ is an important quantity from the experimental point of view. A finite dc-conductivity $\sigma_{xx}(\omega = 0)$ implies that there are electronic states around the Fermi level and therefore it indicates a metallic nature of the system.

In Fig. 5-6 we show quasiparticle weight Z, double occupancy $D_{\rm occ}$, and the longitudinal dc-conductivity σ_{xx} for various values of bath coupling Γ. Z and $D_{\rm occ}$ approach to zero as U becomes larger, but converge to some nonzero values. This is due to the heat-bath attached to the system. In fact, when we decrease the coupling constant Γ as in Fig. 5-6(a)(b), then Z and $D_{\rm occ}$ converge closer to zero in the large U limit.

In Fig. 5-6(c) we also show σ_{xx} for some bath coupling strength Γ. As Γ becomes smaller, the dc-conductivity σ_{xx} drops to zero more sharply at the critical point. By observing the intersection point of the $U - \sigma_{xx}$ curves for $\Gamma = 0.06$ and $\Gamma = 0.1$ we estimate the critical value $U_c \simeq 12$.

Note that the quasiparticle weight Z has some structures in the insulating region. This is because the Fermi-liquid picture breaks down in the Mott insulating regime $U > U_c$, where the quasiparticle weight calculated by Eq. (5.17) becomes ill-defined.

Let us compare the obtained critical value with the previous studies. Jafari *et al*. obtained $U_c = 13.3$ using DMFT with iterated perturbation theory as the impurity solver at $T = 0$ [97]. A slight difference from the present critical value can be understood as a finite-temperature effect[1]. Technically, the critical value U_c depends on the impurity solver. In fact, Minh-Tien *et al.* used DMFT with QMC impurity solver at $T = 0.1$, obtaining $U_c = 8.2$ [107]. It is empirically known that the iterative perturbation theory overestimates the critical value [107].

5.3.2 Nonequilibrium steady states in off-resonant fields

Next, we apply circularly polarized lights with *off-resonant photon energies* $\Omega \gg W$, where $W = 6J$ is the band width. In this regime, the distribution function stays monotonic over the bandwidth (Fig. 5-7). Therefore it is expected that realized steady states are well described by the time-averaged effective Hamiltonian.

It turns out that the system exhibits two types of photo-induced phase transitions: semimetal-insulator and topological phase transitions. In the following, we study the electronic structures and transport properties to investigate the nature of the steady states and obtain the phase diagram. Finally, we discuss the resulting phase diagram by mapping our system to a time-independent effective model, so that the connection between the honeycomb lattice in off-resonant fields and an effective model of topological insulators are clarified.

Semimetal-insulator transition

In Fig. 5-8 the density of states $A(\omega)$, the occupation density $N(\omega)$ and the effective distribution function $f(\omega) = N(\omega)/A(\omega)$ are shown for various values of external field strength A. We set $U = 2$ and therefore the system is semimetal in the absence of external fields. The

[1] One might expect that U_c increases as the temperature rises, but DMFT calculation show that U_c decreases as the temperature increases in a square lattice [56], a honeycomb lattice [107].

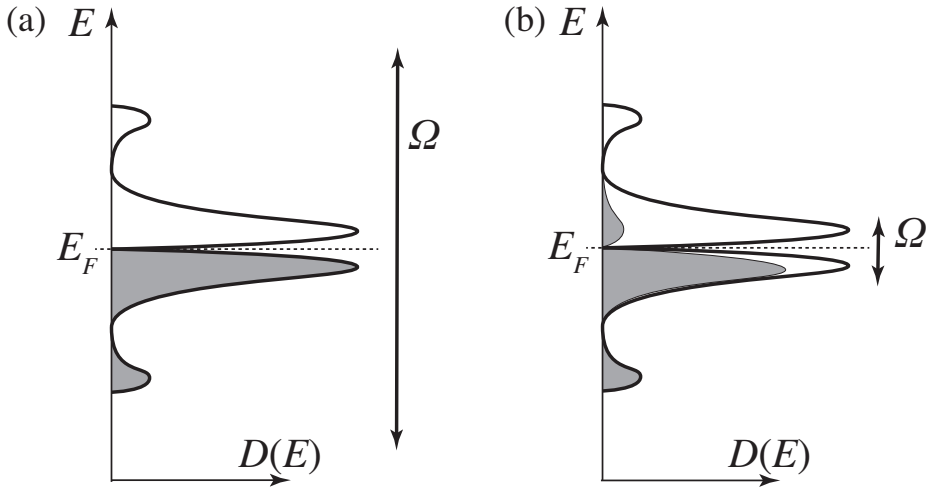

Figure 5-7: Schematic description of the system in off-resonant (a) and resonant (b) electric fields, where Ω is the frequency of the external fields. Thick lines and gray shaded region show the density of states and the distribution, respectively.

problem is how the semimetallic state is disturbed by circularly polarized fields, and what is the character of the nonequilibrium steady states.

The distribution functions stay monotonic over the bandwidth in Fig. 5-8, as we have expected in the off-resonant condition. Examining the density of states in Fig. 5-8, we find that as the field strength increases, the system undergoes a phase transition which looks rather similar to the semimetal-to-insulator transition for increasing U. The dip structure around the Fermi level vanishes as A increases, and UHB and LHB grow around $\omega = U/2$.

In order to show the physical properties of the steady states, we plot the double occupancy and dc-conductivities $\sigma_{ab}(\omega = 0)(a, b = x, y)$ against the field strength A in Fig. 5-9. It should be noted that the tensor $\sigma_{ab}(\omega)$ has a symmetry,

$$\sigma_{xx}(\omega) = \sigma_{yy}(\omega), \quad \sigma_{xy}(\omega) = -\sigma_{yx}(\omega), \tag{5.20}$$

due to the discrete rotational symmetry of the honeycomb-lattice in circularly polarized fields.[2]

Longitudinal conductivities $(\sigma_{xx}, \sigma_{yy})$ show that the steady state is insulating in regions $2.1 < A < 2.8$ or $5.2 < A < 6$. The double occupancy D_{occ} has minima in the insulating regions which implies the Mott-insulating properties are strongly enhanced in the insulating region. We clearly observe SMIT at these critical values $A_c \simeq 2.1, 2, 8, 5.2$. This is quite similar to

[2] One can prove Eq. (5.20) as follows. Let R be the unitary operation of rotating the system by angle $\phi = 2\pi/3$ around the z-axis. We also consider the translated coordinate system S', which is rotated by R from the original coordinate S. The system is equivalent in both coordinate. The external field is also equivalent, with only the difference of time translation $t \to t + (2\pi/3)/\Omega$. The time shift by a constant does nothing to the steady states. Therefore, the realized steady states should have the rotational symmetry given by R. This means that the 2×2 tensor $\sigma(\omega) = \{\sigma_{ab}\}$ should satisfy $\sigma(\omega) = R^{-1}\sigma(\omega)R = R\sigma(\omega)R^{-1}$ with $R = \begin{pmatrix} \cos\phi & -\sin\phi \\ \sin\phi & \cos\phi \end{pmatrix}$. Simple algebra with this relation leads to Eq. (5.20). This argument holds for any $\phi \neq n\pi (n \in \mathbb{Z})$. Therefore Eq. (5.20) also holds for a square lattices, and a triangle lattice, and so on.

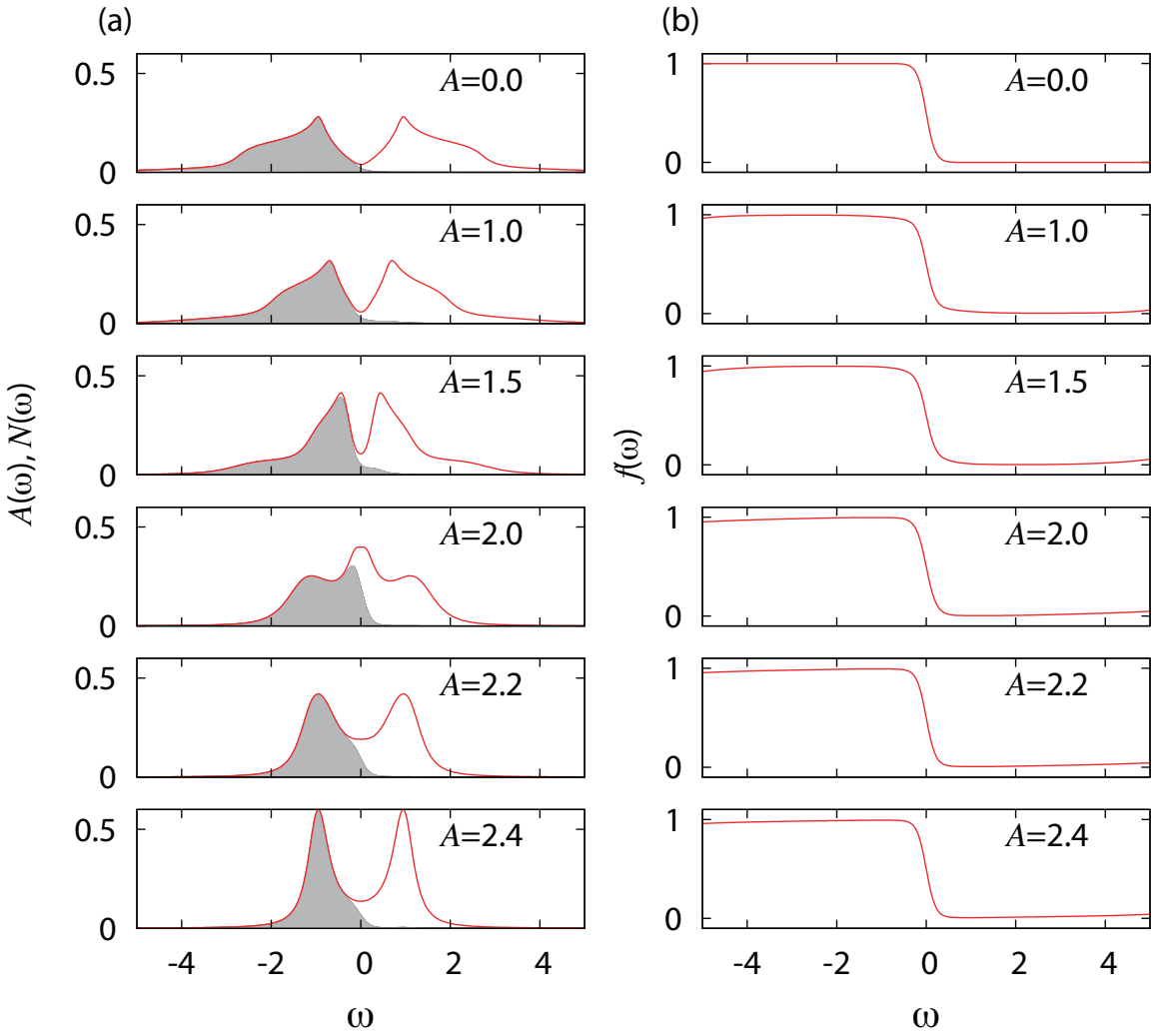

Figure 5-8: Density of states $A(\omega)$ with shading representing occupied states $N(\omega)$ (left panel), and the effective distribution function $f(\omega)$ (right panel) for various field strength A increased from 0.0 to 2.4 in the off-resonant regime $\Omega = 10$. Parameters used here are $J = 1, U = 2, \Gamma = 0.1$ and $T = 0.1$.

usual SMIT, with an essential difference that the transition is induced by the external field A, not by the interaction U.

Thus the results show that the external fields induce the Mott insulator phase. This may seem surprising, since external fields usually tend to excite carriers. However, this phenomenon is clearly understood in terms of the effective Hamiltonian where external fields effectively change the hopping parameters [29, 34].

Since the nonequilibrium distribution function is monotonic as shown in Fig. 5-8, the phase transition should be caused purely by a property of the effective Hamiltonian. As shown in the Floquet Hamiltonian (5.15), an external field gives the factor $J_0(A)$ to the kinetic energy part of the Floquet Hamiltonian and causes effective shrinking of the bandwidth W. The reason for this shrinkage is understood by time average over the Bloch oscillation

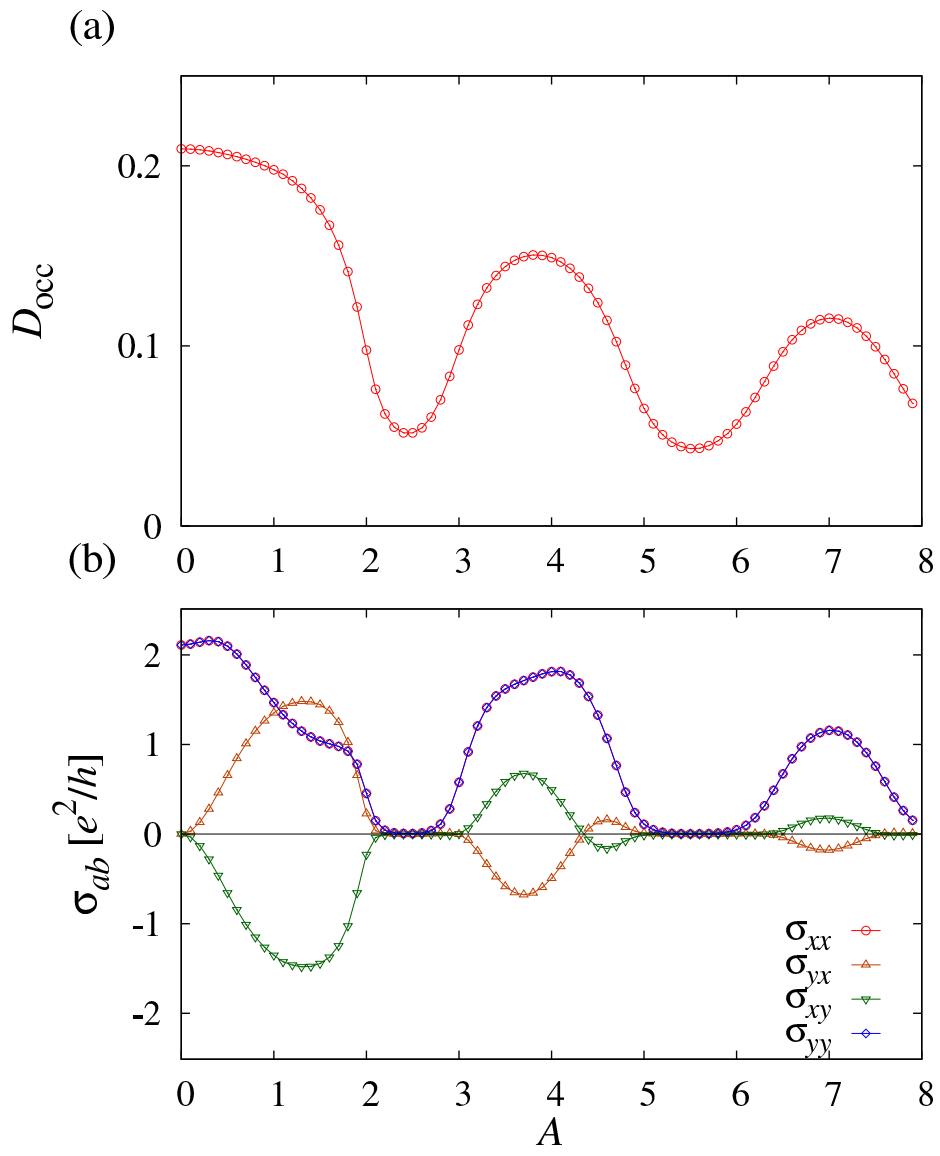

Figure 5-9: (a) The double occupancy $D_{\rm occ}$ and (b) optical conductivities ($\sigma_{xx}, \sigma_{yx}, \sigma_{xy}$ and σ_{yy}) against the field strength A in an off-resonant regime $\Omega = 10$. Parameters used here are $J = 1, U = 2, \Gamma = 0.1$ and $T = 0.1$.

[68]. Therefore the electron correlation strength U/W is increased as $U/(W|J_0(A)|)$. Hence, the Mott transition induced by off-resonant external fields may be interpreted as an analog of the bandwidth-controlled Mott transition [5].

If the field induced SMIT is consistent with the bandwidth-controlled Mott transition, the critical field strength A_c for a fixed U is given by the relation $U/(W|J_0(A_c)|) = U_c/W$, i.e.,

$$|J_0(A_c)| = \frac{U}{U_c}. \tag{5.21}$$

For the parameters used in Fig. 5-9, Eq. (5.21) gives

$$A_c = J_0^{-1}(\pm U/U_c) \simeq J_0^{-1}(\pm 1/6) \simeq 2.10, 2.75, 5.05, 6.05, \cdots .$$

These critical values are consistent with those obtained here from D_{occ} and σ_{xx} in Fig. 5-9.

Topological-semimetal transition

We further investigate the properties of semimetallic regions. In this region, the circularly polarized light opens a topological gap at K- and K'-points and gives nontrivial Berry curvatures and the Hall conductivity at least for noninteracting case as shown by Oka, *et al.* [29]. Therefore it is interesting to ask whether the topological property is preserved, or even other topological properties emerge, when the interaction is switched on. As shown in Chapter 3, the Hall conductivity is a good indicator for nontrivial Berry curvatures in the Floquet Hamiltonian.

Let us again examine Fig. 5-9(b), the dc-conductivity against field strength A for $U = 2$. Firstly, the Hall conductivity σ_{xy} is nonzero only in the region where the longitudinal conductivity σ_{xx} is finite. Secondly, σ_{xy} and σ_{xx} drop to zero *not simultaneously*: there seem to be two-stage phase transitions with three phases: (1) topological phase: $\sigma_{xy} \neq 0$, (2) normal metal phase: $\sigma_{xx} \neq 0, \sigma_{xy} = 0$ and (3) Mott-insulating phase: $\sigma_{xx} = \sigma_{xy} = 0$.

To further investigate the three regions, we calculate the $\boldsymbol{k}$-resolved Hall conductivity $g(\boldsymbol{k})$ over the BZ, given by

$$g(\boldsymbol{k}) = \frac{1}{2}\lim_{\omega\to 0}\int_{-\Omega/2}^{\Omega/2}\frac{d\nu}{2\pi}\mathrm{tr}\,\frac{\hat{v}^y_{\boldsymbol{k}}\hat{G}^{\mathrm{R}}_{\boldsymbol{k}}(\nu)\hat{v}^x_{\boldsymbol{k}}\hat{G}^{<}_{\boldsymbol{k}}(\nu-\omega) + \hat{v}^y_{\boldsymbol{k}}\hat{G}^{<}_{\boldsymbol{k}}(\nu)\hat{v}^x_{\boldsymbol{k}}\hat{G}^{\mathrm{A}}_{\boldsymbol{k}}(\nu-\omega)}{\omega} - (x\leftrightarrow y). \tag{5.22}$$

The $\boldsymbol{k}$-resolved Hall conductivity $g(\boldsymbol{k})$ is connected to the Hall conductivity via a relation,

$$\sigma_{yx} = \frac{N_s}{\Omega_{\mathrm{cell}}N_k}\sum_{\boldsymbol{k}} g(\boldsymbol{k})d\boldsymbol{k}, \tag{5.23}$$

with $N_s = 2$ the spin degeneracy, $\Omega_{\mathrm{cell}} = 3\sqrt{3}/2$ the volume of the unit cell, and N_k the number of $\boldsymbol{k}$-points in the Brillouin zone. As we have shown in Chapter 3, in the noninteracting case $g(\boldsymbol{k})$ is expressed as

$$g(\boldsymbol{k}) = \sum_m \mathscr{B}_{m\boldsymbol{k}} f_{m\boldsymbol{k}}, \tag{5.24}$$

where $\mathscr{B}_{m\boldsymbol{k}}$ is the Berry curvature and $f_{m\boldsymbol{k}}$ is the distribution function for the Floquet state labeled by the Floquet index m and the Bloch momentum $\boldsymbol{k}$. It is straightforward to show that $g(\boldsymbol{k})$ satisfies

$$g(\boldsymbol{k}) = g(R\boldsymbol{k}), \quad R = \begin{pmatrix} \cos\frac{2\pi}{3} & -\sin\frac{2\pi}{3} \\ \sin\frac{2\pi}{3} & \cos\frac{2\pi}{3} \end{pmatrix} \tag{5.25}$$

and therefore $g(\boldsymbol{k})$ has the same C_3 symmetry as the Berry curvature [29].

In Fig. 5-10, we plot the spectral function and the $\boldsymbol{k}$-resolved Hall conductivity. From this we can see that the main contribution to the Hall conductivity is the Berry curvature around the K- and K'-points for $0 < A < 2.4$. The contribution vanishes at $A \simeq 2.4$, a zero of $J_0(A)$, where the diagonal elements of the current matrix $\hat{v}^{x,y}$ vanish. In Fig. 5-10(a) the $\boldsymbol{k}$-resolved

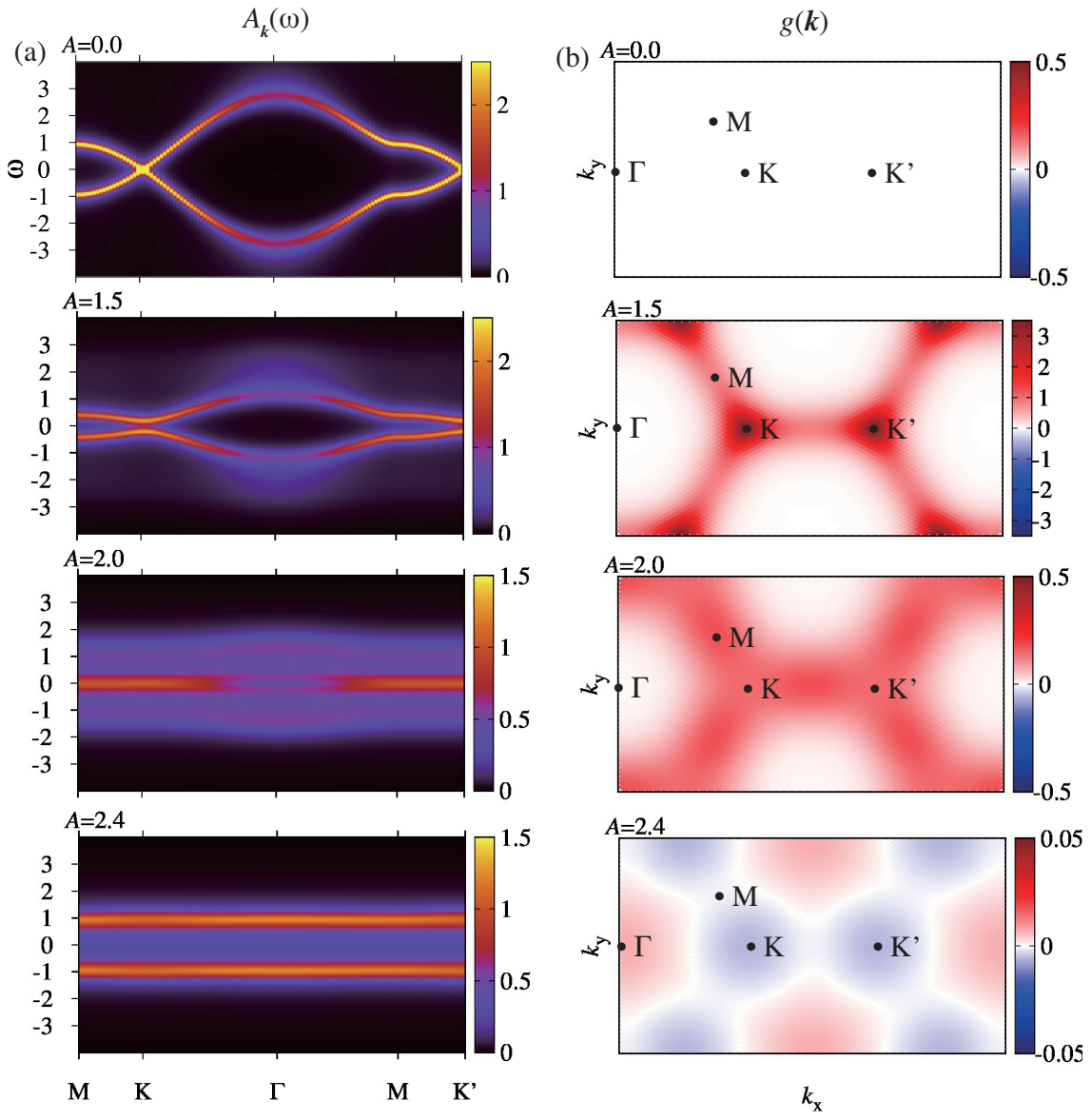

Figure 5-10: (a) The $\boldsymbol{k}$-resolved spectral function $A_{\boldsymbol{k}}(\omega)$ and (b) the $\boldsymbol{k}$-resolved Hall conductivity $g(\boldsymbol{k})$ for various values of the field strength A in the off-resonant regime $\Omega = 10$. Parameters used here are $J = 1, U = 2, \Gamma = 0.1$ and $T = 0.1$.

spectral function,

$$A_{\boldsymbol{k}}(\omega) = -\frac{1}{\pi}\mathrm{Im}\int_0^T \frac{dt_{\mathrm{av}}}{T}\int_{-\infty}^{\infty} dt_{\mathrm{rel}}\, e^{i\omega t_{\mathrm{rel}}}\mathrm{tr}\, G_{\boldsymbol{k}}\left(t_{\mathrm{av},+}\frac{t_{\mathrm{rel}}}{2}, t_{\mathrm{av},-}\frac{t_{\mathrm{rel}}}{2}\right), \tag{5.26}$$

shows that a band gap opens at the Dirac points for $A = 1.5$. It clearly shows that the system becomes insulating due to the external field. For $A = 2.0$ the gap almost closes and the system becomes semimetallic. For $A = 2.4$ the system is a Mott insulator, with quasiparticle absent around the Fermi level while UHB and LHB develop. This shows that the system has a

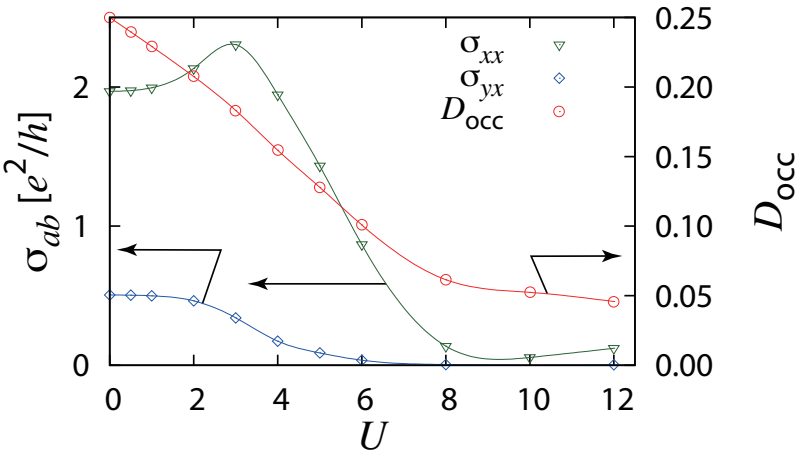

Figure 5-11: The double occupancy $D_{\rm occ}$, the longitudinal dc-conductivity σ_{xx} and the Hall conductivity σ_{xy} against U for $A = 0.4$ in the off-resonant regime $\Omega = 10$. Parameters used here are $J = 1, \Gamma = 0.1$ and $T = 0.1$.

two-stage phase transition.

In order to see the effect of U for the topological properties, we fix the field strength $A = 0.4$ at which the topological gap opens at $U = 0$, and increase the interaction U until the system enters the Mott-insulating region. In Fig. 5-11. we plot the dc-conductivities σ_{xx}, σ_{xy} and the double occupancy $D_{\rm occ}$. An important observation is that there are two critical values of U. At $U = U_{\rm c1} \simeq 7.0$ the dc-Hall conductivity σ_{xy} vanishes, followed by $U = U_{\rm c2} \simeq 9.0$, where the longitudinal conductivity σ_{xx} goes to zero and the system enters an insulating phase.

Let us discuss how the Hall conductivity σ_{xy} is quantized. In Fig. 5-12 we plot σ_{xx} and σ_{xy} against A for various values of U. In particular, in the noninteracting case we set a weakly coupled low temperature heat-bath with $T = \Gamma = 0.02$ so that the effect of the dissipation is reduced. For the noninteracting case, σ_{xy} reaches the quantized value $\pm 2e^2/h$ (where the factor 2 is the spin degeneracy). For rather strongly coupled bath with $T = \Gamma = 0.1$, the Hall conductivity decreases from the quantized value. This fact indicates that one should set the temperature sufficiently low, compared to the topological gap at the K-point, for an exact quantization of σ_{xy}. In fact, the topological gap for $A = 1.5$ is estimated as ~ 0.1 (see the band structure in Fig. 5-10) and thus $T \ll 0.1$ may be required in this case. As U increases, the Hall conductivity is also suppressed, as we have discussed in Fig. 5-11.

We finally investigate the metallic, insulating, and topological properties in the U-A space. In Fig. 5-13 we plot σ_{xx} (a), $D_{\rm occ}$ (b), and σ_{xy} (c,d) for fixed bath parameters $T = \Gamma = 0.1$, against U and A. In Fig. 5-13(a-c) we also plot the contour $U/U_c = |J_0(A)|$ (see Eq. (5.21)) with $U_c = 12$, above which the system is effectively regarded as a (bandwidth-controlled) Mott insulator. In fact, $D_{\rm occ}$ and σ_{xx} have interesting robe structures and have vanishingly small values above the contour, indicating that the system is indeed insulating above the contour.

The behavior of the Hall conductivity is more interesting. Below the metal-insulator boundary, the Hall conductivity changes sign around special values of the field strength $A = 3.0, 4.4, 6.4, 7.6, \cdots$ along the U-axis in Fig. 5-13(c) (such sign-change behavior has been

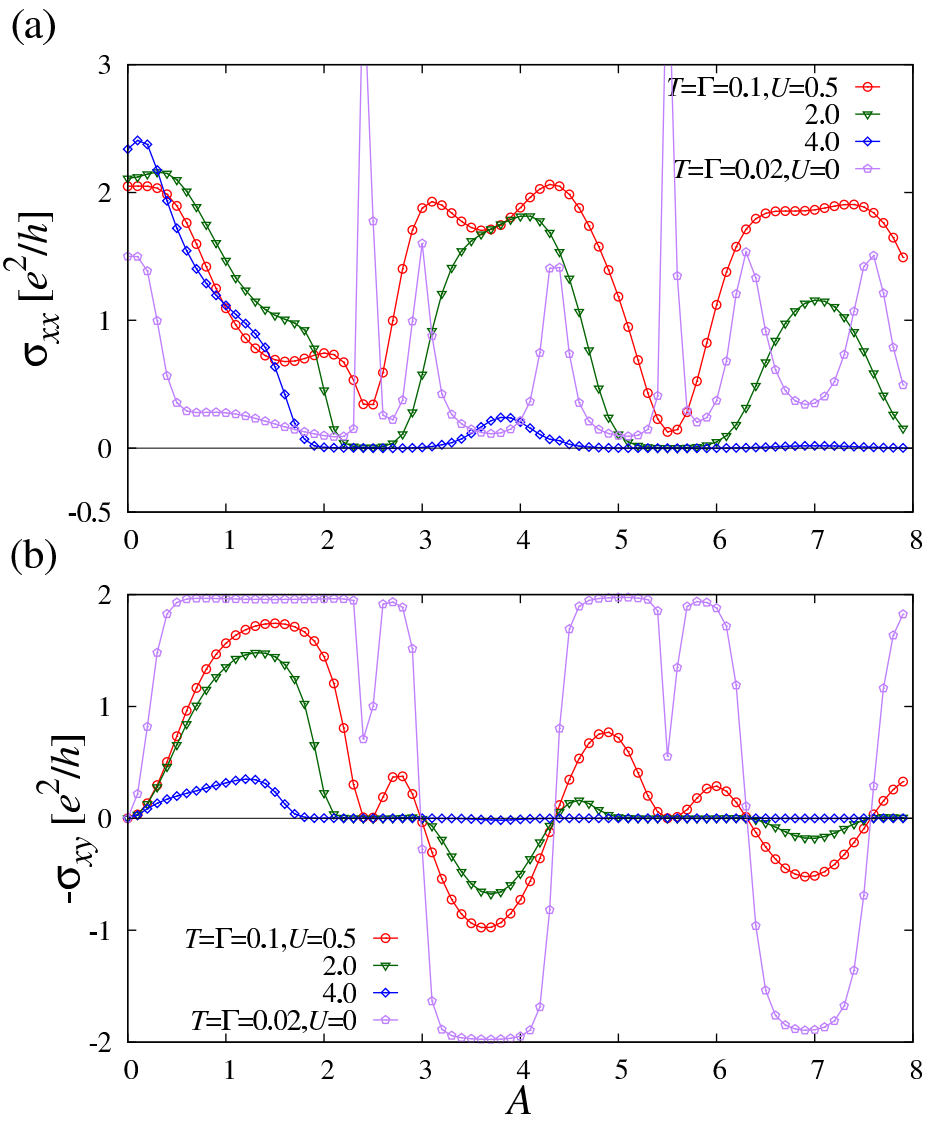

Figure 5-12: The longitudinal dc-conductivity σ_{xx} and the Hall conductivity σ_{xy} against A in the off-resonant regime $\Omega = 10$ for the interaction strength U increased from 1.0 to 4.0 with $\Gamma = T = 0.1$, and in the noninteracting case $U = 0$ with a weakly coupled heat bath with $\Gamma = T = 0.02$.

already seen in Fig. 5-9 and Fig. 5-12). This sign change occurs even in the absence of U. We will further investigate this novel phenomenon in the next section.

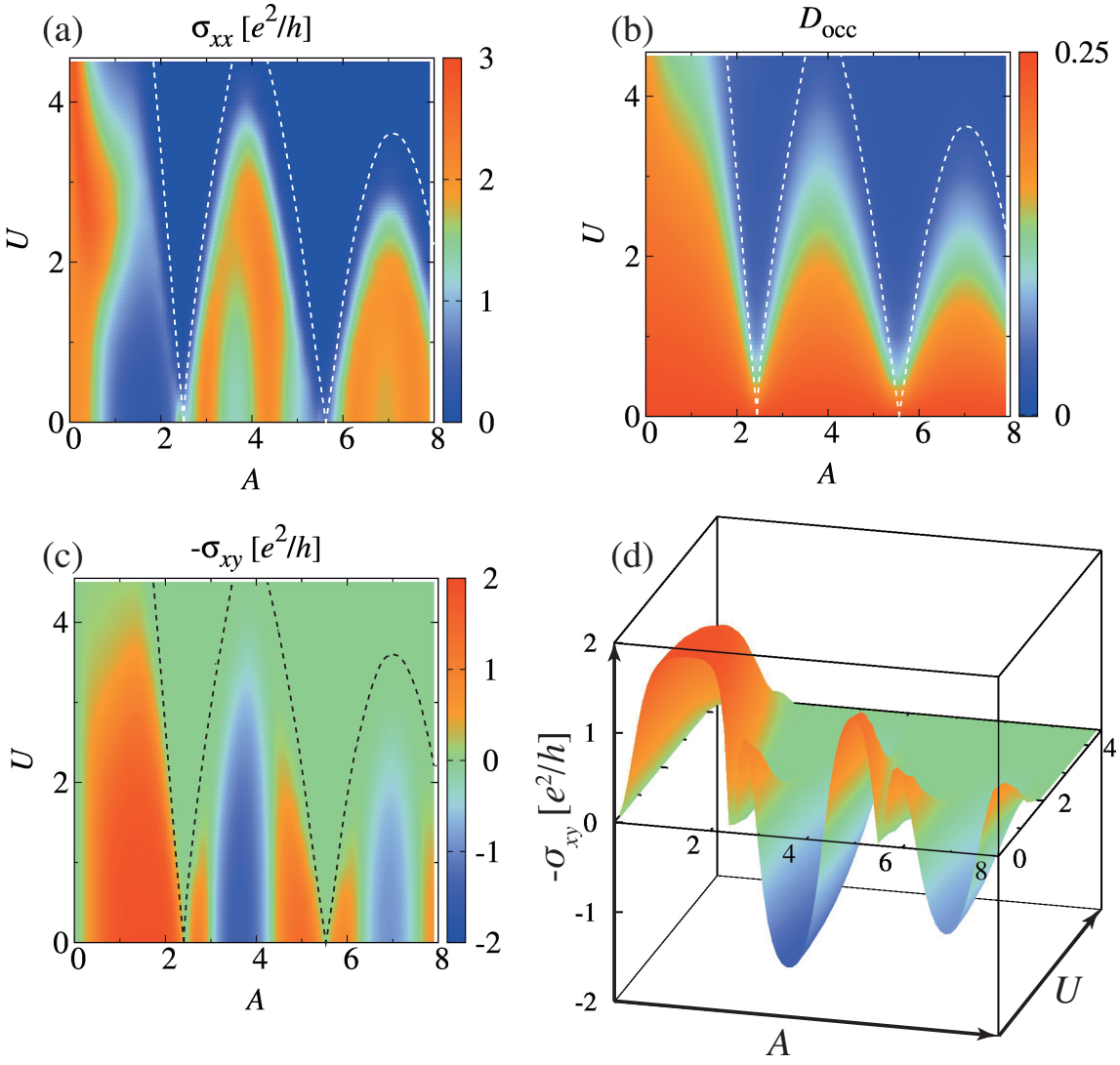

Figure 5-13: Two-dimensional color plots for (a) the longitudinal conductivity σ_{xx}, (b) the double occupancy D_{occ}, and (c) the dc-Hall conductivity σ_{xy} as functions of U and A in the off-resonant regime $\Omega = 10$. An effective critical value of $U = U_c J_0(A)$ (see Eq. (5.21)) is also plotted as dashed lines. (d) A three-dimensional plot for σ_{xy} is also shown so that one can easily see that σ_{xy} reaches its quantized value ± 2 inside the topological phases. Parameters used here are $J = 1, \Gamma = 0.1$ and $T = 0.1$.

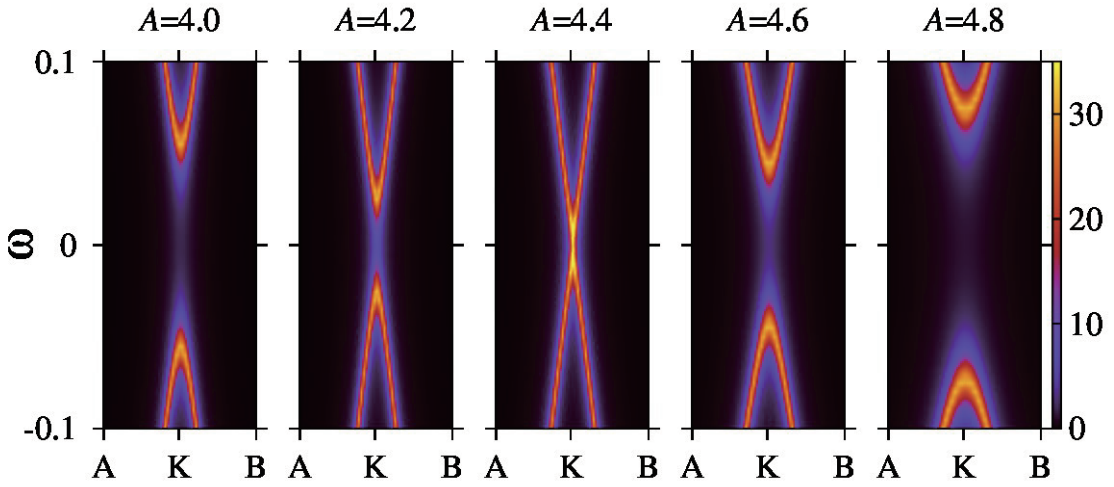

Figure 5-14: Noninteracting ($U = 0$) band structure in the vicinity of the K-point, around a critical value $A = 4.4$, at which the Hall conductivity changes sign (Fig. 5-13). Horizontal axis is a line in the $\boldsymbol{k}$-space given by $(4\pi/3\sqrt{3}, t)$ with $-2\pi/9 \leq t \leq 2\pi/9$. Parameters used here are $U = 0, J = 1, \Gamma = 0.01$ and $T = 0.01$.

Interpretation of the photo-induced topological phase transition in terms of effective Haldane model

In this section, we investigate the origin of the sign-dependence of the Hall conductivity σ_{xy} in Fig. 5-13. First we show in Fig. 5-14 the $\boldsymbol{k}$-resolved spectral functions in the vicinity of the K-point, for $U = 0$ and several values of A around $A \simeq 4.4$. Two bands touch with each other at the Fermi level and separates again as A passes a critical value $A = 4.4$ along the $U = 0$ axis. Since this phase transition is observed in the noninteracting case, this phenomenon should be explained by the topological nature of the noninteracting Floquet Hamiltonian.

The connection between the Dirac electrons in circularly polarized fields and the topological band-insulator is clarified by Kitagawa *et al.* As Kitagawa *et al.* pointed out [106], in the weak-field limit ($A \ll 1$ and $J \ll \Omega$), the tight-binding model on the honeycomb lattice in a circularly polarized light can be mapped to the Haldane model which we introduced in the introduction. Due to this mapping, the photo-induced topological phase transition turns out to be equivalent to the topological phase transitions of the Haldane model, a tight-binding model of a topological insulator.

Although their arguments are limited to the weak-field regime, their method for the construction of the effective Hamiltonian is general enough to analyze the system in strong electric fields. In the following, we reestablish the procedure for constructing the effective Hamiltonian by perturbation theory, only assuming $J/\Omega \ll 1$, and obtain the effective theory for the honeycomb lattice in strong circularly polarized fields.

First we write down the Schrödinger equation for a Floquet elgenstate $|\phi_\alpha\rangle = \{\phi_\alpha^m\}_{m=-\infty}^{\infty}$,

$$(E_\alpha + n\Omega)\phi_\alpha^n = \sum_m \hat{H}_{nm}\phi_\alpha^m, \tag{5.27}$$

where α labels the Floquet eigenstate and ϕ_α^m is the m-th component of the Floquet eigenvector. Note that in the $\Omega \to \infty$ limit we have $\phi_\alpha^{n\neq 0} = 0$ and ϕ_α^0 is an eigenstate of $\hat{H}_{00} = H_0$. Thus $\phi_\alpha^{n\neq 0} \sim O(J/\Omega)$ is evaluated as

$$\phi_\alpha^{n\neq 0} = \sum_m \frac{\hat{\mathscr{H}}_{nm}}{E_\alpha + n\Omega}\phi_\alpha^m = \frac{\hat{H}_{n0}}{n\Omega}\phi_\alpha^0 + o\left(\frac{J}{\Omega}\right). \tag{5.28}$$

Plugging this into the Schrödinger equation for the $n = 0$ component in Eq. (5.27), we have

$$\begin{aligned} E_\alpha\phi_\alpha^0 &= \sum_m \hat{H}_{0m}\phi_\alpha^m \\ &\simeq \left(\hat{H}_{00} + \sum_{m\neq 0}\frac{\hat{H}_{0m}\hat{H}_{m0}}{m\Omega}\right)\phi_\alpha^0 \\ &= \left(H_0 + \sum_{n>0}\frac{[H_{-n}, H_n]}{n\Omega}\right)\phi_\alpha^0. \end{aligned}$$

Thus we obtain a general expression of the effective Hamiltonian up to the order of J/Ω,

$$H_{\text{eff}} = H_0 + \sum_{n>0}\frac{[H_{-n}, H_n]}{n\Omega}. \tag{5.29}$$

Kitagawa, *et al.* [106] constructed the effective Hamiltonian $H_{\text{eff}} = H_0 + [H_{-1}, H_1]/\Omega$ as a perturbation expansion for the field strength A. Our effective Hamiltonian Eq. (5.29) is a natural extension of theirs, and works even for larger A as long as the photon energy satisfies the off-resonant condition $\Omega/J \gg 1$.

Let us assume that our time-dependent Hamiltonian has the form

$$\mathscr{H}(t) = \sum_{ij} J_{ij}(t)c_i^\dagger c_j, \quad J_{ij}(t)^* = J_{ji}(t) \tag{5.30}$$

with $J_{ij}(t+T) = J_{ij}(t)$. This expression is general enough within our interest. In fact, the tight-binding model in electric fields are given by substituting

$$J_{ij}(t) = J_{ij}\exp\left(-i\int_{\boldsymbol{R}_j}^{\boldsymbol{R}_i}\boldsymbol{A}(t)\cdot d\boldsymbol{r}\right). \tag{5.31}$$

The n-th Floquet component of the Hamiltonian reads

$$\mathscr{H}_n = \sum_{ij} J_{ij}^n c_i^\dagger c_j, \quad J_{ij}^n = \int_0^T \frac{dt}{T} J_{ij}(t)e^{in\Omega t} = (J_{ji}^{-n})^*. \tag{5.32}$$

Using the Fermionic commutation relation $\{c_i, c_j^\dagger\} = \delta_{ij}$, we can calculate the commutator in

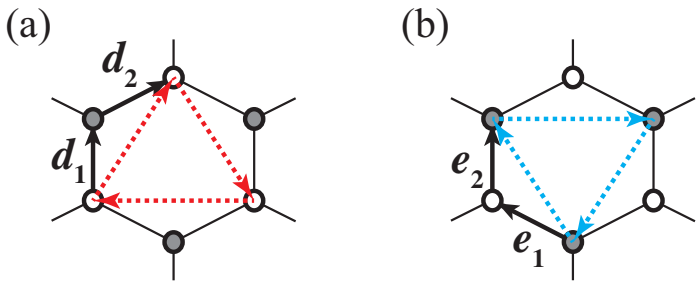

Figure 5-15: Next-nearest-neighbor hopping between (a) A-sublattice sites (open circles), and (b) B-sublattice sites (shaded circles) on the honeycomb lattice. $\boldsymbol{d}_{1,2}$ and $\boldsymbol{e}_{1,2}$ are the vectors between nearest-neighbor sites. Red and blue arrows represent the hopping process with the hopping direction $\boldsymbol{d}_1+\boldsymbol{d}_2$ and $\boldsymbol{e}_1+\boldsymbol{e}_2$, respectively.

Eq. (5.29) as

$$\begin{aligned}
[\mathscr{H}_{-n},\mathscr{H}_n] &= \sum_{ijkl} J_{ij}^{-n} J_{kl}^{n} [c_i^\dagger c_j, c_k^\dagger c_l] \\
&= \sum_{ijkl} J_{ij}^{-n} J_{kl}^{n} \left([c_i^\dagger c_j, c_k^\dagger] c_l + c_k^\dagger [c_i^\dagger c_j, c_l] \right) \\
&= \sum_{ijkl} J_{ij}^{-n} J_{kl}^{n} \left(\delta_{jk} c_i^\dagger c_l - \delta_{il} c_k^\dagger c_j \right) \\
&= \sum_{il} \sum_{j} (J_{ij}^{-n} J_{jl}^{n} - J_{ij}^{n} J_{jl}^{-n}) c_i^\dagger c_l, \qquad (5.33)
\end{aligned}$$

Therefore, the effective Hamiltonian of the tight-binding model (Eq. (5.30)) reads

$$\mathscr{H}_{\text{eff}} = \sum_{ij} \left(J_{ij}^0 + \sum_{n>0} \frac{K_{ij}^n}{n\Omega} \right) c_i^\dagger c_j, \qquad (5.34)$$

$$K_{ij}^n = \sum_k (J_{ik}^{-n} J_{kj}^{n} - J_{ik}^{n} J_{kj}^{-n}) \qquad (5.35)$$

Let us now apply the general formula Eq. (5.34) to the honeycomb lattice in circular fields. In the honeycomb lattice, the bare hopping J_{ij} is only present between nearest-neighbor sites. However, the effective hopping K_{ij}^n in Eq. (5.34) has nonzero elements between next-nearest-neighbor sites, as we show below. First, the bare hopping $J_{\boldsymbol{R}_j}(t)$, the matrix element of electron hopping with direction $\boldsymbol{R}_j$ (see Fig. 5-4(a)) in our model reads

$$\begin{aligned}
J_{\boldsymbol{R}_j}(t) &= J e^{-i\boldsymbol{R}_j\cdot\boldsymbol{A}(t)} \\
&= J e^{-iA\sin(\Omega t - 2\pi j/3)} \\
&= J \sum_n J_n(A) e^{2\pi i n j/3} e^{-n\Omega t}.
\end{aligned}$$

Taking the Fourier transform with t we have

$$J_{\boldsymbol{R}_j}^n = J J_n(A) e^{2\pi i n j/3}. \qquad (5.36)$$

Now we consider the next-nearest-neighbor hopping depicted in Fig. 5-15. As shown in Fig. 5-15(a), the next-nearest-neighbor hopping between A-sublattice sites are expressed by two nearest-neighbor hopping vectors $\boldsymbol{d}_1 = \boldsymbol{R}_0$ and $\boldsymbol{d}_2 = -\boldsymbol{R}_1$. Using Eq. (5.34), we obtain the effective hopping parameter as

$$\begin{aligned} K^n_{\boldsymbol{d}_1+\boldsymbol{d}_2} &= J^{-n}_{\boldsymbol{d}_2} J^n_{\boldsymbol{d}_1} - J^n_{\boldsymbol{d}_2} J^{-n}_{\boldsymbol{d}_1} \\ &= (J^n_{\boldsymbol{R}_1})^* J^n_{\boldsymbol{R}_0} - (J^{-n}_{\boldsymbol{R}_1})^* J^{-n}_{\boldsymbol{R}_0} \\ &= J_n^2(A)(e^{-2\pi i n/3} - e^{2\pi i n/3}) = -2iJ_n^2(A)\sin\frac{3\pi n}{2}. \end{aligned} \tag{5.37}$$

Similarly, the next-nearest neighbor hopping matrix in the B-sublattice, illustrated in Fig. 5-15(b), is calculated as

$$K^n_{\boldsymbol{e}_1+\boldsymbol{e}_2} = J^{-n}_{\boldsymbol{e}_2} J^n_{\boldsymbol{e}_1} - J^n_{\boldsymbol{e}_2} J^{-n}_{\boldsymbol{e}_1} = 2iJ_n^2(A)\sin\frac{3\pi n}{2}. \tag{5.38}$$

Substituting Eqs (5.36), (5.37) and (5.38) into Eq. (5.34), we finally obtain the effective Hamiltonian:

$$\mathscr{H}_{\text{eff}} = \sum_{\langle ij\rangle} J_{\text{eff}} c_i^\dagger c_j + i \sum_{\langle\langle ij\rangle\rangle} \nu_{ij} K_{\text{eff}} c_i^\dagger c_j, \tag{5.39}$$

$$J_{\text{eff}} = J J_0(A), \tag{5.40}$$

$$\begin{aligned} K_{\text{eff}} &= \frac{2J^2}{\Omega} \sum_{n=1}^{\infty} \frac{J_n^2(A)}{n} \sin\frac{2\pi n}{3} \\ &= \frac{2J^2}{\Omega}\left[\frac{\pi}{6} J_0^2(A) - \int_0^{\pi/6} J_0(2A\cos\theta) d\theta\right], \end{aligned} \tag{5.41}$$

where $\sum_{\langle ij\rangle}$ and $\sum_{\langle\langle ij\rangle\rangle}$ are the summation over all the nearest-neighbor and next-nearest-neighbor pairs, respectively. $\nu_{ij} = (2/\sqrt{3})(\boldsymbol{d}_2 \times \boldsymbol{d}_1)_z \in \{\pm 1\}$ is the chirality of the hopping path, where $\boldsymbol{d}_1$ and $\boldsymbol{d}_2$ are the nearest-neighbor vectors that connect the next-nearest-neighbor sites. In the second line in Eq. (5.41) we have used some formula for the Bessel functions (see Appendix E).

Importantly, K_{eff} is a real number and thus the effective hopping matrix iK_{eff} is pure imaginary. Therefore an electron acquires a phase factor $e^{\pm i\pi/2}$ after the next-nearest-neighbor hopping. The Hamiltonian Eq. (5.39) is indeed equivalent to the Haldane model [19] that we have introduced in the introduction of this chapter. Our effective Hamiltonian corresponds to the Haldane model with an alternating flux $\varphi = \pi/2$.

In order to investigate the sign dependence, we plot K_{eff} along with $J_0(A)$ against field strength A in Fig. 5-16. K_{eff} oscillates and changes sign (infinitely many times) as A increases. Inverting sign of K_{eff} is equivalent to adding an additional flux: $\varphi \to \varphi + \pi$ and leads to, according to the phase diagram of the Haldane model (Fig. 5-1), a topological phase transition with a shift of the Chern number $\nu = \pm 1 \to \mp 1$.

In fact, the zeros of K_{eff} do indeed coinside with the boundary between $\sigma_{xy} > 0$ and $\sigma_{xy} < 0$ along $U = 0$ axis in Fig. 5-13. Thus we can conclude that the topological phase transition against field strength A can be understood in terms of the effective Haldane model (Eq. (5.39)) in the off-resonant regime.

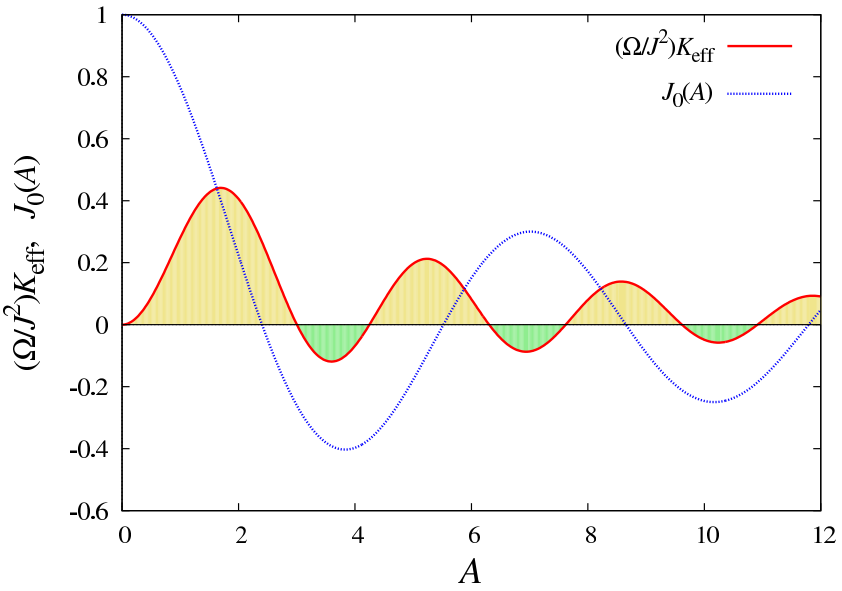

Figure 5-16: The effective next-nearest-neighbor hopping parameter $K_{\rm eff}$ (Eq.5.41) normalized by J^2/Ω, against the field strength A. Positive and negative regions of $K_{\rm eff}$ are emphasized as the yellow and green shaded regions, respectively. $J_0(A)(\propto J_{\rm eff})$ is also plotted for comparison.

5.3.3 Nonequilibrium steady states in resonant fields

We now turn to the resonant field regime: $\Omega < W$. In this regime, photo-excited carriers appear and give substantial differences from the off-resonant regime that is explained by the properties of the effective Hamiltonian.

In Fig. 5-17 we show the density of states and effective distribution function for $U = 2$ and $\Omega = 4$. Photo-induced SMIT is observed in Fig. 5-17(a) in a manner similar to the off-resonant case (Fig. 5-8). An important difference, however, is the non-monotonic behavior of the effective distribution function (Fig. 5-17(b)).

As we stressed in the previous subsection, in the off-resonant case the distribution function does not significantly deviate from the Fermi-Dirac distribution. Therefore the transport properties are basically explained by the static properties of the effective Hamiltonian. In the resonant case, however, the distribution function is no longer monotonic and gives substantial differences in physical observables.

In Fig. 5-18 we show the dc-conductivities σ_{xx} and σ_{xy} for resonant and off-resonant photon energies. σ_{xx} is suppressed with increasing A for all $\Omega = 1.0, 4.0, 10.0$, indicating that the system goes from semimetal to insulator. Surprisingly, σ_{yx} *changes sign* for the photon energy Ω in a low field strength, which means that the direction of Hall current can be inverted by the choice of photon energy.

In order to investigate further, in Fig. 5-19(a) we show the Hall conductivity σ_{xy} against the field strength A for various values of photon energy Ω in the noninteracting case. Since the topological gap is proportional to A^2 in the weak-field limit, the Hall conductivity also has an asymptotic form $\sigma_{xy} \propto A^2 (A \to 0)$[29]. In Fig. 5-19(b) we show the asymptotic coefficient

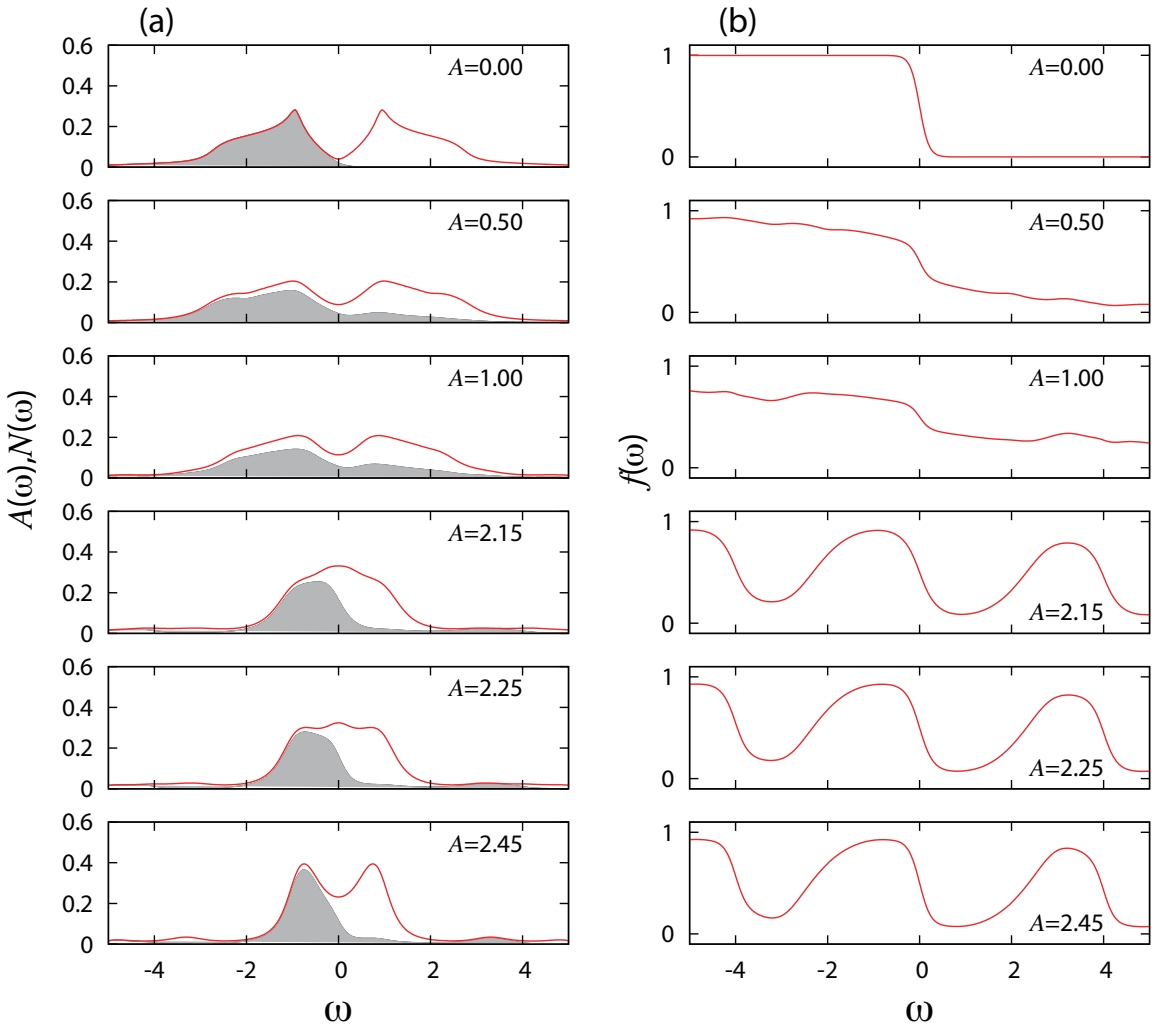

Figure 5-17: (a) Density of states and (b) effective distribution functions for various field strength A in a resonant regime $\Omega = 4$. Parameters used here are $J = 1, U = 2, \Gamma = 0.1$ and $T = 0.1$.

given by $\lim_{A\to 0} \sigma_{xy}/A^2$.

An important finding here is that the sign of σ_{xy} can be changed by the photon energy Ω. Oka, *et al.* [29] have numerically shown that, for $\Omega = 0.3$ and $A \sim 0.1$, the Hall current is induced in the $-y$ direction, that is, $\sigma_{yx} < 0$. Our result is consistent with their results, and indicates that a sign change of the Hall current may occur in their model by increasing the frequency Ω.

To clarify the origin of the sign change, we plot the $\boldsymbol{k}$-resolved Hall conductivity $g(\boldsymbol{k})$, Eq. (5.22), in Fig. 5-20. We can see that $g(\boldsymbol{k})$ exhibits different patterns as Ω is changed. An important observation here is that these patterns and the energy surfaces $\epsilon_{\boldsymbol{k}} = \pm\Omega/2$, as illustrated in Fig. 5-21, coincide with each other.

The origin of the contribution from the energy surfaces is the Floquet band gap caused by the mixing of Floquet side bands. In Fig. 5-22 we plot the $\boldsymbol{k}$-resolved spectral function

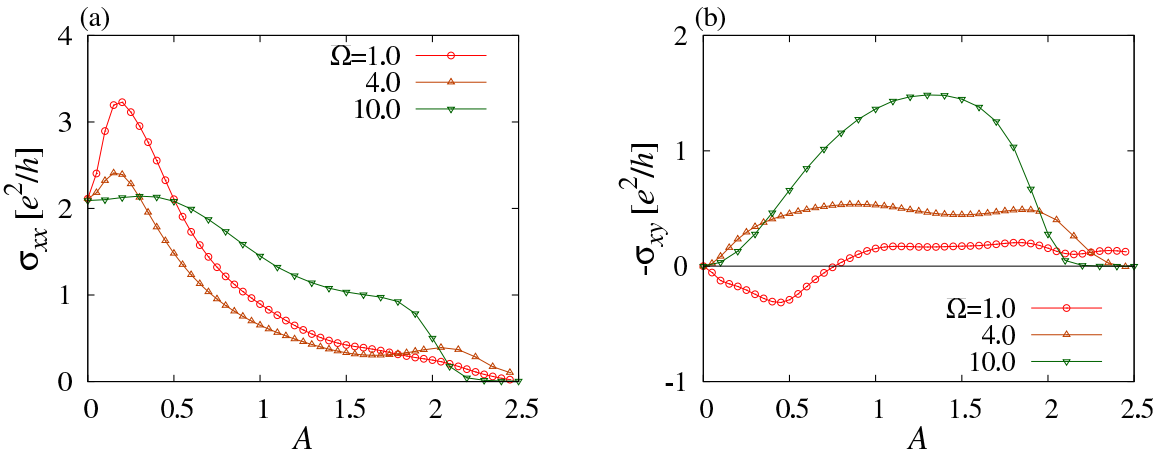

Figure 5-18: (a) σ_{xx} and (b) σ_{xy} for resonant field $\Omega = 1.0, 4.0$ and off-resonant field $\Omega = 10.0$. Parameters used here are $J = 1, U = 2, \Gamma = 0.1$ and $T = 0.1$.

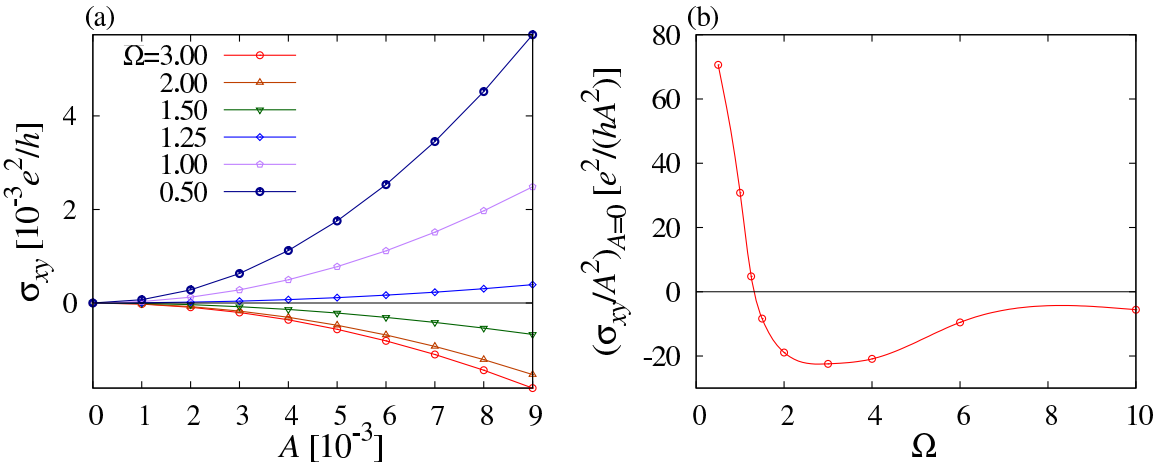

Figure 5-19: (a) σ_{yx} against weak intensity A, for various values of Ω in the resonant regime. (b) quadratic coefficient given by $\lim_{A\to 0} \sigma_{yx}/A^2$ for each Ω in (a). Parameters used here are $J = 1, U = 0, \Gamma = 0.06$ and $T = 0.06$.

for $\Omega = 1$ in the noninteracting case. We observe the topological gap at $\omega = 0$ and the gap between the original band and a Floquet side band at $\omega = \Omega/2$. Since the Berry curvature has large contributions around the gap, the patterns in Fig. 5-20 originate from the Berry curvature at the Floquet band gap at $\omega = \pm\Omega/2$.

Figure 5-20 also indicates that the Berry curvature contributes not isotropically around the Dirac points. Since the Berry curvature itself does not change sign around the Dirac points [29], the sign inversion of $g(\boldsymbol{k}) = \sum_m \mathscr{B}_{m\boldsymbol{k}} f_{m\boldsymbol{k}}$ should originate from the non-equilibrium distribution function $f_{m\boldsymbol{k}}$ which depend on the Bloch momentum $\boldsymbol{k}$. To demonstrate the statement, we replace the nonequilibrium distribution function by thermal distribution function, $f_{\mathrm{FD}}(\epsilon_{m\boldsymbol{k}})$, where $f_{\mathrm{FD}}(\omega) = (1 + e^{\omega/T})^{-1}$ is the Fermi-Dirac distribution function. The resultant

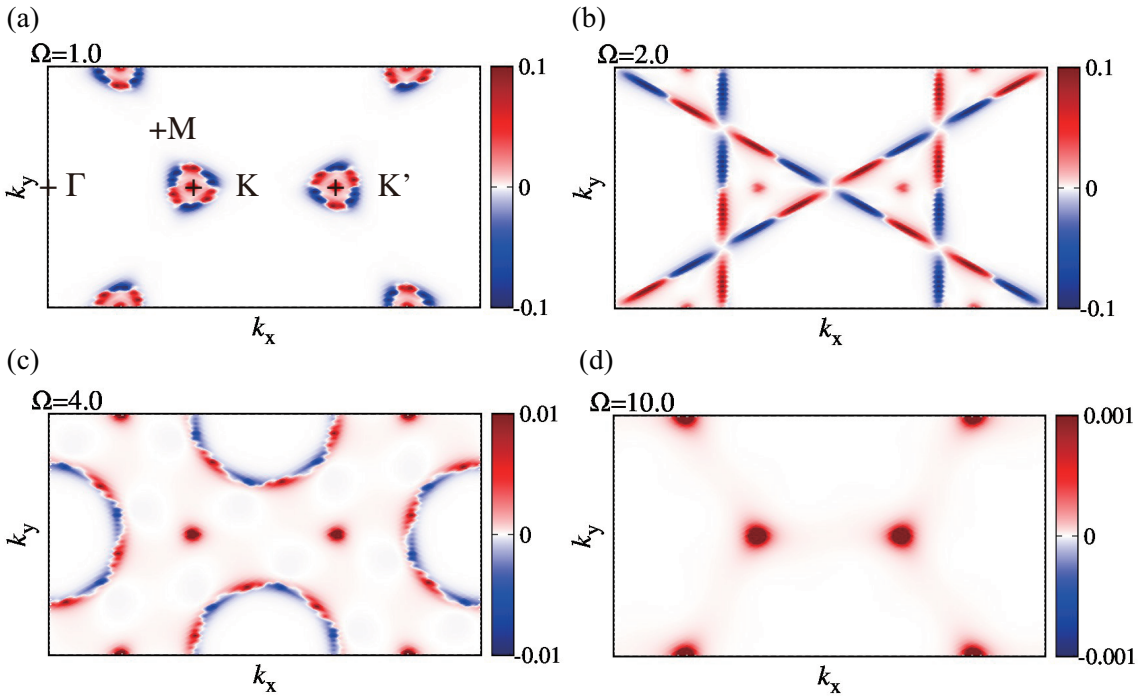

Figure 5-20: The $\boldsymbol{k}$-resolved Hall conductivity $g(\boldsymbol{k})$ for various values of Ω. Parameters used here are $A = 0.005, J = 1, U = 0, \Gamma = 0.06$ and $T = 0.06$.

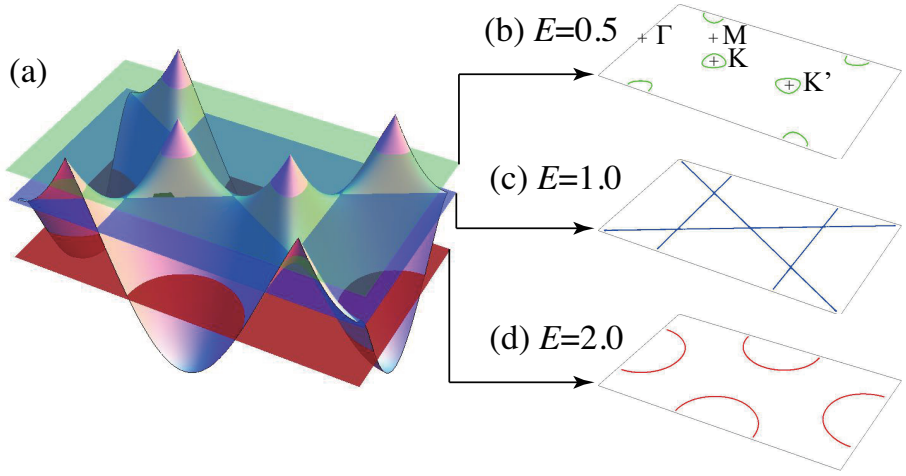

Figure 5-21: Energy surfaces of the honeycomb lattice. (a) The lower part of the honeycomb band structure $\omega = \pm\epsilon_{\boldsymbol{k}}$, where $\epsilon_{\boldsymbol{k}}$ is given by Eq. (5.8). Equi-energy surfaces $\epsilon_{\boldsymbol{k}} = \Omega/2 = 0.5, 1.0, 2.0$ are respectively shown in (b), (c) and (d).

$\boldsymbol{k}$-resolved Hall conductivity $\tilde{g}(\boldsymbol{k})$ only has the information of the Berry curvature $\mathscr{B}_{m\boldsymbol{k}}$ and therefore we can factor out the effect of the distribution function $f_{m\boldsymbol{k}}$ by comparing $g(\boldsymbol{k})$ and $\tilde{g}(\boldsymbol{k})$. Strictly speaking, we have defined $\tilde{g}(\boldsymbol{k})$ as the same as $g(\boldsymbol{k})$ in Eq. (5.22) with an

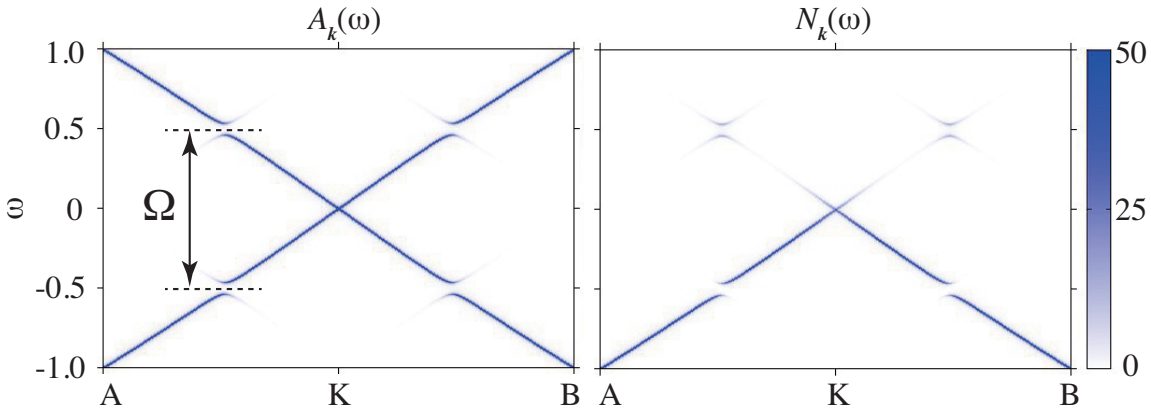

Figure 5-22: The $\boldsymbol{k}$-resolved spectral function $A_{\boldsymbol{k}}(\omega)$ and the occupation density $N_{\boldsymbol{k}}(\omega)$ for $\Omega = 1.0$. Parameters used here are $A = 0.05, J = 1, U = 0, \Gamma = 0.005$ and $T = 0.05$.

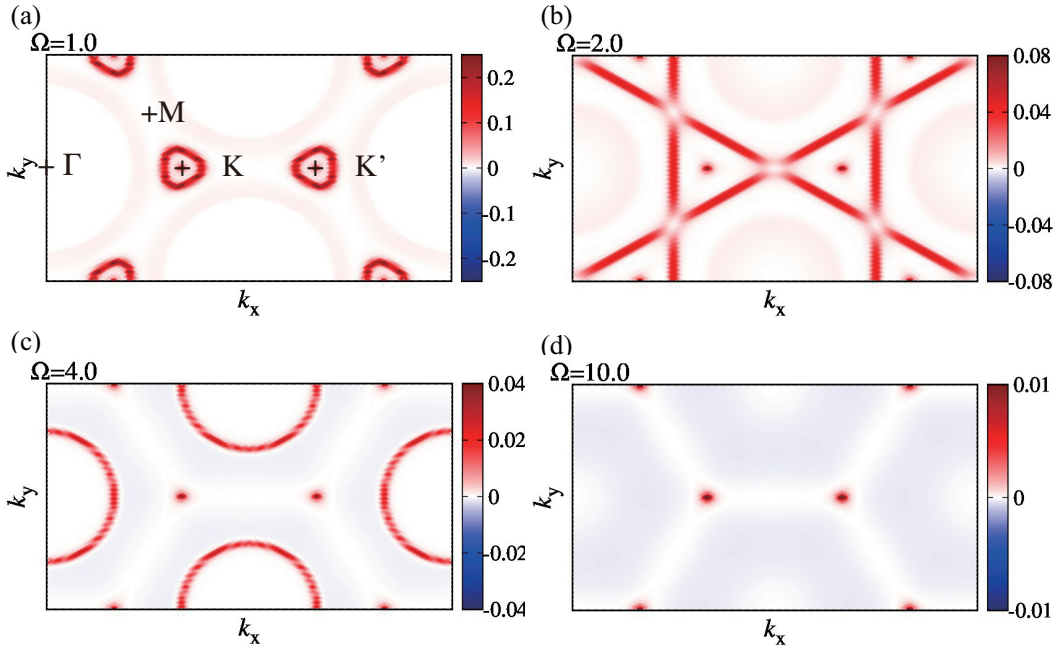

Figure 5-23: The contribution of the fictitiously thermalized Berry curvature $\tilde{g}(\boldsymbol{k})$ for various values of Ω. Parameters used here are $A = 0.005, J = 1, U = 0, \Gamma = 0.06$ and $T = 0.06$.

artificial lesser Green's functions that satisfy the fluctuation-dissipation theorem,

$$\hat{G}^K_{\boldsymbol{k}}(\omega) = \hat{G}^R_{\boldsymbol{k}}(\omega)\hat{F}(\omega) - \hat{F}(\omega)\hat{G}^A_{\boldsymbol{k}}(\omega), \tag{5.42}$$

$$\hat{F}(\omega) = \mathrm{diag}\left\{\tanh\frac{\omega + n\Omega}{2T}\right\}_{n=-\infty}^{\infty}. \tag{5.43}$$

Results are shown in Fig. 5-23. The patterns of the contributing k-points are similar to Fig.

5-20. However, the negative contributions are completely wiped out in the force-thermalized ones $\tilde{g}(\boldsymbol{k})$. This clearly shows that the k-dependent non-equilibrium distribution function indeed gives rise to the sign change of the Hall conductivity.

5.4 Summary

In this chapter, we have studied the honeycomb-Hubbard model in circularly polarized fields as a paradigm of the interplay of photo-induced topological states and electron correlation. We analyzed the electronic structures and transport properties of the steady states with Floquet-DMFT formalism extended to multi-band systems.

- In the off-resonant case ($\Omega \gg W$, with W the band width), we have obtained the phase diagram of the steady state quantitatively by calculating dc-conductivities. The topological phase, characterized by the gap at the Dirac point and a finite Hall conductivity σ_{xy}, is surprisingly robust against the electron interaction.

  More interestingly, we found the topological phase transition characterized by the sign inversion of the Hall-conductivity σ_{xy} as the strength of the field is varied. We have shown that the topological phase transition is clearly understood by the topological properties of the Haldane model, by mapping the time-dependent Hamiltonian into the effective Haldane model in the $\Omega \to \infty$ limit.

- In the resonant case, we have shown that the transport coefficient exhibits sign-change dependence on the photon-energy Ω. We clarified the origin of Ω dependence: in the off-resonant case the Berry curvature at the Dirac point contributes to σ_{xy}, while in the resonant case, the Berry curvature at the higher Floquet band gap as multiplied by $\boldsymbol{k}$-dependent nonequilibrium distribution function give rise to a negative Hall conductivity.

There are many interesting questions that we could not tackle in this study. Most importantly, we have not studied the ordered states. Although we have implicitly assumed that long-range magnetic orders do not appear, if long-range spin orders are taken into account, the Hubbard model on the honeycomb lattice exhibits antiferromagnetic order in the correlated regime. Further, there are interesting predictions, such as the presence [108] and the absence [109] of the spin-liquid phase, the emergence of density wave and unconventional superconductivity [110], all of which originate from electron-electron correlation on a honeycomb lattice [111]. It is thus interesting to investigate the fate of these ordered phases under the influence of ac-electric fields.

Chapter 6

Summary and outlook

6.1 Summary

In this thesis, we have studied correlated electron systems driven out of equilibrium by ac-electric fields. As we have stressed in the introduction (Chapter 1), orbital degrees of freedom give rise to more complex but rich physics that cannot be attributed to an effective single-band picture. Due to the rich physics, multiband electron systems are an especially interesting playground in the context of photo-induced phase transitions for theoretical and experimental interests, and our fundamental interest lies in understanding how multiband electron systems, which themselves possess various properties originating from orbital degrees of freedom, exhibit novel physics driven out of equilibrium under the influence of external fields.

In order to simulate nonequilibrium multiband correlated electron systems on the same footing, in Chapter 2 we have reviewed the time-dependent Green's function formalism and the dynamical mean-field theory (DMFT) to incorporate electron correlation in a non-perturbative manner. In Chapter 3 we have developed the Floquet dynamical mean-field theory (Floquet-DMFT), which was previously developed for single-band electron systems. The multiband extension naturally leads us to the physics of so-called photo-induced topological insulators, which is characterized by the photo-induced Berry curvature, and we have clarified the connection between the photo-induced Berry curvature and Floquet-Green's functions.

Having established the multiband Floquet-DMFT, we studied two interesting multiband systems, the *dp*-model and the honeycomb-Hubbard model (the Hubbard model on the honeycomb lattice) in ac-electric fields.

For the first application, in Chapter 4, we have studied nonequilibrium steady states in the *dp*-model in strong external ac-fields, motivated by a recent pump-probe measurements for high-T_c cuprates. In this study the photon energy Ω was varied from 4 eV to 20 eV and we found the following.

- We have numerically obtained the momentum-resolved density of states and distribution functions. For a small photon energy $\Omega = 4.0$ eV and a small intensity of the fields $A < 2$ (corresponding to the amplitude of the electric field $E = 2 \times 10^5$ kV/cm), the nonequilibrium distribution function deviates from the original distribution function

and resembles the Fermi-Dirac distribution function at higher temperatures, indicating that the effect of the external fields is basically understood as the effective rise of the temperature of the system.

- For a larger photon energy within the resonant regime $\Omega = 8.0$ eV, we also observed the deformation of the distribution function for a small field intensity A, while the band structure does not significantly deviate from that in equilibrium. The distribution function suggests population inversion and the system exhibits non-thermal effects, such as negative optical conductivities.

- For an off-resonant photon energy $\Omega = 20$ eV, the distribution function stays almost monotonic near the Fermi level for large $A \geq 2$ ($E \simeq 1 \times 10^6$ kV/cm), where the band structure highly deviates from original one. The population-inverted Floquet side bands appear far away from the Fermi level, and thus we also observe negative conductivities.

Secondly, in Chapter 5, we have studied nonequilibrium steady state in the honeycomb-Hubbard model in circularly polarized electric fields. The central motivation in this study is to investigate the interplay between photo-induced topological phases and the Mott insulating phase in the honeycomb-Hubard model under the influence of circularly polarized ac-fields. The results are summarized as follows.

- In the off-resonant case with photon energy $\Omega = 10J > W = 6J$, with W the band width and J the nearest-neighbor hopping, we have obtained a phase diagram with respect to the intensity A and the Hubbard repulsion U by calculating the double occupancy and dc-conductivities. The topological phase, characterized by the gap at the Dirac point and quantized Hall conductivity σ_{xy}, emerges in the strong-intensity regime. The quantization of σ_{xy} is also confirmed numerically. Although σ_{xy} is suppressed in the presence of Hubbard interaction U, the Hall conductivity σ_{xy} remains for large $U \simeq 5J$ and thus the photo-induced Hall effect is surprisingly robust against electron interaction.

- We found a topological-topological phase transition characterized by the sign inversion of the Hall conductivity σ_{xy} as the strength of the field is varied. We have shown that the topological-topological phase transition is clearly understood by the topological properties of the Haldane model, by mapping the time-dependent Hamiltonian into the effective Haldane model in the large-frequency limit $\Omega/W \gg 1$.

- In the resonant case $\Omega \leq W$, we have shown that the transport coefficient exhibits sign-change dependence on the photon-energy Ω. We clarified the origin of Ω dependence: in the off-resonant case, the Berry curvature at the Dirac point contributes to σ_{xy}, while in the resonant case, the Berry curvature at a higher Floquet band gap multiplied by the $\boldsymbol{k}$-dependent nonequilibrium distribution function gives rise to the negative σ_{xy}.

6.2 Future works

As we summarized above, we have studied steady states of multiband correlated electron systems in ac-electric fields with Floquet-DMFT and predicted novel phenomena in multi-

band systems driven by external fields for the first time. Here we pose short-term and long-term prospects.

6.2.1 Short-term outlook

First we present some questions that stem from our settings for the numerical simulations.

- *Impurity solver away-from-half filling.*— Throughout this study we have used the second-order iterative perturbation theory (IPT) as an impurity solver. It is empirically known that the second-order IPT gives qualitatively good results for the Hubbard model at half-filling. One reason for this is that, for half-filling, the second-order IPT accidentally reproduces the self-energy in the atomic limit $U \to \infty$. However, such nice properties are no longer guaranteed if one naively apply the second-order IPT to the cases for arbitrary filling.

  In order to investigate the Hubbard model away from half-filling, we may have several options. One option is to design some *modified* self-energy that reproduces the atomic limit, based on the original IPT. For example, Kajuater, *et al.* [60] introduced an asymptotic form of the self-energy using the original self-energy with the second-order IPT, and designed their asymptotic form so that asymptotic properties in $U \to \infty$ and $\omega \to \infty$ may be both maintained. They succeeded in reproducing the filling-controlled Mott transition in equilibrium. One may extend their approach to our nonequilibrium case.

  Another option is to use more elaborate impurity solvers, such as the non-crossing approximation (NCA) [112, 83, 113] and the quantum Monte Carlo (QMC) [114]. NCA is based on strong-coupling expansion and thus applicable to strongly correlated regime. QMC is in principle gives exact results, but the computational cost becomes severe around metal-insulator transitions. One may have to choose impurity solvers depending on the correlation strength of the system.

- *Choice of the heat-bath.*— As we have formulated in Sec. 2.1.5, we have assumed that a fermionic heat-bath is attached to the system. The virtue of this choice is that the bath degrees of freedom can be exactly integrated out and incorporated as an effective self-energy. On the other hand, the fermionic heat-bath model requires particle-exchange between the system and the bath and therefore the particle number is not exactly conserved. Besides, in real experiments, there are bosonic relaxation channels such as spin-waves and phonons. Thus, to be more realistic, bosonic heat-bath models, as developed in Refs. [84, 115], should be incorporated in our formalism.

- *Ordered phases.*— In this thesis we have not studied the ordered states such as magnetic phases and superconducting phases. It is known that the *dp*-model [74] and the honeycomb-Hubbard model [108, 109, 110] both have magnetic and superconducting phases and thus it is interesting to investigate how these ordered phases are disturbed or enhanced by external fields.

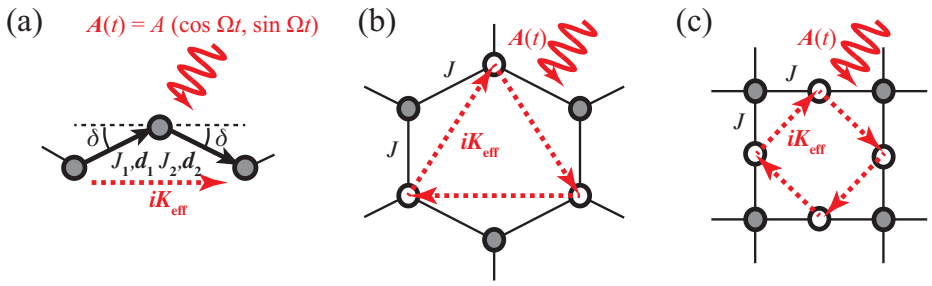

Figure 6-1: A photo-assisted next-nearest-neighbor (NNN) hopping processes in various types of lattices. Solid black lines represent nearest-neighbor (NN) hopping. Red dashed arrows represent photo-assisted NNN hopping processes. J and iK_{eff} represent NN and NNN hopping amplitudes, respectively. (a) A part of a general lattice structure containing NNN atoms, with NN vectors $\boldsymbol{d}_1$ and $\boldsymbol{d}_2$ with angle 2δ, in the circularly polarized light given by the vector potential $\boldsymbol{A}(t) = A(\cos\Omega t, \sin\Omega t)$. (b) The honeycomb lattice, and (c) the Lieb lattice in the circularly polarized ac-electric field.

6.2.2 Long-term outlook

In this thesis, we have especially studied the *dp*-model and the honeycomb-Hubbard model as applications of multiband Floquet-DMFT. There, we observed a dynamical reduction of bandwidths (known in the context of *the dynamical localization* of electrons in ac-fields [78]) and an emergence of photo-assisted anomalous hopping processes. In particular, in the case of honeycomb-Hubbard model, these dynamical effects result in novel photo-induced phase transitions, such as metal-to-insulator and topological-to-topological phase transitions.

Although we have studied some limited cases of multi-band lattice systems, we expect that the novel phase transitions discussed in this thesis can emerge in more general classes of multi-orbital systems. To see this, let us apply the perturbation theory, discussed in Sec. 5.3.2, for general multi-orbital systems. In Fig. 6-1 (a) we show a portion of an arbitrary lattice structure, containing next-nearest neighboring (NNN) atoms. We set J_1 and J_2 the nearest-neighbor (NN) hopping amplitudes and 2δ the angle between the NN vectors $\boldsymbol{d}_1$ and $\boldsymbol{d}_2$. Applying the formula Eq. (5.29) for the effective Hamiltonian in the off-resonant regime, we obtain an effective NNN hopping iK_{eff} in a circularly polarized field $\boldsymbol{A}(t) = A(\cos\Omega t, \sin\Omega t)$, with

$$K_{\text{eff}} = -\frac{2J_1J_2}{\Omega}\sum_{n=1}^{\infty}\frac{(-1)^n J_n^2(A)}{n}\sin 2n\delta. \tag{6.1}$$

In other words, the anomalous NNN hopping may ubiquitously appear in general lattices having angled NN bonds, under the influence of circularly polarized lights. We stress that anomalous NNN hopping cannot appear for single-orbital systems, where NNN paths with opposite angles ($\pm 2\delta$) always cancel with each other.

This observation motivates us to study steady states in circularly polarized lights for *general multi-orbital lattices having angled NN bonds*. The study of the honeycomb lattice in Chap. 5 can be regarded as one case-study for the class of lattices. The honeycomb lattice

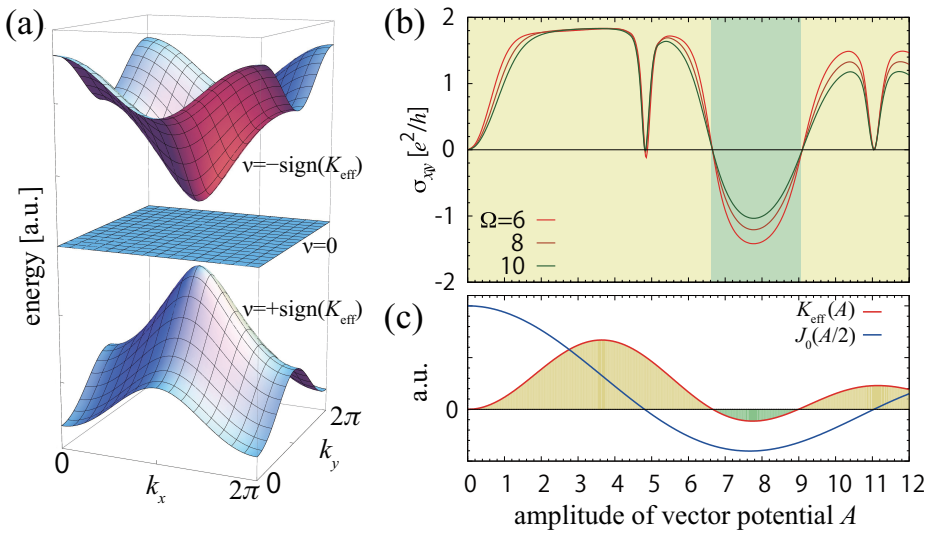

Figure 6-2: (a) The band structure of the effective lattice model for the Lieb lattice in off-resonant circularly polarized lights. Chern numbers for upper, middle (flat) and lower bands are $-\mathrm{sign}K_{\rm eff}$, 0 and $+\mathrm{sign}K_{\rm eff}$, respectively. (b) The Hall conductivity and (c) the effective next-nearest-neighbor hopping amplitude as functions of the amplitude of the vector potential A.

in circularly polarized light acquires the complex NNN hopping (Fig. 6-1(b)) and turns to Haldane's model, a prototypical model for Chern insulators. This idea can then be utilized to design other Chern insulators, which may be more feasible in real materials or optical lattice systems.

For example, in Appendix G we demonstrate designing the checkerboard lattice [116, 117], another typical Chern insulator, starting from the Lieb lattice in circularly polarized lights. Figure 6-1(c) shows the Lieb lattice in a circularly polarized light. The Lieb lattice consists of three atoms per unit cell with no level offset between the atoms. The geometry of the Lieb lattice may be found in real materials, such as CuO_2 plane in cuprates. There are even a proposals for simulating Lieb model in optical lattice systems [118]. The photo-induced NNN hopping resembles the anomalous NNN hopping in the checkerboard lattice [116, 117]. As a result, topologically nontrivial bands emerge and topological-to-topological phase transitions can be observed, as in the case of the honeycomb lattice. In Fig. 6-2(a) we show the band structure of the effective Lieb model Eq. (G.7) for an off-resonant frequency. The Dirac point at $\boldsymbol{k} = (\pi, \pi)$, which is gapless in equilibrium, becomes gapped in the circularly polarized lights. As the amplitude of the vector potential A is increased, sign-inversions of the effective NNN hopping given in Eq. (6.1) take place and we observe topological-to-topological phase transitions, as shown in Fig. 6-2(b)(c). The bandwidth of the effective Hamiltonian is scaled by the Bessel function $J_0(A/2)$ and the photo-induced Mott-transition will also take place for certain values of A in the presence of the on-site Coulomb repulsion.

We have thus demonstrated the novel photo-induced phase transition in a variety of multi-orbital systems and have shown a ubiquitousness of the photo-induced phase transitions discussed in this thesis. We expect that further investigations for other multi-orbital

systems will give insights for the choice of materials and experimental settings such as the intensity and the photon energy of the lasers, for the sake of the realizations of the interesting photo-induced phenomena investigated in this thesis.

Appendix A

Particle-hole symmetry

In some cases, systems possess a *particle-hole symmetry* (PHS), an accidental symmetry that strongly restricts the shape of Green's functions. Let us consider a lattice model with the following two properties.

(C1) The lattice can be decomposed into two sub-lattices and any particle hopping takes place only between the two sub-lattices.

(C2) The total number of particles is equal to the number of atoms (half filling).

A lattice structure that satisfies the first condition (C1) is called a *bipartite* lattice. For example, the square lattice and the honeycomb lattice with nearest-neighbor hopping are bipartite lattices.

The Hamiltonian for the Hubbard model having the two conditions (C1) and (C2) reads

$$\mathscr{H}(t) = \sum_{i\in\Lambda_{\mathrm{A}}}\sum_{j\in\Lambda_{\mathrm{B}}}\sum_{\sigma}\left[t_{ij}(t)c^{\dagger}_{i\sigma}c_{j\sigma} + t_{ij}(t)^{*}c^{\dagger}_{j\sigma}c_{i\sigma}\right] + \sum_{i\sigma}\frac{U_i(t)}{2}\left(\hat{n}_{i\sigma}-\frac{1}{2}\right)\left(\hat{n}_{i\bar{\sigma}}-\frac{1}{2}\right). \tag{A.1}$$

Here, we have assumed that the lattice is decomposed into A- and B-sublattices. Λ_{A} and Λ_{B} are the set of labels for atoms in A- and B-sublattices, respectively.

Now the particle-hole transformation operator $\hat{\mathscr{P}}$, with $\hat{\mathscr{P}}^2 = 1$, is defined as

$$\hat{\mathscr{P}} = \hat{P}\hat{K}, \tag{A.2a}$$

$$\hat{P}c_{i\sigma} = \begin{cases} c^{\dagger}_{i\sigma}, & i\in\Lambda_{\mathrm{A}} \\ -c^{\dagger}_{i\sigma}, & i\in\Lambda_{\mathrm{B}} \end{cases}. \tag{A.2b}$$

and $\hat{K}$ is the complex conjugation operator that acts on any c-number $c\in\mathbb{C}$ as $\hat{K}c = c^{*}$. The particle-hole operator $\hat{\mathscr{P}}$ transforms an annihilation operator to the corresponding creation operator with phase factor ± 1 for A- and B-sublattices, respectively. Using the definition and

fermionic commutation relations we have

$$\hat{\mathscr{P}}\left[t_{ij}(t)c^{\dagger}_{i\sigma}c_{j\sigma}\right]\hat{\mathscr{P}} = t_{ij}(t)^{*}c_{i\sigma}(-c^{\dagger}_{j\sigma}) = t_{ij}(t)^{*}c^{\dagger}_{j\sigma}c_{i\sigma},$$
$$\hat{\mathscr{P}}\left(c^{\dagger}_{i\sigma}c_{i\sigma}-\frac{1}{2}\right)\hat{\mathscr{P}} = c_{i\sigma}c^{\dagger}_{i\sigma}-\frac{1}{2} = -\left(c^{\dagger}_{i\sigma}c_{i\sigma}-\frac{1}{2}\right).$$

Thus the Hamiltonian Eq. (A.1) satisfies $\hat{\mathscr{P}}\hat{\mathscr{H}}(t)\hat{\mathscr{P}} = \hat{\mathscr{H}}$, showing that the Hamiltonian has PHS, $[\mathscr{H}(t),\hat{\mathscr{P}}] = 0$. Due to this symmetry, the local Green's functions possess the following symmetry:

$$\begin{aligned} G^{R}_{ii,\alpha\beta}(t,t') &= -i\theta(t-t')\langle[c_{i\alpha}(t),c^{\dagger}_{i\beta}(t')]_{+}\rangle && \text{definition.} \\ &= -i\theta(t-t')\langle[c^{\dagger}_{i,\alpha}(t),c_{i,\beta}(t')]_{+}\rangle && \text{PHS} \\ &= -G^{A}_{ii,\beta\alpha}(t',t), && \text{(A.3a)} \\ G^{K}_{ii,\alpha\beta}(t,t') &= -G^{K}_{ii,\beta\alpha}(t',t). && \text{(A.3b)} \end{aligned}$$

Especially in equilibrium, Eq. (A.3a) implies $G^{R}_{ii,\alpha\alpha}(\omega) = -G^{A}_{ii,\alpha\alpha}(-\omega)$ and thus the spectral function $A_{\alpha}(\omega) = (1/\pi)\mathrm{Im}G^{R}_{ii,\alpha\alpha}(\omega)$ is an even function of ω.

We can also express Eqs.(A.3) in the Floquet representation and we have

$$G^{R}_{\alpha\beta;mn}(\omega) = -G^{A}_{\beta\alpha;-n,-m}(-\omega) = -G^{R}_{\alpha\beta;-m,-n}(-\omega)^{*}, \quad \text{(A.4a)}$$
$$G^{K}_{\alpha\beta;mn}(\omega) = -G^{K}_{\beta\alpha;-n,-m}(-\omega). \quad \text{(A.4b)}$$

We have imposed this condition in the study of honeycomb lattice in Chapter 5.

Appendix B

Solving impurity problems with second-order perturbation theory

In this appendix, we solve the impurity problem, discribed by the action,

$$\begin{aligned} S &= S_0 + S_1, \\ S_0 &= \sum_\sigma \int_C dt\, dt'\, c_\sigma^\dagger(t) \tilde{\mathcal{G}}_\sigma^{-1}(t,t') c_\sigma(t'), \qquad \text{(B.1)} \\ S_1 &= \int_C dt\, U \left(n_\uparrow(t) - \alpha_\downarrow\right)\left(n_\downarrow(t) - \alpha_\uparrow\right), \qquad \text{(B.2)} \end{aligned}$$

in terms of Green's functions on the Keldysh contour $C = C_1 \cup C_2$, $C_1 : -\infty \to \infty$ and $C_2 : \infty \to -\infty$. As we have shown in Chapter 2, the Green's function $G_\sigma(t,t')$ can be expressed as

$$iG_\sigma(t,t') = \left\langle T_C c_\sigma(t) c_\sigma^\dagger(t') e^{-iS_1} \right\rangle, \qquad \text{(B.3)}$$

and its perturbation expansion with respect to S_1 is obtained as

$$G_\sigma(t,t') = G_\sigma^{(0)}(t,t') + G_\sigma^{(1)}(t,t') + G_\sigma^{(2)}(t,t') + \cdots.$$

The first-order term is given as the Feynman diagram in Fig.B-1(a) and calculated as

$$\begin{aligned} G_\sigma^{(1)}(t,t') &= -U \left\langle T_C c_\sigma(t) c_\sigma^\dagger(t') \int_C d\bar{t} \left(n_\uparrow(\bar{t}) - \alpha_\downarrow\right)\left(n_\downarrow(\bar{t}) - \alpha_\uparrow\right) \right\rangle_{\text{conn.}} \\ &= -U \left\langle T_C c_\sigma(t) c_\sigma^\dagger(t') \int_C d\bar{t}\, n_\sigma(\bar{t}) \left(n_{\bar{\sigma}}(\bar{t}) - \alpha_\sigma\right) \right\rangle_{\text{conn.}} \\ &= -U \int_C d\bar{t}\, i\tilde{\mathcal{G}}_\sigma(t,\bar{t}) \left[-i\tilde{\mathcal{G}}_{\bar{\sigma}}(\bar{t},\bar{t}^+) - \alpha_\sigma\right] i\tilde{\mathcal{G}}_\sigma(\bar{t},t') \\ &= U \iint_C d\bar{t} d\bar{t}'\, \tilde{\mathcal{G}}_\sigma(t,\bar{t}) [n_{\bar{\sigma}}^0(\bar{t}) - \alpha_\sigma] \delta_C(\bar{t},\bar{t}') \tilde{\mathcal{G}}_\sigma(\bar{t}',t'). \qquad \text{(B.4)} \end{aligned}$$

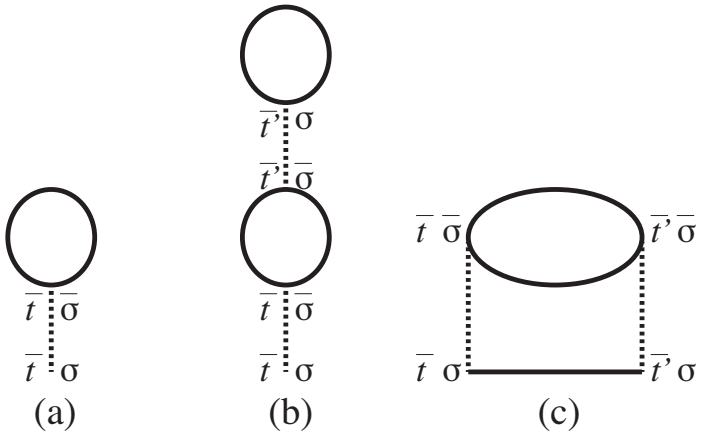

Figure B-1: Feynman diagrams up to the second order. Solid lines and dashed lines represent modified noninteracting Green's function $\tilde{\mathcal{G}}$ and interaction U, respectively. The variable $\bar{t},\bar{t}',\sigma$ and $\bar{\sigma}$ are the variables for integration used in the text.

The second-order terms are given as the Feynman diagram in Fig.B-1(b)(c) and calculated as

$$\begin{aligned} G_\sigma^{(2)}(t,t') &= -i\frac{(-iU)^2}{2}\Big\langle T_C c_\sigma(t)c_\sigma^\dagger(t') \\ &\times \iint_C d\bar{t}d\bar{t}'\left(n_\uparrow(\bar{t})-\alpha_\downarrow\right)\left(n_\downarrow(\bar{t})-\alpha_\uparrow\right)\left(n_\uparrow(\bar{t}')-\alpha_\downarrow\right)\left(n_\downarrow(\bar{t}')-\alpha_\uparrow\right)\Big\rangle_{\text{conn.}} \\ &= U^2\iint_C d\bar{t}d\bar{t}'\,\tilde{\mathcal{G}}_\sigma(t,\bar{t})\tilde{\mathcal{G}}_\sigma(\bar{t},\bar{t}')\tilde{\mathcal{G}}_\sigma(\bar{t}',t')\tilde{\mathcal{G}}_{\bar{\sigma}}(\bar{t},\bar{t}')\tilde{\mathcal{G}}_{\bar{\sigma}}(\bar{t}',\bar{t}) \qquad \text{(B.5)} \\ &- iU^2\iint_C d\bar{t}d\bar{t}'\,\tilde{\mathcal{G}}_\sigma(t,\bar{t})\tilde{\mathcal{G}}_\sigma(\bar{t},t')\tilde{\mathcal{G}}_{\bar{\sigma}}(\bar{t},\bar{t}')\tilde{\mathcal{G}}_{\bar{\sigma}}(\bar{t}',\bar{t})\left[i\tilde{\mathcal{G}}_\sigma(\bar{t}',\bar{t}'+0^+)-\alpha_{\bar{\sigma}}\right]. \qquad \text{(B.6)} \end{aligned}$$

Comparing the above results with

$$G_\sigma(t,t') = \tilde{\mathcal{G}}_\sigma(t,t') + \int_C d\bar{t}d\bar{t}'\tilde{\mathcal{G}}_\sigma(t,\bar{t})\Sigma_\sigma(\bar{t},\bar{t}')G_\sigma(\bar{t}',t')$$

we obtain the self-energy on the Keldysh contour up to the second order as

$$\Sigma_\sigma(t,t') = U[n^0_{\bar{\sigma}}(t)-\alpha_\sigma - i\chi_{\bar{\sigma}}(t)]\delta_C(t,t') + U^2\tilde{\mathcal{G}}_\sigma(t,t')\tilde{\mathcal{G}}_{\bar{\sigma}}(t,t')\tilde{\mathcal{G}}_{\bar{\sigma}}(t,t'), \qquad \text{(B.7)}$$

where $\chi_\sigma(t)$ is the internal tadpole contribution given by

$$\chi_\sigma(t) = \int_C d\bar{t}\,U[n_\sigma(t)-\alpha_{\bar{\sigma}}]\tilde{\mathcal{G}}_{\bar{\sigma}}(t,\bar{t})\tilde{\mathcal{G}}_{\bar{\sigma}}(\bar{t},t). \qquad \text{(B.8)}$$

Appendix C

Formula for the double occupancy in the multi-band Hubbard model

The purpose of this Appendix is the following.

- To obtain a general expression for the double occupancy in the multi-band Hubbard model,
$$\mathscr{H}(t) = \sum_{\alpha\beta} H^{(0)}_{\alpha\beta}(t) c^\dagger_\alpha c_\beta + \frac{1}{2}\sum_\alpha U_\alpha \hat{n}_\alpha \hat{n}_{\bar{\alpha}}, \tag{C.1}$$
where $\alpha = (i,a,\sigma)$ contains the site-index i, band-index a and spin-index $\sigma = \uparrow, \downarrow$. $\bar{\alpha}$ means spin-inversion: $\bar{\alpha} = (i,a,\bar{\sigma})$.

- To check the validity of the formula for the double occupancy Eq. (C.4) by applying it to the thermal equilibrium state in two different ways:
  - Baym-Kadanoff formalism. The interaction is present on the imaginary-time axis.
  - Keldysh formalism: We apply the adiabatic switching-on of the interaction and therefore the interaction is absent on the imaginary-time axis. Instead, we take the initial time $t_{\min}$ to be infinite past.

- To apply the formula to ac-driven systems and rewrite it in terms of Wigner functions.

We have assumed in Eq. (C.1) that there is no inter-band interactions, while the one-body part contains inter-band hopping terms.

C.1 Derivation of the formula for the double occupancy

The equation of motion for a Heisenberg operator $c_\alpha(t)$ reads

$$\begin{aligned} i\partial_t c_\alpha(t) &= [c_\alpha(t), \mathscr{H}(t)] \\ &= \sum_\beta H^{(0)}_{\alpha\beta}(t) c_\beta(t) + U_\alpha \hat{n}_{\bar{\alpha}}(t) c_\alpha(t). \end{aligned}$$

Using this relation, we have the derivative of contour-ordered Green's function,

$$G_{\alpha\gamma}(t,t') = -i\langle \mathrm{T}_C c_\alpha(t) c^\dagger_\beta(t')\rangle,$$

with respect to t as

$$i\partial_t G_{\alpha\gamma}(t,t') = \sum_\beta H^{(0)}_{\alpha\beta}(t) G_{\beta\gamma}(t,t') - iU_\alpha \langle \mathrm{T}_C\{\hat{n}_{\bar{\alpha}}(t)c_\alpha(t)\}c^\dagger_\gamma(t')\rangle + \delta_C(t,t'). \tag{C.2}$$

Setting $U_\alpha = 0$, we obtain the differential equation for non-interacting Green's function,

$$\sum_\beta [i\partial_t \delta_{\alpha\beta} - H^{(0)}_{\alpha\beta}(t)] G^{(0)}_{\beta\gamma}(t,t') = \delta_C(t,t'). \tag{C.3}$$

Therefore we obtain the inverse Green's function if we regard the LHS of above as the convolution $\sum_\beta \int_C G^{(0)-1}_{\alpha\beta}(t,\bar{t}) G^{(0)}_{\beta\gamma}(\bar{t},t')d\bar{t}$.

Using Eq. (C.3) and Eq. (C.2) with $\gamma = \alpha$ and $t' = t + 0$, we obtain

$$\sum_\beta \int_C d\bar{t}\, G^{(0)-1}_{\alpha\beta}(t,\bar{t}) G_{\beta\alpha}(\bar{t}, t+0) = iU_\alpha \langle \hat{n}_\alpha(t)\hat{n}_{\bar{\alpha}}(t)\rangle.$$

Plugging the relation $G^{(0)-1} = \Sigma + G^{-1}$, we finally obtain the formula for the double-occupancy as

$$\langle \hat{n}_\alpha(t)\hat{n}_{\bar{\alpha}}(t)\rangle = \frac{1}{iU_\alpha}\sum_\beta \int_C d\bar{t}\, \Sigma_{\alpha\beta}(t,\bar{t}) G_{\beta\alpha}(\bar{t},t). \tag{C.4}$$

C.2 Checking the validity of Eq. (C.4)

Thermal equilibrium state with Baym-Kadanoff formalism In this subsection, we apply the formula Eq. (C.4) to the thermal equilibrium situation and obtain the known formula in the previous works with DMFT [56]. We choose $t_{\min} = t_{\max} = 0$ on the contour C and assume the system is in thermal equilibrium at $t = 0$. The contour C therefore consists only of the C_3 branch. In this situation, Eq. (C.4) gives

$$\langle \hat{n}_\alpha(0)\hat{n}_{\bar{\alpha}}(0)\rangle = -\frac{1}{U_\alpha}\sum_\beta \int_0^{1/T} d\bar{\tau}\, \Sigma^{33}_{\alpha\beta}(0,-i\bar{\tau}) G^{33}_{\beta\alpha}(-i\bar{\tau},0).$$

The Matsubara component G^{33} and thermal Green's function G^{thm} are related with each other as

$$\begin{aligned} G^{33}(t,t') &= -i\langle \mathrm{T}_C\, c(t)c^\dagger(t')\rangle, \quad t,t' \in C_3, \\ G^{\mathrm{thm}}(\tau,\tau') &= -\langle \mathrm{T}_\tau\, c(\tau)c^\dagger(\tau')\rangle, \quad \tau,\tau' \in [0,1/T], \\ G^{33}(-i\tau,-i\tau') &= iG^{\mathrm{thm}}(\tau,\tau'). \end{aligned} \tag{C.5}$$

Therefore, we confirm the double-occupancy formula in the thermal Green's function formalism,

$$\langle \hat{n}_\alpha(0)\hat{n}_{\bar{\alpha}}(0)\rangle = \frac{1}{U_\alpha}\sum_\beta \int_0^{1/T} d\bar{\tau}\, \Sigma^{\mathrm{thm}}_{\alpha\beta}(0,\bar{\tau})G^{\mathrm{thm}}_{\beta\alpha}(\bar{\tau},0).$$

Thermal equilibrium state with Keldysh formalism In this subsection, let the interaction be absent at the infinite past $t_{\mathrm{min}} = -\infty$, and adiabatically be present at $t_{\mathrm{max}} = 0$. Due to the assumption, the self-energy $\Sigma^{31} = \Sigma^{13} = 0$ and Eq. (C.4) is reduced to

$$\begin{aligned}
\langle \hat{n}_\alpha(0)\hat{n}_{\bar{\alpha}}(0)\rangle &= \frac{1}{iU_\alpha}\sum_\beta \int_{-\infty}^{0} d\bar{t}\,[\Sigma^{>}_{\alpha\beta}(0,\bar{t})G^{<}_{\beta\alpha}(\bar{t},0) + \Sigma^{<}_{\alpha\beta}(0,\bar{t})G^{>}_{\beta\alpha}(\bar{t},0)] \\
&= \frac{1}{iU_\alpha}\sum_\beta \int_{-\infty}^{\infty} d\bar{t}\,[\Sigma^{\mathrm{R}}_{\alpha\beta}(0,\bar{t})G^{<}_{\beta\alpha}(\bar{t},0) + \Sigma^{<}_{\alpha\beta}(0,\bar{t})G^{\mathrm{A}}_{\beta\alpha}(\bar{t},0)] \\
&= \frac{1}{iU_\alpha}\sum_\beta \int_{-\infty}^{\infty} \frac{d\omega}{2\pi}\,[\Sigma^{\mathrm{R}}_{\alpha\beta}(\omega)G^{<}_{\beta\alpha}(\omega) + \Sigma^{<}_{\alpha\beta}(\omega)G^{\mathrm{A}}_{\beta\alpha}(\omega)].
\end{aligned}$$

Note that the fluctuation-dissipation theorem holds in thermal equilibrium:

$$\begin{aligned}
G^{\mathrm{R}} - G^{\mathrm{A}} = G^{>} - G^{<} = -(1+e^{\omega/T})G^{<}, \\
\Sigma^{\mathrm{R}} - \Sigma^{\mathrm{A}} = \Sigma^{>} - \Sigma^{<} = -(1+e^{\omega/T})\Sigma^{<}.
\end{aligned}$$

Eliminating $G^<$ and $\Sigma^<$, we obtain

$$\langle \hat{n}_\alpha(0)\hat{n}_{\bar{\alpha}}(0)\rangle = \frac{1}{iU_\alpha}\sum_\beta \int_{-\infty}^{\infty} \frac{d\omega}{2\pi}\,\frac{\Sigma^{\mathrm{A}}_{\alpha\beta}(\omega)G^{\mathrm{A}}_{\beta\alpha}(\omega) - \Sigma^{\mathrm{R}}_{\alpha\beta}(\omega)G^{\mathrm{R}}_{\beta\alpha}(\omega)}{1+e^{\omega/T}}. \tag{C.6}$$

Since $\Sigma^{\mathrm{R}}G^{\mathrm{R}}[\Sigma^{\mathrm{A}}G^{\mathrm{A}}]$ is the analytic continuation of $\Sigma^{\mathrm{tim}}G^{\mathrm{tim}}$ into the upper-half [lower-half] plane, and the function $(1+e^{\omega/T})^{-1}$ has poles at $\omega = i\omega_n = (2n+1)\pi iT$ with a residue $-T$, we can deform the integration path for $\Sigma^R(\omega)G^R(\omega)$ and $\Sigma^A(\omega)G^A(\omega)$ in Eq. (C.6) as shown in Fig. C-1. As a result, we can rewrite Eq. (C.6) as a sum of residues at $i\omega_n$ and thus obtain

$$\langle \hat{n}_\alpha(0)\hat{n}_{\bar{\alpha}}(0)\rangle = \frac{1}{U_\alpha} T \sum_{n=-\infty}^{\infty}\sum_\beta \Sigma^{\mathrm{thm}}(i\omega_n)G^{\mathrm{thm}}(i\omega_n). \tag{C.7}$$

C.3 Wigner Green's function representation of the formula

We have shown that, in Keldysh formalism, the double occupancy is given by

$$D_\alpha(t) := \langle \hat{n}_\alpha(t)\hat{n}_{\bar{\alpha}}(t)\rangle = \frac{1}{iU_\alpha}\int_{-\infty}^{\infty} d\bar{t}\,\left[\Sigma^{\mathrm{R}}_\alpha(t,\bar{t})G^{<}_\alpha(\bar{t},t) + \Sigma^{<}_\alpha(t,\bar{t})G^{\mathrm{A}}_\alpha(\bar{t},t)\right]. \tag{C.8}$$

In ac-driven situations, the Green's function $G(t,t')$ is periodic in the averaged-time domain: $G(t+T,t'+T) = G(t,t')$ where T is the period of the drive. Therefore we can define the Wigner

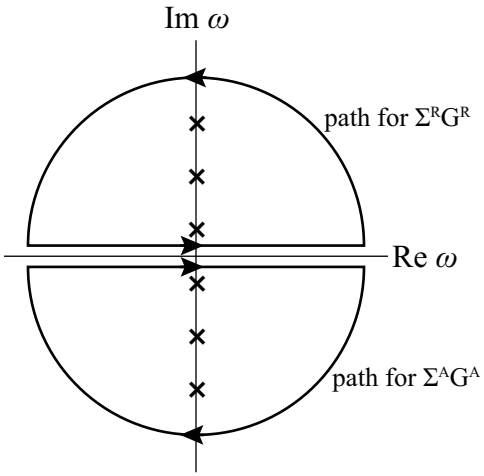

Figure C-1: Integration path for $\Sigma^{\mathrm{R}}G^{\mathrm{R}}$ and $\Sigma^{\mathrm{A}}G^{\mathrm{A}}$ on the complex ω-plane. Crosses on the imaginary axis represent $i\omega_n = (2n+1)\pi i T\,(n \in \mathbb{Z})$.

representation $G_n(\omega)$:

$$G_n(\omega) = \int_0^T \frac{dt_{\mathrm{av}}}{T} \int_{-\infty}^{\infty} dt_{\mathrm{rel}}\, e^{in\Omega t_{\mathrm{av}}} e^{i\omega t_{\mathrm{rel}}} G(t,t'),$$

where $t_{\mathrm{av}} = (t+t')/2$, $t_{\mathrm{rel}} = t - t'$. With this expression, the nth oscillating mode of the double-occupancy,

$$D_{\alpha n} := \int_0^T \frac{dt}{T} D_\alpha(t) e^{i\Omega n t},$$

is given by the formula,

$$D_{\alpha n} = \sum_m \int_{-\infty}^{\infty} \frac{d\omega}{2\pi} \left[\Sigma^{\mathrm{R}}_{\alpha,n+m}\left(\omega + \frac{n}{2}\Omega\right) G^{<}_{\alpha,-m}(\omega) + \Sigma^{<}_{\alpha,n+m}\left(\omega + \frac{n}{2}\Omega\right) G^{\mathrm{A}}_{\alpha,-m}(\omega) \right]. \tag{C.9}$$

Here we have utilized a formula,

$$\begin{aligned} C(t,t') &= \int_{-\infty}^{\infty} A(t,\bar{t}) B(\bar{t},t')\, d\bar{t} \\ &= \sum_{nn'} \int_{-\infty}^{\infty} \frac{d\omega}{2\pi} e^{-i(\omega+n\Omega)t} e^{i(\omega+n'\Omega)t'} A_n\left(\omega + \frac{n}{2}\Omega\right) B_{-n'}\left(\omega + \frac{n'}{2}\Omega\right), \\ C_n(t_{\mathrm{rel}} = 0) &= \sum_m \int_{-\infty}^{\infty} \frac{d\omega}{2\pi} A_{n+m}\left(\omega + \frac{n+m}{2}\Omega\right) B_{-m}\left(\omega + \frac{m}{2}\Omega\right). \end{aligned}$$

Appendix D

Photo-induced Berry curvature in terms of current matrices

In this appendix, we prove that the two expressions for the photo-induced Berry curvature,

$$\mathscr{B}^z_{\alpha\boldsymbol{k}} = \sum_{\beta(\neq\alpha)} (-i)\frac{\hat{w}^x_{\alpha\beta}\hat{w}^y_{\beta\alpha} - \hat{w}^y_{\alpha\beta}\hat{w}^x_{\beta\alpha}}{(\epsilon_{\alpha\boldsymbol{k}} - \epsilon_{\beta\boldsymbol{k}})^2}, \tag{D.1a}$$

$$\mathscr{B}^z_{\alpha\boldsymbol{k}} = \big[-i\nabla \times \langle u_{\alpha\boldsymbol{k}}|\nabla|u_{\alpha\boldsymbol{k}}\rangle \big]_z, \tag{D.1b}$$

coincide with each other. Here, $|u_{\alpha\boldsymbol{k}}\rangle$ is an eigenstate of the Schrödinger equation in the Floquet matrix form, Eq.(D.3). Starting from Eq.(D.1b), we have

$$\begin{aligned}
\mathscr{B}^i_{\alpha\boldsymbol{k}} &= -i\epsilon_{ijk}\partial_j\langle u_{\alpha\boldsymbol{k}}|\partial_k|u_{\alpha\boldsymbol{k}}\rangle \\
&= -i\epsilon_{ijk}\langle \partial_j u_{\alpha\boldsymbol{k}}|\partial_k u_{\alpha\boldsymbol{k}}\rangle \\
&= -i\epsilon_{ijk}\sum_{\beta(\neq\alpha)} \langle \partial_j u_{\alpha\boldsymbol{k}}|u_{\beta\boldsymbol{k}}\rangle\langle u_{\beta\boldsymbol{k}}|\partial_k u_{\alpha\boldsymbol{k}}\rangle,
\end{aligned} \tag{D.2}$$

where i,j,k run over x,y,z and summation over repeated indices is assumed. ϵ_{ijk} is Levi-Civita's anti-symmetric tensor. Now, recall the Schrödinger equation in terms of Floquet matrices,

$$(\hat{H}_{\boldsymbol{k}} - \hat{\Omega})|u_{\alpha\boldsymbol{k}}\rangle = \epsilon_{\alpha\boldsymbol{k}}|u_{\alpha\boldsymbol{k}}\rangle. \tag{D.3}$$

By taking the differential ∂_k for both sides and multiplying $\langle u_{\beta\boldsymbol{k}}|(\beta\neq\alpha)$ we obtain

$$\langle u_{\beta\boldsymbol{k}}|\hat{v}^k_{\boldsymbol{k}}|u_{\alpha\boldsymbol{k}}\rangle + \epsilon_{\beta\boldsymbol{k}}\langle u_{\beta\boldsymbol{k}}|\partial_k u_{\alpha\boldsymbol{k}}\rangle = \epsilon_{\alpha\boldsymbol{k}}\langle u_{\beta\boldsymbol{k}}|\partial_k u_{\alpha\boldsymbol{k}}\rangle,$$

with a current matrix $\hat{v}^k_{\boldsymbol{k}} = \partial_k\hat{H}_{\boldsymbol{k}}$. This equation leads to

$$\langle u_{\beta\boldsymbol{k}}|\partial_k u_{\alpha\boldsymbol{k}}\rangle = \frac{\langle u_{\beta\boldsymbol{k}}|\hat{v}^k_{\boldsymbol{k}}|u_{\alpha\boldsymbol{k}}\rangle}{\epsilon_{\alpha\boldsymbol{k}} - \epsilon_{\beta\boldsymbol{k}}}. \tag{D.4}$$

Plugging this into Eq.(D.2) we obtain

$$\mathscr{B}^{i}_{\alpha\boldsymbol{k}} = -i\epsilon_{ijk} \sum_{\beta(\neq\alpha)} \frac{\langle u_{\alpha\boldsymbol{k}}|\hat{v}^{j}_{\boldsymbol{k}}|u_{\beta\boldsymbol{k}}\rangle\langle u_{\beta\boldsymbol{k}}|\hat{v}^{k}_{\boldsymbol{k}}|u_{\alpha\boldsymbol{k}}\rangle}{(\epsilon_{\alpha\boldsymbol{k}} - \epsilon_{\beta\boldsymbol{k}})^2}. \tag{D.5}$$

The matrix element $\langle u_{\alpha\boldsymbol{k}}|\hat{v}^{j}_{\boldsymbol{k}}|u_{\beta\boldsymbol{k}}\rangle$ in the numerator of the Eq.(D.5) is nothing but the $\alpha\beta$ component of a Floquet matrix,

$$\hat{w}^{j}_{\boldsymbol{k}} = \hat{\Lambda}^{-1}_{\boldsymbol{k}}\hat{v}^{j}_{\boldsymbol{k}}\hat{\Lambda}_{\boldsymbol{k}}, \tag{D.6}$$

with $\hat{\Lambda}_{\boldsymbol{k}} = (u_{\alpha\boldsymbol{k}})_{\alpha\in\mathbb{Z}}$ and thus the above equation coincides with Eq.(D.1a).

Appendix E

Properties of the Bessel functions

In this Appendix, we summarize important properties of the Bessel functions of the first kind $J_n(z)$ we have used in the main text. Although there are several definitions of the Bessel functions, we define $J_n(z)$ by introducing its generating function and derive its properties and formulae, starting from Eq.(E.1) below.

Definition.—The Bessel function is defined by the Fourier expansion of the generating function $\Phi(\theta) \equiv e^{iz\sin\theta}$, a 2π-periodic function of θ, as

$$e^{iz\sin\theta} = \sum_{n=-\infty}^{\infty} J_n(z)e^{in\theta}, \quad z,\theta \in R. \tag{E.1}$$

By substituting $\theta \to \theta + \pi/2$, we obtain an equivalent expression,

$$e^{iz\cos\theta} = \sum_{n=-\infty}^{\infty} i^n J_n(z)e^{in\theta}, \quad z,\theta \in R. \tag{E.2}$$

From the definition, we obtain an explicit form of $J_n(z)$ as

$$\begin{aligned} J_n(z) &= \int_0^{2\pi} \frac{d\theta}{2\pi} e^{iz\sin\theta} e^{-in\theta} \\ &= \int_0^{\pi} \frac{d\theta}{2\pi} (e^{iz\sin\theta} e^{-in\theta} + e^{iz\sin(2\pi-\theta)} e^{-in(2\pi-\theta)}) \\ &= \int_0^{\pi} \frac{d\theta}{\pi} \cos(z\sin\theta - n\theta). \end{aligned} \tag{E.3}$$

We plot $J_n(z)$ for several values of n in Fig.E-1. Each $J_n(z)$ oscillates and has an infinite number of zeros. Zeros of $J_0(z)$, which play an important role in the physics of ac-driven systems, are shown in Fig.E-1. Note that the Bessel functions $J_n(z)$ for negative indices n and those for positive ones n are related by an equation,

$$J_{-n}(z) = J_n(-z) = (-1)^n J_n(z). \tag{E.4}$$

Neumann's addition theorem.—Next, we obtain some useful formula that we used in the main text. First we substitute $(\theta, z) = (\alpha, p), (\theta - \alpha, q)$ into Eq.(E.1) and multiply the two

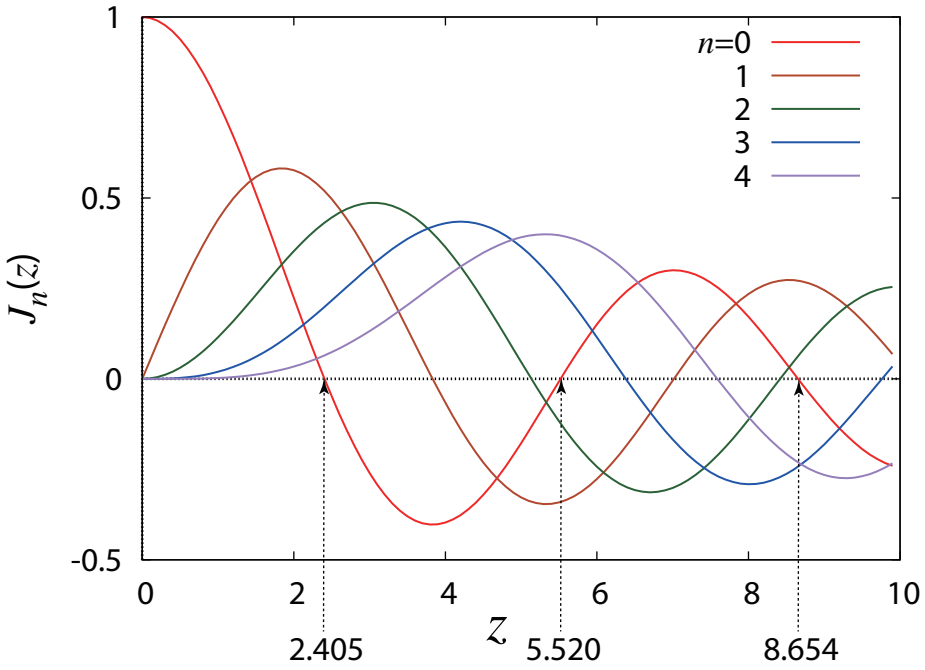

Figure E-1: The Bessel functions $J_n(z)$ for n from 0 to 4. Zeros of $J_0(z)$ are also shown.

equations to obtain

$$e^{i(p\sin\alpha+q\sin(\theta-\alpha))}=\sum_{m,n}J_m(p)J_n(q)e^{i((m-n)\alpha+n\theta)}. \tag{E.5}$$

The exponent on the LHS is transformed as

$$i(p\sin\alpha+q\sin(\theta-\alpha))=i\sqrt{p^2+q^2-2pq\cos\theta}\,\sin(\alpha+\alpha'),$$
$$\alpha'=\arctan\frac{q\sin\theta}{p-q\cos\theta}.$$

Now we integrate Eq.(E.5) over $\alpha\in[0,2\pi]$. Then the summation for m and n in RHS only remains for $m=n$. LHS coincides with the definition of $J_0(z)$ if we shift the integration variable as $\alpha\to\alpha-\alpha'$. Thus we obtain so-called Neumann's addition theorem for the Bessel functions:

$$J_0(\sqrt{p^2+q^2-2pq\cos\theta})=\sum_{n=-\infty}^{\infty}J_n(p)J_n(q)e^{in\theta}. \tag{E.6}$$

Other useful formula.—Especially, for $p=q>0$ and $0\le\theta\le2\pi$, Eq(E.6) gives

$$J_0\left(2p\sin\frac{\theta}{2}\right)=\sum_{n=-\infty}^{\infty}J_n(p)^2e^{in\theta}. \tag{E.7}$$

We further integrate Eq.(E.7) over $\theta\in[0,2\pi]$. Due to the redundancy: $\sin\left(\frac{\theta}{2}\right)=\sin\left(\frac{2\pi-\theta}{2}\right)$,

the integral of LHS gives $4\int_0^{\pi/2} J_0(2p\sin\theta)d\theta$. On RHS, $n \neq 0$ terms vanish and the $n = 0$ term gives $2\pi J_0(p)^2$. Thus we obtain

$$\int_0^{\pi/2} J_0(2z\cos\theta)d\theta = \frac{\pi}{2}J_0(z)^2. \tag{E.8}$$

Using above, one can calculate the following summation that appeared in the main text as

$$\begin{aligned}
\sum_{n=1}^{\infty}\frac{J_n(A)^2}{n}\sin\frac{2\pi n}{3} &= \int_0^{2\pi/3}\sum_{n=1}^{\infty} J_n(A)^2\cos n\theta d\theta \\
&= \int_0^{2\pi/3}\frac{1}{2}\left[J_0\left(2A\sin\frac{\theta}{2}\right) - J_0(A)^2\right]d\theta \\
&= -\frac{\pi}{3}J_0(A)^2 + \int_0^{\pi/3} J_0(2A\sin\theta)\,d\theta \\
&= -\frac{\pi}{3}J_0(A)^2 + \left(\int_0^{\pi/2} - \int_0^{\pi/6}\right)J_0(2A\cos\theta)\,d\theta \\
&= \frac{\pi}{6}J_0(A)^2 - \int_0^{\pi/6} J_0(2A\cos\theta)\,d\theta,
\end{aligned} \tag{E.9}$$

where we have used Eq.(E.7) on the second line and Eq.(E.8) in the last transformation.

Appendix F

Detailed calculation of the Floquet matrices of the dp-model in ac-fields

In this Appendix, we show the detailed calculation of the Floquet matrix elements of the Hamiltonian $H_{0,\boldsymbol{k}+\boldsymbol{A}(t)}$ in Eq.(4.2c). We consider the two types of external fields—linearly polarize lights, and circularly polarize lights.

Linearly polarized lights—The vector potential is given by $\boldsymbol{A}_L(t) = (A\cos\Omega t, A\cos\Omega t)$ and we substitute $\boldsymbol{k} \to \boldsymbol{k} + \boldsymbol{A}_L(t)$ in Eq.(4.2c). From the d-p hopping term we have the matrix element as

$$\begin{aligned}
t_{dp}\sin\left(\frac{k + A\cos\Omega t}{2}\right) &= \left[\frac{t_{dp}}{2i}e^{ik/2}e^{i(A/2)\cos\Omega t}\right] + \text{c.c.} \\
&= \left[\frac{t_{dp}}{2i}e^{ik/2}\sum_{n=-\infty}^{\infty} i^n J_n\left(\frac{A}{2}\right)e^{in\Omega t}\right] + \text{c.c.} \\
&= \frac{t_{dp}}{2i}\sum_{n=-\infty}^{\infty}\left[e^{ik/2}i^n J_n\left(\frac{A}{2}\right) - e^{-ik/2}i^n J_{-n}\left(\frac{A}{2}\right)\right]e^{in\Omega t} \\
&= t_{dp}\sum_{n=-\infty}^{\infty}\sin\left(\frac{k+n\pi}{2}\right)J_n\left(\frac{A}{2}\right)e^{in\Omega t}. \qquad \text{(F.1)}
\end{aligned}$$

From the p-p hopping term we have

$$\begin{aligned}
&2t_{pp}\sin\left(\frac{k_x + A\cos\Omega t}{2}\right)\sin\left(\frac{k_y + A\cos\Omega t}{2}\right) \\
&\quad = t_{pp}\left[-\cos\left(\frac{k_x+k_y}{2} + A\cos\Omega t\right) + \cos\left(\frac{k_x - k_y}{2}\right)\right] \\
&\quad = t_{pp}\left[-\sin\left(\frac{k_x+k_y+\pi}{2} + A\cos\Omega t\right) + \cos\left(\frac{k_x - k_y}{2}\right)\right] \\
&\quad = -t_{dp}\sum_{n=-\infty}^{\infty}\cos\left(\frac{k_x+k_y+n\pi}{2}\right)J_n(A)e^{in\Omega t} + t_{pp}\cos\left(\frac{k_x-k_y}{2}\right), \qquad \text{(F.2)}
\end{aligned}$$

where we have used the definition of the Bessel function Eq.(E.2). In the last transformation we used Eq.(F.1).

Circularly polarized lights—The vector potential is given by $\boldsymbol{A}_C(t) = (A\cos\Omega t, A\sin\Omega t)$ and we substitute $\boldsymbol{k} \to \boldsymbol{k} + \boldsymbol{A}_C(t)$ in Eq.(4.2c). From the d-p hopping term, in addition to

Eq.(F.1) in the case of linearly polarized lights, we have another matrix element,

$$t_{dp}\sin\left(\frac{k+A\sin\Omega t}{2}\right)=t_{dp}\sin\left(\frac{k+A\cos(\Omega t-\pi/2)}{2}\right)$$
$$=t_{dp}\sum_{n=-\infty}^{\infty}(-i)^n\sin\left(\frac{k+n\pi}{2}\right)J_n\left(\frac{A}{2}\right)e^{in\Omega t}. \tag{F.3}$$

In the first line, we have just substituted $\Omega t\to\Omega t-\pi/2$ in Eq.(F.1), since $\cos\Omega t$ is transformed to $\sin\Omega t$ and Eq.(F.1) coincides with the matrix element that we wanted to calculate above. From the p-p hopping term we have, with $K^{\pm}=(k_x\pm k_y)/2$,

$$\begin{aligned}
&2t_{pp}\sin\left(\frac{k_x+A\cos\Omega t}{2}\right)\sin\left(\frac{k_y+A\sin\Omega t}{2}\right)\\
&=t_{pp}\left\{-\sin\left[K^{+}+\frac{\pi}{2}+\frac{A}{\sqrt{2}}\sin\left(\Omega t+\frac{\pi}{4}\right)\right]+\sin\left[K^{-}+\frac{\pi}{2}-\frac{A}{\sqrt{2}}\sin\left(\Omega t-\frac{\pi}{4}\right)\right]\right\}\\
&=t_{pp}\sum_{n=-\infty}^{\infty}\Bigg[-(-i)^n\cos\left(K^{+}+\frac{n\pi}{2}\right)J_n\left(\frac{A}{\sqrt{2}}\right)e^{in(\Omega t+pi/4)}\\
&+(-i)^n\cos\left(K^{-}+\frac{n\pi}{2}\right)J_n\left(-\frac{A}{\sqrt{2}}\right)e^{in(\Omega t-\pi/4)}\Bigg]\\
&=t_{pp}\sum_{n=-\infty}^{\infty}\left\{e^{in\pi/4}\cos\left(\frac{k_x-k_y+n\pi}{2}\right)-e^{-in\pi/4}\cos\left(\frac{k_x+k_y+n\pi}{2}\right)\right\}J_n\left(\frac{A}{\sqrt{2}}\right)e^{in\Omega t},
\end{aligned}\tag{F.4}$$

where we have substituteed $k\to K^{\pm}\pm\pi/2$ in Eq.(F.3).

Appendix G

Properties of the Lieb model in circularly polarized ac-fields

G.1 Tight-binding model for Lieb model

The Lieb model consists of three orbitals, d, p_x and p_y as depicted in Fig.G-1. The tight-binding Hamiltonian up to next nearest neighbor hoppings reads

$$\mathscr{H} = \mathscr{H}_0 + \mathscr{H}_1 + \mathscr{H}_2, \tag{G.1a}$$

$$\mathscr{H}_0 = \sum_i \epsilon_d d_i^\dagger d_i + \sum_l \epsilon_p p_l^\dagger p_l, \tag{G.1b}$$

$$\mathscr{H}_1 = \sum_i J d_i^\dagger (p_{i+\hat{x}/2} + p_{i+\hat{y}/2} + p_{i-\hat{x}/2} + p_{i-\hat{y}/2}) + \text{h.c.}, \tag{G.1c}$$

$$\mathscr{H}_2 = \sum_i K e^{i\phi} (p_{i+\hat{x}/2}^\dagger p_{i+\hat{y}/2} + p_{i+\hat{y}/2}^\dagger p_{i-\hat{x}/2} + p_{i-\hat{x}/2}^\dagger p_{i-\hat{y}/2} + p_{i-\hat{y}/2}^\dagger p_{i+\hat{x}/2}) + \text{h.c.}, \tag{G.1d}$$

where $\mathscr{H}_0$ is the on-site energy of each site, $\mathscr{H}_1$ represents nearest neighbor (NN) hopping processes , and $\mathscr{H}_2$ is next-nearest neighbor (NNN) hopping. For later convenience we multiplied phase factor $e^{i\phi}$ to the NNN hopping parameters. We shall show in Sec.G.2.1 that the complex hopping parameter appears as a result of the circularly polarized field, even if the original Hamiltonian does not contain NNN hopping process: $K = 0$.

By the standard tight-binding calculation, we obtain the noninteracting Hamiltonian $\mathscr{H}_0$ as

$$\mathscr{H}_0 = \sum_{\boldsymbol{k}} \psi_{\boldsymbol{k}}^\dagger H_{0\boldsymbol{k}} \psi_{\boldsymbol{k}}, \tag{G.2a}$$

$$\psi_{\boldsymbol{k}} = \begin{pmatrix} d_{\boldsymbol{k}} & p_{x,\boldsymbol{k}} & p_{y,\boldsymbol{k}} \end{pmatrix}^t, \tag{G.2b}$$

$$H_{0\boldsymbol{k}} = \begin{pmatrix} \epsilon_d & 2J\cos\frac{k_x}{2} & 2J\cos\frac{k_y}{2} \\ 2J\cos\frac{k_x}{2} & \epsilon_p & 2K\left[\cos\left(\frac{k_x+k_y}{2}\right)e^{-i\phi} + \cos\left(\frac{k_x-k_y}{2}\right)e^{i\phi}\right] \\ 2J\cos\frac{k_y}{2} & 2K\left[\cos\left(\frac{k_x+k_y}{2}\right)e^{i\phi} + \cos\left(\frac{k_x-k_y}{2}\right)e^{-i\phi}\right] & \epsilon_p \end{pmatrix}. \tag{G.2c}$$

The band structure for the Lieb lattice for $K = 0$ is presented in Fig. G-2(a). There exists

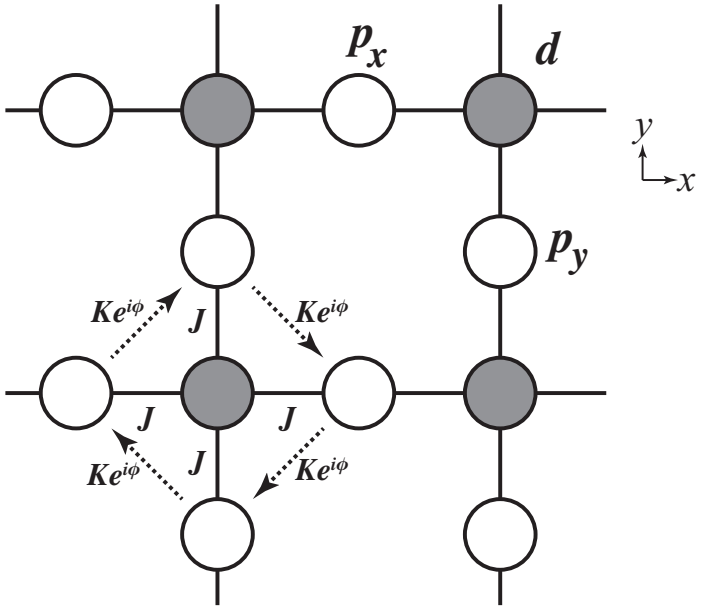

Figure G-1: The Lieb lattice. J and K are nearest and next-nearest neighbor hopping amplitudes, respectively. For reference a phase factor ϕ is attached to next-nearest neighbor hopping processes depicted as the dotted arrows in the figure.

a flat band and two dispersive bands, touching at a single Dirac point M(π,π).

G.2 The Lieb model in circularly polarized electric fields

We consider a circularly polarized electric field $\boldsymbol{E}(t) = -\partial_t \boldsymbol{A}(t)$, given by the vector potential

$$\boldsymbol{A}(t) = {}^t(A\cos\Omega t, A\sin\Omega t). \tag{G.3}$$

The external field is included as the Peierls substitution: $\boldsymbol{k} \to \boldsymbol{k}+\boldsymbol{A}(t)$, and the Floquet matrix elements are calculated as

$$\hat{H}_{mn}(\boldsymbol{k}) = H_{0\boldsymbol{k},m-n} = \int_0^T \frac{dt}{T} H_{0,\boldsymbol{k}+\boldsymbol{A}(t)} e^{i(m-n)\Omega t}. \tag{G.4}$$

The Floquet matrices $H_{0\boldsymbol{k},n}$ are 3×3 matrices with the form

$$H_{0\boldsymbol{k},n} = \begin{pmatrix} \epsilon_d\delta_{n0} & a^*_{-n} & b^*_{-n} \\ a_n & \epsilon_p\delta_{n0} & c^*_{-n} \\ b_n & c_n & \epsilon_d\delta_{n0} \end{pmatrix}. \tag{G.5}$$

The parameters a_n, b_n and c_n are obtained from Eq.(G.4) with the noninteracting Hamiltonian Eq.(G.2c) and the vector potential Eq.(G.3), and we have

$$a_n = 2JJ_n\left(\frac{A}{2}\right)\cos\left(\frac{k_x+n\pi}{2}\right), \tag{G.6a}$$

$$b_n = 2JJ_n\left(\frac{A}{2}\right)(-i)^n\cos\left(\frac{k_y+n\pi}{2}\right), \tag{G.6b}$$

$$c_n = 2KJ_n\left(\frac{A}{\sqrt{2}}\right)\left[e^{-in\pi/4}e^{i\phi}\cos\left(\frac{k_x+k_y+n\pi}{2}\right)+e^{in\pi/4}e^{-i\phi}\cos\left(\frac{k_x-k_y+n\pi}{2}\right)\right]. \tag{G.6c}$$

G.2.1 Effective model, band structure, and topological phases in off-resonant case

From now on, we discard the bare NNN hopping: $K = 0$. Using the formula for an effective Hamiltonian in off-resonant fields Eq. (5.29) in Chap. 5, we obtain the effective Hamiltonian for the Lieb lattice in circularly polarized field. Using the Fourier component of the Hamiltonian $H_{0\boldsymbol{k},n}$ in Eq.(G.4), we have

$$\begin{aligned} H_{\mathrm{eff}\boldsymbol{k}} &= H_{0\boldsymbol{k},0}+\sum_{n>0}\frac{[H_{0\boldsymbol{k},-n},H_{0\boldsymbol{k},n}]}{n\Omega} \\ &= \begin{pmatrix} \epsilon_d & 2J_{\mathrm{eff}}\cos\frac{k_x}{2} & 2J_{\mathrm{eff}}\cos\frac{k_y}{2} \\ 2J_{\mathrm{eff}}\cos\frac{k_x}{2} & \epsilon_p & 2K_{\mathrm{eff}}\left[\cos\left(\frac{k_x+k_y}{2}\right)e^{-i\phi}+\cos\left(\frac{k_x-k_y}{2}\right)e^{i\phi}\right] \\ 2J_{\mathrm{eff}}\cos\frac{k_y}{2} & 2K_{\mathrm{eff}}\left[\cos\left(\frac{k_x+k_y}{2}\right)e^{i\phi}+\cos\left(\frac{k_x-k_y}{2}\right)e^{-i\phi}\right] & \epsilon_p \end{pmatrix}, \end{aligned} \tag{G.7}$$

with a phase $\phi = -\pi/2$ and effective hopping parameters,

$$J_{\mathrm{eff}} = JJ_0\left(\frac{A}{2}\right), \tag{G.8a}$$

$$K_{\mathrm{eff}} = \frac{2J^2}{\Omega}\sum_{n=1}^{\infty}\frac{1}{n}J_n^2\left(\frac{A}{2}\right)\sin\left(\frac{n\pi}{2}\right). \tag{G.8b}$$

The band structure of the effective Lieb model Eq. (G.7) is plotted in Fig. G-2(b). Due to the photo-assisted NNN hopping amplitude iK_{eff}, a photo-induced gap opens at the Dirac point M(π,π). The size of the gap is proportional to K_{eff}, whose A-dependence is plotted in Fig.G-3.

The Hall conductivity σ_{xy} is calculated from the nonequilibrium Kubo formula. In Fig. G-4(a) we show σ_{xy} as a function of A at half-filling. The Fermi level is set to the energy of the flat band. The values of intensity A at which the sign of σ_{xy} inverts correspond to the zeros of K_{eff} in Fig. G-3.

In Fig. G-4(b) we fix A and vary the Fermi level near the energy of the flat band. σ_{xy} does not change drastically in the vicinity of the flat band. Thus we conclude that the flat band has trivial Chern number $\nu = 0$, and the lower and the upper bands carries nontrivial Chern number: $\nu = \pm 1$, respectively.

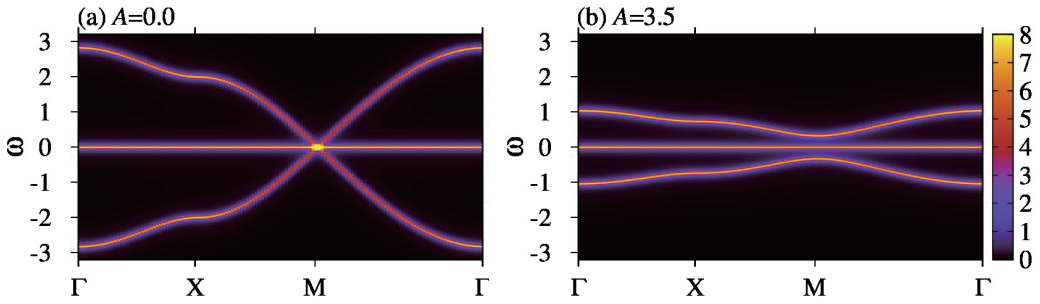

Figure G-2: The band structure of the Lieb lattice (a) in equilibrium, and (b) in a circularly polarized light with the intensity $A = 3.5$ and the photon energy $\Omega = 10$.

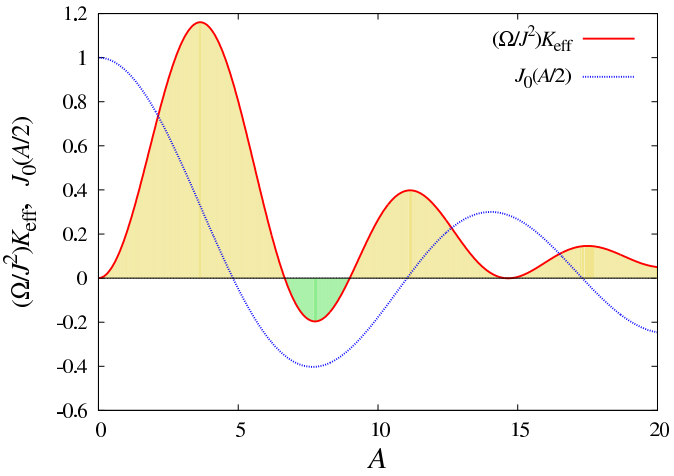

Figure G-3: Effective NNN hopping amplitude K_{eff} as a function of the intensity A.

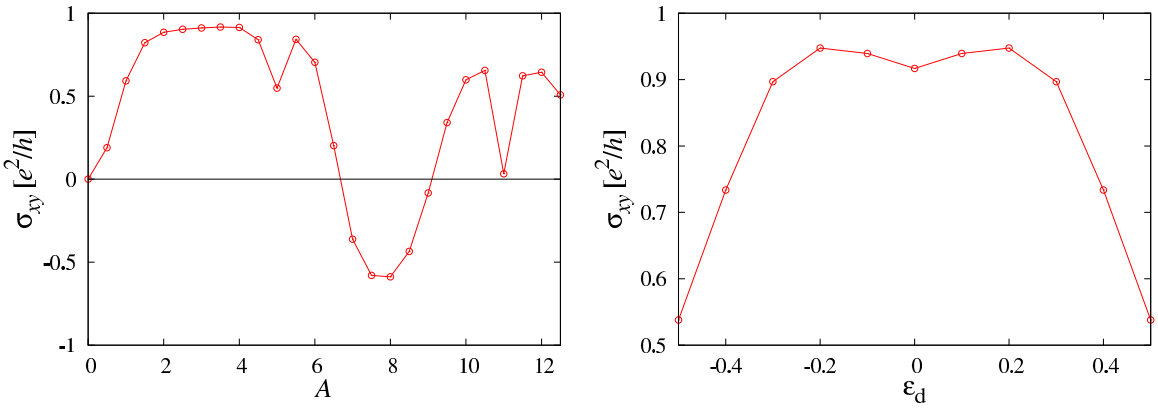

Figure G-4: dc-Hall conductivity in the Lieb lattice in a circularly polarized light with $\Omega = 10$. (a) The intensity A is varied from 0 to 12.5 with level offsets fixed as $\epsilon_d = \epsilon_p = 0$. (b) The level offset $\epsilon_d (= \epsilon_p)$ is varied from -0.5 to 0.5 with the intensity $A = 3.5$ is fixed.

Bibliography

[1] J. C. Slater, Phys. Rev. **49**, 537 (1936).

[2] J. C. Slater, Phys. Rev. **49**, 931 (1936).

[3] J. C. Slater, Phys. Rev. **52**, 198 (1937).

[4] S. Sakai, R. Arita, and H. Aoki, Phys. Rev. Lett. **99**, 216402 (2007).

[5] M. Imada, A. Fujimori, and Y. Tokura, Rev. Mod. Phys. **70**, 1039 (1998).

[6] N. F. Mott, Proc. Phys. Soc. London, Ser. A **62**, 416 (1949).

[7] P. W. Anderson, Science (80-.). **235**, 1196 (1987).

[8] V. J. Emery, Phys. Rev. Lett. **58**, 2794 (1987).

[9] F. C. Zhang and T. M. Rice, Phys. Rev. B **37**, 3759 (1988).

[10] M. Ogata and H. Fukuyama, Rep. Prog. Phys. **71**, 036501 (2008).

[11] V. J. Emery and G. Reiter, Phys. Rev. B **38**, 11938 (1988).

[12] K. Segawa, M. Kofu, S.-H. Lee, I. Tsukada, H. Hiraka, M. Fujita, S. Chang, K. Yamada, and Y. Ando, Nat. Phys. **6**, 579 (2010).

[13] P. Kuiper, G. Kruizinga, J. Ghijsen, M. Grinori, P. J. W. Weijis, F. M. F. de Groot, G. A. Sawatzky, H. Werveij, L. F. Feiner, and H. Petersen, Phys. Rev. B **38**, 6483 (1988).

[14] C. T. Chen, Phys. Rev. Lett. **66**, 104 (1991).

[15] T. Takahashi, H. Matsuyama, H. Katayama-Yoshida, Y. Okabe, S. Hosoya, K. Seki, H. Fujimoto, M. Sato, and H. Inokuchi, Nature **334**, 698 (1988).

[16] J. Zaanen, G. Sawatzky, and J. Allen, Phys. Rev. Lett. **55**, 418 (1985).

[17] K. Kuroki and H. Aoki, Phys. Rev. Lett. **76**, 4400 (1996).

[18] D. J. Thouless, M. Kohmoto, M. P. Nightingale, and M. den Nijs, Phys. Rev. Lett. **49**, 405 (1982).

[19] F. D. M. Haldane, Phys. Rev. Lett. **61**, 2015 (1988).

[20] C. L. Kane and E. J. Mele, Phys. Rev. Lett. **95**, 226801 (2005).

[21] C. L. Kane and E. J. Mele, Phys. Rev. Lett. **95**, 146802 (2005).

[22] L. Fu and C. L. Kane, Phys. Rev. B **74**, 195312 (2006).

[23] M. Z. Hasan and C. L. Kane, Rev. Mod. Phys. **82**, 3045 (2010).

[24] H. Okamoto, T. Miyagoe, K. Kobayashi, H. Uemura, H. Nishioka, H. Matsuzaki, A. Sawa, and Y. Tokura, Phys. Rev. B **83**, 125102 (2011).

[25] D. Fausti, R. I. Tobey, N. Dean, S. Kaiser, A. Dienst, M. C. Hoffmann, S. Pyon, T. Takayama, H. Takagi, and A. Cavalleri, Science **331**, 189 (2011).

[26] P. Kirchmann, L. Rettig, D. Nandi, U. Lipowski, M. Wolf, and U. Bovensiepen, Appl. Phys. A **91**, 211 (2008).

[27] Y. H. Wang, D. Hsieh, E. J. Sie, H. Steinberg, D. R. Gardner, Y. S. Lee, P. Jarillo-Herrero, and N. Gedik, Phys. Rev. Lett. **109**, 127401 (2012).

[28] Y. H. Wang, H. Steinberg, P. Jarillo-Herrero, and N. Gedik, Science (80-.). **342**, 453 (2013).

[29] T. Oka and H. Aoki, Phys. Rev. B **79**, 081406(R) (2009).

[30] Y. Zhou and M. W. Wu, Phys. Rev. B **83**, 245436 (2011).

[31] T. Oka and H. Aoki, *Quantum and Semi-classical Percolation and Breakdown in Disordered Solids (Lecture notes in Physics)*, vol. 762 of *Lecture Notes in Physics* (Springer Berlin Heidelberg, Berlin, Heidelberg, 2009).

[32] H. Aoki, N. Tsuji, M. Eckstein, M. Kollar, T. Oka, and P. Werner, arXiv p. 1310.5329 (2013).

[33] L. Perfetti, P. a. Loukakos, M. Lisowski, U. Bovensiepen, M. Wolf, H. Berger, S. Biermann, and A. Georges, New J. Phys. **10**, 053019 (2008).

[34] T. Kitagawa, E. Berg, M. Rudner, and E. Demler, Phys. Rev. B **82**, 235114 (2010).

[35] N. Tsuji, T. Oka, and H. Aoki, Phys. Rev. Lett. **103**, 047403 (2009).

[36] T. Oka and H. Aoki, J. Phys. Conf. Ser. **334**, 012060 (2011).

[37] G. C. Wick, Phys. Rev. **80**, 268 (1950).

[38] T. Matsubara, Prog. Theor. Phys. **14**, 351 (1955).

[39] A. Abrikosov, L. Gorkov, and I. Dzyaloshinski, *Methods of quantum field theory in statistical mechanics* (Dover, 1963).

[40] A. G. Hall, J. Phys. A Math. Gen. **8**, 214 (1975).

[41] P. Danielewicz, Ann. Phys. **152**, 239 (1984).

[42] R. P. Feynman, Phys. Rev. **76**, 749 (1949).

[43] L. V. Keldysh, Sov. Phys. JETP **47**, 1515 (1965).

[44] L. P. Kadanoff and G. Baym, *Quantum Statistical Mechanics* (W. A. Bejamin, New York, 1962).

[45] M. Gell-Mann and F. Low, Phys. Rev. **84**, 350 (1951).

[46] M. Wagner, Phys. Rev. B **44**, 6104 (1991).

[47] D. Semkat, D. Kremp, and M. Bonitz, Phys. Rev. E **59**, 1557 (1999).

[48] J. Rammer, *Quantum field theory of non-equilibrium states* (Cambridge University Press, 2007), 1st ed.

[49] A.-P. Jauho, N. S. Wingreen, and Y. Meir, Phys. Rev. B **50**, 5528 (1994).

[50] R. Kubo, J. Phys. Soc. Japan **12**, 570 (1957).

[51] P. C. Martin and J. Schwinger, Phys. Rev. **115**, 1342 (1959).

[52] A. O. Caldeira and A. J. Leggett, Phys. Rev. Lett. **46**, 211 (1981).

[53] A. O. Caldeira and A. J. Leggett, Phys. Rev. A **31**, 1059 (1985).

[54] M. Buettiker, Phys. Rev. B **32**, 1846 (1985).

[55] W. Metzner and D. Vollhardt, Phys. Rev. Lett. **62**, 324 (1989).

[56] A. Georges, P. Cedex, W. Krauth, and M. J. Rozenberg, Rev. Mod. Phys. **68**, 13 (1996).

[57] G. Kotliar, S. Savrasov, K. Haule, V. Oudovenko, O. Parcollet, and C. Marianetti, Rev. Mod. Phys. **78**, 865 (2006).

[58] J. K. Freericks, Phys. Rev. B **97**, 266408 (2006).

[59] N. Tsuji and P. Werner, Phys. Rev. B **88**, 165115 (2013).

[60] H. Kajueter and G. Kotliar, Phys. Rev. Lett. **77**, 131 (1996).

[61] M. J. Rozenberg, G. Kotliar, and X. Y. Zhang, Phys. Rev. B **49**, 10181 (1994).

[62] G. Kotliar and H. Kajueter, Phys. Rev. B **54**, 14221 (1996).

[63] M. Potthoff, T. Wegner, and W. Nolting, Phys. Rev. B **55**, 16132 (1997).

[64] R. E. Peierls, Z. Phys. **80**, 763 (1933).

[65] M. Rozenberg, G. Kotliar, and H. Kajueter, Phys. Rev. Lett. **75**, 105 (1995).

[66] A. Khurana, Phys. Rev. Lett. **64**, 1990 (1990).

[67] M. Eckstein and M. Kollar, Phys. Rev. B **78**, 205119 (2008).

[68] N. Tsuji, T. Oka, and H. Aoki, Phys. Rev. B **78**, 235124 (2008).

[69] G. H. Wannier, Rev. Mod. Phys. **34**, 645 (1962).

[70] X. G. Zhao, R. Jahnke, and Q. Niu, Phys. Lett. A **202**, 297 (1995).

[71] J. G. Bednorz and K. A. Müller, Z. Phys. B **60**, 189 (1986).

[72] A. Schilling, M. Cantoni, J. D. Guo, and H. R. Ott, Nature **363**, 56 (1993).

[73] E. Dagotto, Rev. Mod. Phys. **66**, 763 (1994).

[74] A. Macridin, M. Jarrell, T. Maier, and G. Sawatzky, Phys. Rev. B **71**, 134527 (2005).

[75] T. Timusk and B. Statt, Rep. Prog. Phys. **62**, 61 (1998).

[76] W. W. Warren, Phys. Rev. Lett. **62**, 1193 (1989).

[77] X. Wang, L. De'Medici, and A. Millis, Phys. Rev. B **83**, 094501 (2011).

[78] D. H. Dunlap and V. M. Kenkre, Phys. Rev. Lett. **34**, 3625 (1986).

[79] R. Shimano, G. Yumoto, J. Y. Yoo, R. Matsunaga, S. Tanabe, H. Hibino, T. Morimoto, and H. Aoki, Nat. Commun. **4**, 1841 (2013).

[80] C. Giannetti, G. Zgrablic, C. Consani, A. Crepaldi, D. Nardi, G. Ferrini, G. Dhalenne, A. Revcolevschi, and F. Parmigiani, Phys. Rev. B **80**, 235129 (2009).

[81] S. Iwai, M. Ono, A. Maeda, H. Matsuzaki, H. Kishida, H. Okamoto, and Y. Tokura, Phys. Rev. Lett. **91**, 057401 (2003).

[82] N. Grewe and H. Keiter, Phys. Rev. B **24**, 4420 (1981).

[83] Y. Kuramoto, Z. Phys. B **53**, 37 (1983).

[84] M. Eckstein and P. Werner, Phys. Rev. Lett. **110**, 126401 (2013).

[85] T. Oka and H. Aoki, Phys. Rev. B **82**, 064516 (2010).

[86] K. v. Klitzing, G. Dorda, and M. Pepper, Phys. Rev. Lett. **45**, 494 (1980).

[87] M. V. Berry, Proc. Roy. Soc. A **392**, 45 (1802).

[88] S. S. Chern, Ann. Math. **47**, 85 (1946).

[89] H. Aoki and M. S. Dresselhaus (ed.), *Physics of Graphene* (Springer-Verlag, 2013).

[90] A. K. Geim and K. S. Novoselov, Nat. Mater. **6**, 183 (2007).

[91] M. König, S. Wiedmann, C. Brüne, A. Roth, H. Buhmann, L. W. Molenkamp, X.-L. Qi, and S.-C. Zhang, Science **318**, 766 (2007).

[92] Y. Hor, A. Richardella, P. Roushan, Y. Xia, J. Checkelsky, A. Yazdani, M. Hasan, N. Ong, and R. Cava, Phys. Rev. B **79**, 195208 (2009).

[93] Y. L. Chen, J. G. Analytis, J.-H. Chu, Z. K. Liu, S.-K. Mo, X. L. Qi, H. J. Zhang, D. H. Lu, X. Dai, Z. Fang, *et al.*, Science **325**, 178 (2009).

[94] Z. Gu, H. a. Fertig, D. P. Arovas, and A. Auerbach, Phys. Rev. Lett. **107**, 216601 (2011).

[95] G. Santoro, M. Airoldi, S. Sorella, and E. Tosatti, Phys. Rev. B **47**, 16216 (1993).

[96] M. Ebrahimkhas and S. A. Jafari, Eur. Phys. Lett. **98**, 27009 (2012).

[97] S. A. Jafari, Eur. Phys. J. B **68**, 537 (2009).

[98] T. O. Wehling, E. Sasioglu, C. Friedrich, a. I. Lichtenstein, M. I. Katsnelson, and S. Blügel, Phys. Rev. Lett. **106**, 236805 (2011).

[99] F. Aryasetiawan, M. Imada, A. Georges, G. Kotliar, S. Biermann, and A. Lichtenstein, Phys. Rev. B **70**, 195104 (2004).

[100] M. Schüler, M. Rösner, T. O. Wehling, a. I. Lichtenstein, and M. I. Katsnelson, Phys. Rev. Lett. **111**, 036601 (2013).

[101] P. Soltan-Panahi, J. Struck, P. Hauke, A. Bick, W. Plenkers, G. Meineke, C. Becker, P. Windpassinger, M. Lewenstein, and K. Sengstock, Nat. Phys. **7**, 434 (2011).

[102] P. Soltan-Panahi, D.-S. Lühmann, J. Struck, P. Windpassinger, and K. Sengstock, Nat. Phys. **8**, 71 (2011).

[103] L. Tarruell, D. Greif, T. Uehlinger, G. Jotzu, and T. Esslinger, Nature **483**, 302 (2012).

[104] X. Chen, Z.-C. Gu, Z.-X. Liu, and X.-G. Wen, Science **338**, 1604 (2012).

[105] H. Yao and S. Ryu, Phys. Rev. B **88**, 064507 (2013).

[106] T. Kitagawa, T. Oka, A. Brataas, L. Fu, and E. Demler, Phys. Rev. B **84**, 235108 (2011).

[107] M.-T. Tran and K. Kuroki, Phys. Rev. B **79**, 125125 (2009).

[108] Z. Y. Meng, T. C. Lang, S. Wessel, F. F. Assaad, and A. Muramatsu, Nature **464**, 847 (2010).

[109] S. Sorella, Y. Otsuka, and S. Yunoki, Sci. Rep. **2**, 992 (2012).

[110] C. Honerkamp, Phys. Rev. Lett. **100**, 146404 (2008).

[111] V. N. Kotov, B. Uchoa, V. M. Pereira, F. Guinea, and a. H. Castro Neto, Rev. Mod. Phys. **84**, 1067 (2012).

[112] J. Kroha and P. Woelfle, arXiv pp. 1–21 (1998).

[113] K. Haule, S. Kirchner, J. Kroha, and P. Wölfle, Phys. Rev. B **64**, 155111 (2001).

[114] P. Werner, A. Comanac, L. de ' Medici, M. Troyer, and A. Millis, Phys. Rev. Lett. **97**, 076405 (2006).

[115] F. Marsiglio, Phys. Rev. B **42**, 2416 (1990).

[116] N. Goldman, D. F. Urban, and D. Bercioux, Phys. Rev. A **83**, 063601 (2011).

[117] C. Weeks and M. Franz, Phys. Rev. B **85**, 041104 (2012).

[118] V. Apaja, M. Hyrkas, and M. Manninen, Phys. Rev. A **82**, 041402(R) (2010).